



AFRL-AFOSR-VA-TR-2016-0301

**Nonequilibrium Molecular Energy Coupling and Conversion
Mechanisms**

**Igor Adamovich
OHIO STATE UNIVERSITY RESEARCH FOUNDATION
1960 KENNEY ROAD
COLUMBUS, OH 43210-1016**

**08/28/2016
Final Report**

DISTRIBUTION A: Distribution approved for public release.

Air Force Research Laboratory
AF Office Of Scientific Research (AFOSR)/RTB2

REPORT DOCUMENTATION PAGEForm Approved
OMB No. 0704-0188

The public reporting burden for this collection of information is estimated to average 1 hour per response, including the time for reviewing instructions, searching existing data sources, gathering and maintaining the data needed, and completing and reviewing the collection of information. Send comments regarding this burden estimate or any other aspect of this collection of information, including suggestions for reducing the burden, to Department of Defense, Washington Headquarters Services, Directorate for Information Operations and Reports (0704-0188), 1215 Jefferson Davis Highway, Suite 1204, Arlington, VA 22202-4302. Respondents should be aware that notwithstanding any other provision of law, no person shall be subject to any penalty for failing to comply with a collection of information if it does not display a currently valid OMB control number.
PLEASE DO NOT RETURN YOUR FORM TO THE ABOVE ADDRESS.

1. REPORT DATE (DD-MM-YYYY) 01/08/2016	2. REPORT TYPE Final report	3. DATES COVERED (From - To) 01/09/2012 - 14/05/2016		
4. TITLE AND SUBTITLE Nonequilibrium Molecular Energy Coupling and Conversion Mechanisms		5a. CONTRACT NUMBER FA9550-12-1-0439		
		5b. GRANT NUMBER		
		5c. PROGRAM ELEMENT NUMBER		
6. AUTHOR(S) Igor V. Adamovich and Anne B. McCoy		5d. PROJECT NUMBER		
		5e. TASK NUMBER		
		5f. WORK UNIT NUMBER		
7. PERFORMING ORGANIZATION NAME(S) AND ADDRESS(ES) Ohio State University, Department of Mechanical and Aerospace Engineering 201 W. 19th Ave., Columbus, OH 43210				
8. PERFORMING ORGANIZATION REPORT NUMBER				
9. SPONSORING/MONITORING AGENCY NAME(S) AND ADDRESS(ES) Air Force Office of Scientific Research, 875 N. Randolph, Ste. 325, Arlington, VA 22203				
10. SPONSOR/MONITOR'S ACRONYM(S)				
11. SPONSOR/MONITOR'S REPORT NUMBER(S)				
12. DISTRIBUTION/AVAILABILITY STATEMENT DISTRIBUTION A: Distribution approved for public release.				
13. SUPPLEMENTARY NOTES				
14. ABSTRACT The report presents results of development of an accurate, physics-based model of vibrational and rotational energy transfer in three-dimensional collisions of rotating diatomic molecules, applicable over a wide range of collision energies and vibrational / rotational quantum numbers, and results of detailed kinetic modeling studies of state-to-state molecular energy transfer processes, including excitation of vibrational and electronic states by electron impact, collisional quenching of excited electronic states, vibration-vibration (V-V) energy transfer, vibration-rotation-translation (V-R-T) relaxation, internal mode energy thermalization, molecular dissociation, and plasma chemical reactions.				
15. SUBJECT TERMS molecular energy transfer, reaction cross sections, plasma chemical reactions, vibrational relaxation, energy thermalization, flow perturbations				
16. SECURITY CLASSIFICATION OF: a. REPORT U		17. LIMITATION OF ABSTRACT b. ABSTRACT U c. THIS PAGE U	18. NUMBER OF PAGES UU 93	19a. NAME OF RESPONSIBLE PERSON Igor V. Adamovich 19b. TELEPHONE NUMBER (Include area code) 614-292-8453

INSTRUCTIONS FOR COMPLETING SF 298

1. REPORT DATE. Full publication date, including day, month, if available. Must cite at least the year and be Year 2000 compliant, e.g. 30-06-1998; xx-06-1998; xx-xx-1998.

2. REPORT TYPE. State the type of report, such as final, technical, interim, memorandum, master's thesis, progress, quarterly, research, special, group study, etc.

3. DATE COVERED. Indicate the time during which the work was performed and the report was written, e.g., Jun 1997 - Jun 1998; 1-10 Jun 1996; May - Nov 1998; Nov 1998.

4. TITLE. Enter title and subtitle with volume number and part number, if applicable. On classified documents, enter the title classification in parentheses.

5a. CONTRACT NUMBER. Enter all contract numbers as they appear in the report, e.g. F33315-86-C-5169.

5b. GRANT NUMBER. Enter all grant numbers as they appear in the report. e.g. AFOSR-82-1234.

5c. PROGRAM ELEMENT NUMBER. Enter all program element numbers as they appear in the report, e.g. 61101A.

5e. TASK NUMBER. Enter all task numbers as they appear in the report, e.g. 05; RF0330201; T4112.

5f. WORK UNIT NUMBER. Enter all work unit numbers as they appear in the report, e.g. 001; AFAPL30480105.

6. AUTHOR(S). Enter name(s) of person(s) responsible for writing the report, performing the research, or credited with the content of the report. The form of entry is the last name, first name, middle initial, and additional qualifiers separated by commas, e.g. Smith, Richard, J, Jr.

7. PERFORMING ORGANIZATION NAME(S) AND ADDRESS(ES). Self-explanatory.

8. PERFORMING ORGANIZATION REPORT NUMBER. Enter all unique alphanumeric report numbers assigned by the performing organization, e.g. BRL-1234; AFWL-TR-85-4017-Vol-21-PT-2.

9. SPONSORING/MONITORING AGENCY NAME(S) AND ADDRESS(ES). Enter the name and address of the organization(s) financially responsible for and monitoring the work.

10. SPONSOR/MONITOR'S ACRONYM(S). Enter, if available, e.g. BRL, ARDEC, NADC.

11. SPONSOR/MONITOR'S REPORT NUMBER(S). Enter report number as assigned by the sponsoring/monitoring agency, if available, e.g. BRL-TR-829; -215.

12. DISTRIBUTION/AVAILABILITY STATEMENT. Use agency-mandated availability statements to indicate the public availability or distribution limitations of the report. If additional limitations/ restrictions or special markings are indicated, follow agency authorization procedures, e.g. RD/FRD, PROPIN, ITAR, etc. Include copyright information.

13. SUPPLEMENTARY NOTES. Enter information not included elsewhere such as: prepared in cooperation with; translation of; report supersedes; old edition number, etc.

14. ABSTRACT. A brief (approximately 200 words) factual summary of the most significant information.

15. SUBJECT TERMS. Key words or phrases identifying major concepts in the report.

16. SECURITY CLASSIFICATION. Enter security classification in accordance with security classification regulations, e.g. U, C, S, etc. If this form contains classified information, stamp classification level on the top and bottom of this page.

17. LIMITATION OF ABSTRACT. This block must be completed to assign a distribution limitation to the abstract. Enter UU (Unclassified Unlimited) or SAR (Same as Report). An entry in this block is necessary if the abstract is to be limited.

Nonequilibrium Molecular Energy Coupling and Conversion Mechanisms

FA9550-12-1-0439

Final report

by

Igor V. Adamovich

*Department of Mechanical and Aerospace Engineering
The Ohio State University, Columbus, OH 43210*

and

Anne B. McCoy

*Department of Chemistry and Biochemistry
The Ohio State University, Columbus, OH 43210*

Abstract

The report presents results of development of an accurate, physics-based model of vibrational and rotational energy transfer in three-dimensional collisions of rotating diatomic molecules, applicable over a wide range of collision energies and vibrational / rotational quantum numbers, and results of detailed kinetic modeling studies of state-to-state molecular energy transfer processes, including excitation of vibrational and electronic states by electron impact, collisional quenching of excited electronic states, vibration-vibration (V-V) energy transfer, vibration-rotation-translation (V-R-T) relaxation, internal mode energy thermalization, molecular dissociation (both by electron impact and during quenching of excited electronic state), and plasma chemical reactions. The kinetic modeling prediction are compared with recent time-resolved, spatially resolved measurements of vibrational level populations, gas temperature, and atomic species and radical number densities in the afterglow of a ns pulse discharge generating strong internal energy mode disequilibrium in air and fuel-air mixtures. The present results provide new quantitative insight into kinetics of molecular energy transfer and plasma chemical reactions in air and fuel-air mixtures, at the conditions of strong internal energy mode disequilibrium. Closed-form, physics-based, analytic expressions for state-to-state rotational and vibrational energy transfer transition probabilities lend themselves to straightforward incorporation into state-of-the-art DSMC nonequilibrium flow codes. Understanding kinetics of energy thermalization and chemical reactions in ns pulse discharges considerably improves predictive capability of kinetic models, which has major implications for plasma assisted combustion and high-speed plasma flow control, where these discharges are used increasingly widely.

Final Report Overview

The main focus of this report is on (i) development of an accurate, physics-based model of vibrational and rotational energy transfer in three-dimensional collisions of rotating diatomic molecules, applicable over a wide range of collision energies and vibrational / rotational quantum numbers, and (ii) detailed kinetic modeling studies of state-to-state molecular energy transfer processes, including excitation of vibrational and electronic states by electron impact, collisional quenching of excited electronic states, vibration-vibration (V-V) energy transfer, vibration-rotation-translation (V-R-T) relaxation, internal mode energy thermalization, molecular dissociation (both by electron impact and during quenching of excited electronic state), and plasma chemical reactions. The kinetic modeling prediction are compared with recent time-resolved, spatially resolved measurements of vibrational level populations, gas temperature, and atomic species and radical number densities in the afterglow of a ns pulse discharge generating strong internal energy mode disequilibrium in air and fuel-air mixtures. The report is organized as follows:

In Section I, a three-dimensional, nonperturbative, semiclassical analytic model of vibrational energy transfer in collisions between a rotating diatomic molecule and an atom, and between two rotating diatomic molecules (Forced Harmonic Oscillator – Free Rotation model) developed in our previous work has been extended to incorporate rotational relaxation and coupling between vibrational, translational and rotational energy transfer. The model is based on analysis of semiclassical trajectories of rotating molecules interacting by a repulsive exponential atom-to-atom potential. The model predictions are compared with the results of three-dimensional close-coupled semiclassical trajectory calculations using the same potential energy surface. The comparison demonstrates good agreement between analytic and numerical probabilities of rotational and vibrational energy transfer processes, over a wide range of total collision energies, rotational energies, and impact parameter. The model predicts probabilities of single-quantum and multi-quantum vibrational-rotational transitions and is applicable up to very high collision energies and quantum numbers.

In Section II, kinetic modeling calculations provide key new insight into the kinetics of vibrational excitation of nitrogen and plasma chemical reactions in a nanosecond pulse, “diffuse filament” discharges in nitrogen and dry air at a moderate energy loading per molecule, ~0.1 eV/molecule. It is shown that taking into account Coulomb collisions between electrons is critical since they change the electron energy distribution function and, as a result, strongly affect populations of excited states and radical concentrations in the discharge. The results demonstrate that the apparent transient rise of N₂ “first level” vibrational temperature after the discharge pulse, detected in the experiments, is due to net downward V-V energy transfer in N₂-N₂ collisions, which increases N₂(X¹Σ,v=1) population. Most importantly, comparison of the model predictions with the experimental data shows that NO formation in the afterglow of a ns pulse discharge occurs via reactive quenching of multiple excited electronic levels of nitrogen molecule, N₂^{*}, by O atoms. This result is critical for accurate prediction of NO formation in low-temperature pulsed air plasmas, used for plasma-assisted ignition and plasma flow control.

In Section III, time-resolved and spatially resolved temperature measurements, by pure rotational picosecond broadband Coherent Anti-Stokes Raman Spectroscopy (CARS), and kinetic modeling calculations are used to study kinetics of energy thermalization in nanosecond pulse discharges in air and hydrogen-air mixtures. The diffuse filament, nanosecond pulse discharge (pulse duration ~100 ns) is sustained between two spherical electrodes and is operated at a low pulse repetition rate to enable temperature measurements over a wide range of time scales after the discharge pulse. The experimental results demonstrate high accuracy of pure rotational ps CARS for thermometry measurements in highly transient nonequilibrium plasmas. Rotational-translational temperatures are measured for time delays after the pulse ranging from tens of ns to tens of ms, spanning several orders of magnitude of time scales for energy thermalization in nonequilibrium plasmas. In addition, radial temperature distributions across the plasma filament are measured for several time delays after the discharge pulse. Kinetic modeling calculations using a state-specific master equation kinetic model of reacting hydrogen-air plasmas show

good agreement with experimental data. The results demonstrate that energy thermalization and temperature rise in these plasmas occur in two clearly defined stages, (i) “rapid” heating, caused by collisional quenching of excited electronic states of N₂ molecules by O₂, and (ii) “slow” heating, caused primarily by N₂ vibrational relaxation by O atoms (in air) and by chemical energy release during partial oxidation of hydrogen (in H₂-air). This result is critical for predicting performance of ns pulse surface plasma flow actuators, which rely primarily on localized flow heating on sub-acoustic time scale, and for assessing feasibility of high-speed aerodynamic flow control by vibrational relaxation accelerated using injection of rapid relaxer species.

Finally, in Section IV, kinetic modeling is used to analyze energy partition and energy transfer in nanosecond pulse discharges sustained between two spherical electrodes in nitrogen and air. The modeling predictions are compared with previous time-resolved temperature and N₂(X¹Σ_g⁺,v=0-9) vibrational population measurements by picosecond broadband Coherent Anti-Stokes Raman Spectroscopy (CARS) and phase-locked schlieren imaging. The model shows good agreement with experimental data, reproducing experimental discharge current pulse waveforms, as well as dominant processes of energy transfer in the discharge and the afterglow. Specifically, the results demonstrate that temperature rise in the plasma occurs in two stages, (i) “rapid” heating on sub-acoustic time scale, dominated by N₂(A³Σ_u⁺) energy pooling processes, N₂(B³Π_g) and N²P,²D quenching (in nitrogen), and by quenching of excited electronic states of N₂ molecules by O₂ (in air), and (ii) “slow” heating due to N₂ vibrational relaxation by O atoms (in air), nearly completely missing in nitrogen. Comparison of the model predictions with N₂ vibrational level populations confirms that N₂ vibrational temperature rise after the discharge pulse is caused by the “downward” vibrational-vibrational exchange depopulating higher vibrational levels and populating vibrational level v=1. The model reproduces temporal dynamics of vibrational level populations and temperature in the discharge and the afterglow, indicating that energy partition among different modes (vibrational, electronic, dissociation, and ionization) is predicted accurately. At the present conditions, energy fraction coupled to the positive column of the discharge filament in air is approximately 50%, with the rest coupled to the cathode layer. Nearly 10% of the total pulse energy is spent on O atom generation, and about 10% is thermalized on sub-acoustic time scale, producing a strong compression wave in the radial direction.

The present results provide new quantitative insight into kinetics of molecular energy transfer and plasma chemical reactions in air and fuel-air mixtures, at the conditions of strong internal energy mode disequilibrium. Closed-form, physics-based, analytic expressions for state-to-state rotational and vibrational energy transfer transition probabilities lend themselves to straightforward incorporation into state-of-the-art DSMC nonequilibrium flow codes. Also, understanding kinetics of energy thermalization and chemical reactions in ns pulse discharges considerably improves predictive capability of kinetic models, which has major implications for plasma assisted combustion and high-speed plasma flow control, where these discharges are used increasingly widely.

I. Three-Dimensional Analytic Probabilities of Coupled Vibrational-Rotational-Translational Energy Transfer for DSMC Modeling of Nonequilibrium Flows

I.1. Introduction

Vibrational energy transfer processes in collisions of diatomic molecules play an important role in gas discharges, molecular lasers, plasma chemical reactors, and high enthalpy gas dynamic flows. In these nonequilibrium environments, energy loading per molecule may be up to several eV, while disequilibrium among translational, rotational, vibrational, and electronic energy modes of heavy species, and with the free electron energy, may be very strong. This results in development and maintaining of strongly nonequilibrium molecular vibrational energy distributions, which induce a wide range of energy transfer processes among different energy modes and species, chemical reactions, and ionization [1-4]. The rates of these processes are strongly dependent on populations of high vibrational levels of molecules, which at high temperatures are controlled primarily by vibration-rotation-translation (V-R-T) energy transfer,



where AB and M represent a diatomic molecule and a collision partner (another molecule or an atom), respectively, v and w are vibrational quantum numbers, and j_1 and j_2 are rotational quantum numbers.

State-specific rates of vibrational relaxation processes, over a wide range of temperatures and vibrational quantum numbers, are needed for numerous nonequilibrium flow applications, such as radiation prediction in aerospace propulsion flows, in high altitude rocket plumes, and behind strong shock waves. For a number of diatomic species, such as H_2 , N_2 , and O_2 , vibrational relaxation rates have been predicted by semiclassical and quasiclassical trajectory calculations, using analytic atom-to-atom and *ab initio* potential energy surfaces [5-17]. Recently, extensive databases incorporating state-specific vibrational-rotational-translational (V-R-T) energy transfer and dissociation rate coefficients for $\text{N}_2\text{-N}$ have also been developed using quasiclassical trajectory calculations for *ab initio* potential energy surfaces [18-24]. These databases have been used for modeling of nitrogen excitation and dissociation behind strong normal shocks, in nonequilibrium nozzle flows, and in hypersonic flows over a cylinder [25-28]. Development of a comprehensive, complementary *ab initio* database for $\text{N}_2\text{-N}_2$ collisions remains an open challenge. These databases also make possible thorough validation of analytic, physics-based, models of vibrational and rotational energy transfer, which provide insight into the energy transfer mechanism and lend themselves to being incorporated into existing nonequilibrium flow codes.

State-specific V-T, V-V, and molecular dissociation rates in three-dimensional atom-molecule and molecule-molecule collisions have been predicted analytically, using a nonperturbative Forced Harmonic Oscillator – Free Rotation (FHO-FR) energy transfer model [29-31]. V-T and V-V transition probabilities predicted by the analytic FHO-FR model are in very good agreement with numerical trajectory calculations over a wide range of collision energies, for the same intermolecular interaction potential. The FHO-FR model also reproduces the dependence of transition probabilities on individual collision parameters such as rotational energy, impact parameter, and collision reduced mass. Finally, the model equally well predicts probabilities of single-quantum and multi-quantum transitions, up to very high collision energies and quantum numbers. Although the FHO-FR model does include the effect of rotational motion of molecules during the collision on vibrational energy probabilities, the assumption of free rotation does not allow predicting rotational energy transfer. This limitation is critical for modeling of molecular dissociation from high vibrational levels, since rotational energy may well have a significant effect on overcoming the dissociation energy threshold.

The main objective of the present work is expanding the FHO-FR model to include rotational relaxation and coupling between vibrational, translational and rotational energy transfer. The resultant set of closed-form, analytic V-R-T transition probabilities in atom-atom and molecule-atom collisions can be readily incorporated into state-specific DSMC flow codes, such as have been developed recently

[28,32,33].

I.2. R-T and V-R-T energy transfer models

In the FHO-FR model, dynamics of collisions between a rotating symmetric diatomic molecule and an atom, or collisions between two rotating diatomic molecules, was analyzed assuming that the rotational motion was not affected by the collision. Thus, the only effect of rotation on the collision trajectory in the FHO-FR model is the periodic modulation of the repulsive, exponential, atom-to-atom interaction potential. As demonstrated in Ref. [29], this modulation makes the time-dependent interaction more sudden, thus considerably increasing vibrational energy transfer probabilities. The assumption of free rotation is similar to the basic premise of the semiclassical approach, which decouples the classical translational-rotational trajectory during a collision from the vibrational motion of the oscillator, which is treated quantum mechanically. Combining this approach with the exact solution of the Schrodinger equation predicting probabilities of vibration-translation (V-T) and vibration-vibration (V-V) energy transfer in a forced harmonic oscillator, valid for arbitrary values of initial and final vibrational quantum numbers [29,30], and using frequency correction to account for anharmonicity, yields closed-form analytic expressions for V-T and V-V probabilities in three-dimensional atom-molecule and molecule-molecules collisions. These probabilities are in very good agreement with “exact” close-coupled semiclassical trajectory calculations for N₂-N₂, for the same intermolecular potential, over a wide range of collision energies (temperatures) and vibrational quantum numbers [29,30]. Also, it has been shown that FHO-FR model accurately reproduces the dependence of the numerical V-T probabilities on the rotational energies of the molecules. This demonstrates that modulation of the interaction potential by rotation is indeed the dominant effect of rotational motion on vibrational energy transfer (producing strong “R→V-T” coupling).

The assumption of free rotation used by the FHO-FR model, which does not have a significant effect on the V-T and V-V rates, is no longer sufficient if rotational energy transfer during a collision also needs to be predicted. High-energy collisions of strongly vibrationally excited molecules, when a significant fraction of the total collision energy is transferred to the rotational energy mode (producing strong “V-T→R” coupling), are of particular interest since they may affect the rate of molecular dissociation. Basically, these collisions may result in strong contribution of centrifugal forces to dissociation.

Incorporating rotational energy transfer into the semiclassical FHO theory requires an analytic solution for the classical vibrational-rotational trajectory in three-dimensional collisions of an atom and a molecule, or in collisions of two diatomic molecules. A previous semiclassical trajectory calculation study of rotational relaxation of N₂ in collisions with Ar [34] pointed out the existence of an approximate “stochastic” analytic solution for the rotational transition probabilities,

$$P(j_0 \rightarrow j) = \frac{1}{\sqrt{4\pi S}} \exp\left[-\frac{(j_0 - j)^2}{4S}\right], \quad (\text{I.2})$$

where j_0 and j are the initial and the final rotational quantum numbers. In Eq. (I.2), S is an integral over the collision trajectory, which depends on the total collision energy, rotational energy of the molecule, impact parameter, and the direction of the angular momentum vector. In Ref. [34], S was evaluated numerically, based on an approximate analytic solution for the center-of-mass distance during the collision. The results suggested that the distribution of probabilities predicted by Eq. (I.2) may be fairly accurate in the limit of weak coupling, i.e. at large impact parameters. The possibility of evaluating the entire set of rotational transition probabilities in terms of a single integral parameter of the trajectory is very attractive, although obtaining a general analytic solution for the trajectory, for a realistic intermolecular potential, appears to be an intractable problem.

Further analysis done in the present work shows that for the intermolecular potential dominated by steep repulsion, such as $U(R) \sim A \exp(-\alpha R)$, where the spatial scale for the potential energy change, $1/\alpha$, is much less than the distance of closest approach, $1/\alpha \ll R_0$, the trajectory integral S in Eq. (I.2) scales proportionally to the “effective kinetic energy” of collision, i.e. the energy of relative translational motion in the radial direction near the “maximum interaction point”, where $U(R_0)$ reaches maximum [29,30], as follows:

$$S(j_0 \rightarrow j, E_t, b) = \frac{(\sqrt{\xi E_t / B} - j_0)^2}{8} \left[1 - \left(\frac{b}{R_0} \right)^2 \right]. \quad (\text{I.3})$$

In Eq. (I.3), E_t is the total collision energy, b is the impact parameter, $\xi=1$ and $\xi=5/6$ for atom-molecule and molecule-molecule, respectively. The lower value of ξ for molecule-molecule collisions is due to energy storage in the rotation of the “projectile” molecule, such that a smaller fraction of total collision energy is available for the translational motion. As will be shown below, this simple correction is sufficient to account for the rotational motion of the “projectile” molecule on rotational energy transfer in the “target” molecule, for a wide range of conditions. Energy and angular momentum conservation impose the following constraints on the final value of the rotational quantum number after collision,

$$\max \left(0, E_{r0} - \frac{\xi E_t}{2} \right) < Bj^2 < E_t - \frac{E_{k0}}{2} \quad , \quad (\text{I.4})$$

$$E_t = E_{k0} + E_{r0} = E_k + E_r, \quad E_{r0} = Bj_0^2, \quad E_r = Bj^2$$

where E_{k0} , E_k , E_{r0} , and E_r are the initial and the final values of the kinetic (translational) and the rotational energy of the “target” molecule.

After averaging the square of the rotational energy transferred, predicted by Eqs. (I.2 - I.4), over impact parameter and rotational quantum numbers,

$$P(j_0 \rightarrow j, E_t) = \int_0^1 P(j_0 \rightarrow j, E_t, b) d \left(\frac{b^2}{R_0^2} \right) \quad , \quad (\text{I.5})$$

$$\langle \Delta E_r^2(E_t) \rangle^{1/2} = \left(\frac{\int_0^{\sqrt{E_{total}/B}} \int_0^{\sqrt{E_{total}/B}} (2j_0+1)(E_r - E_{r0})^2 P(j_0 \rightarrow j, E_t) dj_0 dj}{\int_0^{\sqrt{E_{total}/B}} \int_0^{\sqrt{E_{total}/B}} (2j_0+1) P(j_0 \rightarrow j, E_t) dj_0 dj} \right)^{1/2} = \frac{\xi}{8} E_t$$

the maximum value of the trajectory integral in Eq. (I.3), S_{max} , can be related to the root-mean-square (RMS) average rotational energy transferred in a collision:

$$S_{max} = \frac{\xi}{8} \frac{E_t}{B} = \frac{\langle \Delta E_r^2(E_t) \rangle^{1/2}}{B} = \frac{\Delta E_r^{RMS}}{B}. \quad (\text{I.6})$$

Thus, the rotational energy transfer probability distribution over the final rotational quantum numbers is determined by a single parameter, RMS average rotational energy transfer, i.e. by the rotational relaxation time [35]. Note that the expressions for S and ΔE_r^{RMS} do not contain explicitly the repulsive exponential potential parameter, α . Basically, since $1/\alpha \ll R_0$, rotational energy transfer can be assumed to occur in

hard sphere collisions. Finally, to account for detailed balance between the forward and the reverse processes, $P(j_0 \rightarrow j, E_t, b)(2j_0+1) = P(j \rightarrow j_0, E_t, b)(2j+1)$, the expressions for S in the transition probabilities need to be “symmetrized” over the initial and the final rotational quantum states,

$$P(j_0 \rightarrow j, E_t, b) = \sqrt{\frac{1}{4\pi S}} \exp\left[-\frac{(j_0 - j)^2}{4S}\right] \sqrt{\frac{2j+1}{2j_0+1}}, \quad (\text{I.2a})$$

$$S(j_0 \rightarrow j, E_t, b) = \frac{(\sqrt{\xi E_t / B} - \sqrt{j_0 j})^2}{8} \left[1 - \left(\frac{b}{R_0} \right)^2 \right], \quad (\text{I.3a})$$

Note that symmetrization affects normalization of the rotational transition probabilities given by Eq. (I.2a), and they need to be renormalized to ensure that $\int_{j_{\min}}^{j_{\max}} P(j_0 \rightarrow j) dj = 1$, where j_{\min} and j_{\max} are determined by Eq. (I.4).

For the exponential repulsive part of the intermolecular potential used in semiclassical trajectory calculations to predict V-T and V-V energy transfer rates for N₂-N₂ [10] and rotational relaxation cross section for N₂-N₂ [35], $\alpha = 4.0 \text{ \AA}^{-1}$, the condition $I/\alpha \ll R_0$ is satisfied, $I/\alpha R_0 \sim 0.1$. The closest approach distance in Eq. (I.3a), evaluated for the potential used in Ref. [10] in previous work on FHO model [29,30], is

$$R_0(E_{total}) \approx 2.5 - \frac{1}{2\alpha} \ln\left(\frac{E_t(\text{cm}^{-1})}{10^4}\right) \text{ \AA}. \quad (\text{I.7})$$

In the first approximation, a semiclassical V-R-T transition probability in atom-molecule collisions can be expressed as a product of V-T and R-T probabilities, as follows,

$$P_{VRT}(v, j_1 \rightarrow w, j_2, E_t, b) = P_{RT}(j_1 \rightarrow j_2, E_t, b) \cdot P_{VT}(v \rightarrow w, \bar{E}_r, E_t, b), \quad (\text{I.8})$$

In Eq. (I.8), symmetrized R-T probabilities are given by Eq. (I.2a), and V-T transition probabilities between vibrational quantum numbers v and w are predicted by the Forced Harmonic Oscillator – Free Rotation (FHO-FR) model [29],

$$P_{VT}(v \rightarrow w) \approx \frac{(n_s)^s}{(s!)^2} Q^s \exp\left[-\frac{2n_s}{s+1} Q - \frac{n_s^2}{(s+1)^2(s+2)} Q^2\right], \quad (\text{I.9})$$

$$s = |v - w|, \quad n_s = \left[\frac{\max(v, w)!}{\min(v, w)!} \right]^{1/s}.$$

In Eq. (I.9), Q is the average number of vibrational quanta transferred per collision (a trajectory integral), calculated using an approximate analytic trajectory for collisions of freely rotating molecules [29],

$$Q(E_t, E_r, b) = \frac{\theta'}{4\theta} \frac{1}{\sinh^2\left[\frac{\pi\omega}{au\gamma(E_t, \bar{E}_r, b)}\right]} \quad (\text{I.10})$$

$$\gamma(E_t, E_r, b) = \max \left[0, \sqrt{\left(1 - \frac{\bar{E}_r}{E_t}\right) \left(1 - \frac{b^2}{R_0^2}\right)} - \frac{\sin(2\vartheta) \cos(\varphi)}{2} \sqrt{\frac{\bar{E}_r}{E_t}} \right] \quad (I.11)$$

In Eqs. (I.10, I.11), $\omega = \frac{|E_w - E_v|}{s\hbar}$ is the average vibrational quantum for the transition $v \rightarrow w$,

$$\theta' = \frac{4\pi^2 \omega^2 m}{\alpha^2 k}, \quad \theta = \frac{\hbar\omega}{k}, \quad m \text{ is the collision reduced mass, } \bar{E}_r = Bj_1 j_2 \text{ is the symmetrized rotational energy,}$$

$u = \sqrt{2E_t/m}$, and ϑ, φ are the rotation phase angles at the closest approach point [29]. Although it is desirable to average the trajectory integral, Q , in Eqs. (I.10, I.11) over the randomly distributed rotation phase angles, $0 \leq \vartheta \leq \pi$ and $0 \leq \varphi \leq \pi/2$, it is challenging to do this analytically with sufficient accuracy, e.g. by expanding it in series near its maximum value, achieved at $\bar{E}_r/E_t = 0.2$, $b/R_0 = 0$, $\vartheta = 3\pi/4$, and $\varphi = 0$ [29]. This difficulty occurs because V-T transition probabilities actually decrease at high values of Q , as can be seen from Eq. (I.9). Therefore at high total collision energies (i.e. high u values in Eq. (I.10)), collisions with low values of γ , which correspond to high rotational energies ($\bar{E}_r/E_t \sim 1$), large impact parameters ($b/R_0 \sim 1$), and rotation in a plane nearly perpendicular to the velocity vector ($\varphi \sim \pi/2$) provide the dominant contribution to V-T relaxation. As demonstrated in Ref. [29], this effect causes complete breakdown of the one-dimensional FHO V-T energy transfer model at high energies, compared to the three-dimensional collision FHO-FR model.

In molecule-molecule collisions, parameter γ in Eq. (I.11) is calculated taking into account the effect of rotation of both molecules on the collision trajectory, and thus on vibrational energy transfer probabilities [30],

$$\gamma(E_t, E_{r1}, E_{r2}, b) = \max \left[0, \sqrt{\left(1 - \frac{\bar{E}_{r1}}{E_t} - \frac{\bar{E}_{r2}}{E_t}\right) \left(1 - \frac{b^2}{R_0^2}\right)} - \frac{\sin(2\vartheta_1) \cos(\varphi_1)}{2} \sqrt{\frac{\bar{E}_{r1}}{E_t}} - \frac{\sin(2\vartheta_2) \cos(\varphi_2)}{2} \sqrt{\frac{\bar{E}_{r2}}{E_t}} \right] \quad (I.11a)$$

In the present work, the projectile molecule was assumed to remain in vibrational level $v'=w'=0$ [30], and vibrational-rotational transitions in the projectile molecule were not evaluated explicitly. However, the present approach can be easily extended to predict probabilities of simultaneous VRT transitions in both molecules, $P(v, j_1, v', j_1' \rightarrow w, j_2, w', j_2')$.

Thus, V-R-T transition probabilities are expressed in terms of two trajectory integrals, S and Q , given by Eq. (I.3a) and Eqs. (I.10, I.11, I.11a), respectively, each one of them being a function of total collision energy, rotational energy, and impact parameter. Note that V-T / R-T factorization used in Eq. (I.8) does not fully account for V-R-T coupling since V-T probabilities in it are still calculated for free-rotating molecules, and is therefore only a first-order approximation.

I.3. Comparison with Trajectory Calculations

To assess the accuracy of the simple analytic solution for the rotational transition probabilities given by Eqs. (I.2a, I.3a, I. IV.4), the model predictions have been compared with the results of semiclassical trajectory calculations (a) between a nitrogen molecule and an atom of the same mass (“spherical nitrogen”), and (b) between two nitrogen molecules, using trajectory calculation codes ADIAV and DIDIE developed by Billing [36,37]. In both cases, the exponential repulsive interaction potential used was the same as in previous work predicting FHO-FR vibrational energy transfer rates in atom-molecule and molecule-molecule collisions [29,30]. The maximum impact parameter used in the numerical calculations was $R=2.5$ Å. In the calculations, the total collision energy, E_t , was kept constant, while rotational and orbital angular momenta, as well as initial orientation of the collision partners, were

selected randomly, for 10^4 - 10^5 trajectories.

Figure I.1 compares transition probabilities in atom-molecule collisions for three different impact parameters, as well as averaged over the impact parameter, $0 \leq b \leq R_0$. It can be seen that the analytic model reproduces the probability distribution over the final rotational quantum numbers quite well, although it underpredicts the probability for small changes in the rotational quantum number, $j-j_0$. Figure I.2 plots analytic and numerical rotational transition probabilities, averaged over the impact parameter, for different values of the initial rotational energy. One can see that the probability distribution over the final rotational quantum number is reproduced well by the analytic model, except for the case of a high rotational energy / low translational kinetic energy, $E_r / E_t = 3/4$, ($E_r / E_t = 3$). Basically, the trajectory calculations demonstrate that, as expected, rapidly rotating molecules with low translational energies behave as nearly isotropic particles (near “breathing spheres”), which makes rotational energy transfer very inefficient, such that the transition probability drops rapidly with $\Delta j=j_0-j$. For these trajectories, the approximate analytic expression for the trajectory integral S , given by Eq. (I.3a), becomes less accurate (see Fig. I.2(d)). Figure I.3 compares the transition probabilities averaged over the impact parameter and initial rotational quantum numbers (assumed to be distributed randomly between $j_0=0$ and $j_{0,\max}$),

$$\langle P(\Delta j, E_t) \rangle = \frac{\sum_{j_0=0}^{j_{0,\max}} (2j_0 + 1) P(j_0 \rightarrow j, E_t)}{(j_{0,\max} + 1)^2}. \quad (\text{I.12})$$

for different values of the total collision energy. Again, it is apparent that the analytic model prediction for the rotational energy transfer probability distribution over $\Delta j = j_0 - j$ is in good agreement with the results of the trajectory calculations, over a wide range of total collision energies, $E_t = 10^3$ - 10^5 cm⁻¹ ($E_t \approx 0.12$ - 12.0 eV). A closer look shows that at high collision energies, the analytic model underpredicts the average probability for the molecule to remain on the same rotational level, such that $\Delta j = j_0 - j = 0$, and overpredicts average probabilities of transitions with $\Delta j \neq 0$. Further analysis shows that this occurs due to the contribution of molecules with high initial rotational energies (high j_0 values), i.e. low translational energies, $E_k=E_t - E_{r0}$, for which the analytic model predictions are less accurate (see Fig. I.2(d)). Finally, the “pointed arch” shaped probability distributions plotted in Fig. I.3 demonstrate that the use of linear or Gaussian scaling for rotational energy transfer probabilities, $\ln[P(j_0 \rightarrow j)] \sim -A|j_0-j|$ or $\ln[P(j_0 \rightarrow j)] \sim -A(j_0-j)^2$, would be simplistic and is not justified. Basically, for initially rapidly rotating molecules (high j_0), the “spread” over the final rotational quantum numbers is much narrower compared to the molecules with lower initial rotational energies (e.g. compare Figs. I.2(c) and I.2(d)), which produces the pointed arch shape of $P(\Delta j)$ distributions shown in Fig. I.3.

Figures I.4,5 compare the rotational transition probabilities in molecule-molecule collisions, for different initial rotation energies (Fig. I.4), and different total collision energies (Fig. I.5), showing trends similar to the ones for atom-molecule collisions. These plots demonstrate that the effect of rotation of the “projectile” molecule on rotational energy transfer in the “target” molecule is accounted for by reducing the total collision energy available for the translational motion (by a parameter ξ in Eq. (I.3a)). This also shows that, in the first approximation, the probabilities for simultaneous rotational energy transfer in both collision partners can be factorized as follows, $P(j_0 \rightarrow j, j_0' \rightarrow j') \approx P(j_0 \rightarrow j) \cdot P(j_0' \rightarrow j')$.

Figure I.6 plots RMS average rotational energy transferred per collision vs. total collision energy, both for atom-molecule and molecule-molecule. The results of the analytic model, plotted in Fig. I.6, have been corrected for the variation of the closest approach distance (i.e. total collision cross section) with the total collision energy, given by Eq. (I.7), such that ΔE_r^{RMS} predicted by the analytic model (see Eq. (I.5)) slightly decreases with the collision energy,

$$\frac{\Delta E_r^{\text{RMS}}(E_t)}{E_t} = \frac{\xi}{8} \frac{R_0(E_t)}{2.5 \text{ \AA}}. \quad (\text{I.13})$$

in good agreement with the trajectory calculations. Summarizing, the results shows in Figs. I.1-6 demonstrate that the present analytic model of rotational energy transfer is in good agreement with atom-molecule and molecule-molecule trajectory calculations, reproducing accurately the dependence of state-specific rotational energy transfer probabilities on the change of rotational quantum number during collision ($j-j_0$), impact parameter, initial rotational energy ($E_{r0}=Bj_0^2$) , and total collision energy (E_t).

RMS average rotational energy transferred per collision, ΔE_r^{RMS} , can be related to the rotational relaxation collision number, Z_{rot} , as follows [35]:

$$\frac{1}{Z_{rot}} = \frac{\pi}{4} \frac{\eta}{P \tau_{rot}} \approx \frac{5\pi}{16} \frac{\left\langle \left\langle \frac{\Delta E_r^2(T)}{T^2} \right\rangle \right\rangle}{\left\langle \left\langle \frac{E_{k0}^2 \sin^2 \chi}{T^2} \right\rangle \right\rangle} \approx \frac{\int_0^\infty \frac{\left\langle \Delta E_r^2(E_t) \right\rangle}{T^2} \left(\frac{\bar{E}_t}{T} \right)^n \exp\left(-\frac{\bar{E}_t}{T}\right) d\left(\frac{\bar{E}_t}{T}\right)}{\int_0^\infty \frac{\left\langle E_{k0}^2 \sin^2 \chi \right\rangle}{T^2} \left(\frac{\bar{E}_t}{T} \right)^n \exp\left(-\frac{\bar{E}_t}{T}\right) d\left(\frac{\bar{E}_t}{T}\right)}. \quad (\text{I.14})$$

In Eq. (I.14), η and τ_{rot} are dynamic viscosity and rotational relaxation time, respectively,

$$\eta \approx \frac{5kT}{8 \left\langle \left\langle \frac{E_{k0}^2 \sin^2 \chi}{T^2} \right\rangle \right\rangle}, \quad (\text{I.15})$$

$$\tau_{rot} = \frac{1}{2N \left\langle \left\langle \frac{\Delta E_r^2(T)}{T^2} \right\rangle \right\rangle} = \frac{kT}{2P \left\langle \left\langle \frac{\Delta E_r^2(T)}{T^2} \right\rangle \right\rangle}, \quad (\text{I.16})$$

E_{k0} is the initial translational kinetic energy, χ is the scattering angle, $n=2$ for atom-molecule and $n=3$ for molecule-molecule collisions. For atom-molecule collisions,

$$\left\langle E_{k0}^2 \sin^2 \chi \right\rangle \approx \left(\frac{3}{5}\right)^2 E_t^2 \left\langle \sin^2 \chi \right\rangle \approx \frac{1}{2} \left(\frac{3}{5}\right)^2 E_t^2. \quad \text{For molecule-molecule collisions,}$$

$\left\langle E_{k0}^2 \sin^2 \chi \right\rangle \approx \frac{1}{2} \left(\frac{3}{7}\right)^2 E_t^2$. Combining this with the expression for the average squared rotational energy transfer, $\left\langle \Delta E_r^2 \right\rangle = \left(\frac{\xi}{8}\right)^2 E_t^2$ (see Eq. (I.5)), we obtain

$$Z_{rot}^{A-M} \approx \frac{1}{2} \left(\frac{24}{5}\right)^2 \approx 12, \quad Z_{rot}^{M-M} \approx \frac{1}{\xi^2} \frac{1}{2} \left(\frac{24}{7}\right)^2 \approx 8.5, \quad (\text{I.17})$$

both values nearly independent of temperature. These results are in good agreement with the present trajectory calculations, which predict $Z_{rot}^{M-M} \approx 10 \approx const$ for the repulsive exponential potential used, in the range of T=300-5000 K (see Fig. I.7). Figure I.7 plots Z_{rot} for nitrogen, predicted using DIDEX for a purely repulsive exponential potential with $\alpha=4.0 \text{ \AA}^{-1}$ [29,30] and for an attractive-repulsive potential [10]. It can be seen that the effect of molecular attraction, which may considerably reduce the collision number, is significant only at fairly low temperatures, below T~1000 K. Figure I.7 also plots the rotational collision number predicted by molecular dynamics (MD) [38] calculations, using a more accurate Lennard-Jones potential energy surface. One can see that Z_{rot} predicted by MD calculations is approximately 30% lower than the values predicted by the semiclassical code using the potential from [10], although both models exhibit the same trend for Z_{rot} to level off at high temperatures, when the effect of attractive forces becomes insignificant.

To estimate the sensitivity of the rotational collision number to the uncertainty in the repulsive exponential potential parameter α , Fig. I.8 plots Z_{rot} , as well as RMS average values of $\langle \Delta E_r^2 \rangle^{1/2}$ and $\langle E_{k0}^2 \sin^2 \chi \rangle^{1/2}$, calculated for a purely repulsive potential at $E_t=10^4 \text{ cm}^{-1}$, vs. α . The results of these calculations show that varying the potential parameter primarily affects the viscosity, while the RMS rotational energy transfer per collision remains nearly constant over a wide range of repulsive intermolecular potentials. As a result, the collision number decreases as α increases and the potential approaches the hard spheres potential, approaching the asymptotic value of $Z_{rot} \approx 4$. Thus, lower values of Z_{rot} predicted in Ref. [37] are likely due to a stiffer repulsive potential (i.e. larger effective value of α) used. Finally, Fig. I.8 illustrates that rotational energy transfer at high temperatures is indeed almost insensitive to the intermolecular potential, as long as $1/\alpha \ll R_0$, in good agreement with the present analytic model, $\langle \Delta E_r^2 \rangle^{1/2} / E_t = \frac{\xi}{8} \approx 0.1$. The results of Figs. I.7, I.8 demonstrate that, as expected, the use of a simple repulsive exponential potential to predict rotational relaxation at high temperatures (above $T \sim 1000 \text{ K}$) is fully justified.

The present rotational relaxation model reproduces the effect of rotational-translational nonequilibrium on rotational relaxation time, discussed in detail in Ref. [39]. Figure I.9 plots the average squared rotational energy transferred in atom-molecule collisions, $\langle \Delta E_r^2 \rangle$, at the conditions when the ratio of the initial rotational energy to the total collision energy, E_{r0}/E_t , is fixed, normalized on its value in equilibrium, $\langle \Delta E_r^2 \rangle_{eq}$, i.e. when the initial rotational energy is randomly distributed between 0 and E_t , at $E_t=10^3 \text{ cm}^{-1}$. The results are shown both for the analytic model and for trajectory calculations. From Fig. I.9, it can be seen that $\langle \Delta E_r^2 \rangle$ in collisions of non-rotating molecules ($E_{r0}/E_t=0$) is significantly higher than the equilibrium value, by about a factor of two. On the other hand, $\langle \Delta E_r^2 \rangle$ in collisions of rapidly rotating molecules ($E_{r0}/E_t \rightarrow 1$) is much lower compared to the equilibrium value, as expected based on the results of Fig. I.2. Since the rotational relaxation time is inversely proportional to $\langle \Delta E_r^2 \rangle$ (see Eq. (I.16)), τ_{rot} in collisions of initially non-rotating molecules will be shorter than near rotational equilibrium, by approximately a factor of two at this collision energy, and τ_{rot} in collisions of rapidly rotating molecules will be significantly longer, consistent with the predictions of the molecular dynamics model of Ref. [39].

Figure I.10 compares V-R-T transition probabilities in atom-molecule collisions, averaged over the impact parameter and initial rotational quantum numbers (assumed to be distributed randomly between $j_0=0$ and $j_{0,max}$, as has been done for purely rotational relaxation in Fig. I.3),

$$\langle P_{VRT}(\Delta j, v \rightarrow w, E_t) \rangle = \frac{\sum_{j_1=0}^{j_{1,max}} (2j_1+1) P_{VRT}(v, j_1 \rightarrow w, j_2, E_t)}{(j_{1,max}+1)^2}. \quad (\text{I.18})$$

for different values of the total collision energy. The plots shown in Fig. I.10 are for vibrational transitions for $\Delta v=w-v=0-3$, i.e. from $v=0$ to $w=0-3$. Once again, the analytic model prediction for the V-R-T probability distribution over $\Delta j = j_0 - j$ is in good agreement with the results of the trajectory calculations, over a wide range of total collision energies, $E_t = 10^3-10^5 \text{ cm}^{-1}$ ($E_t \approx 0.12-12.0 \text{ eV}$). In Figure I.10, significant separation between the distributions of V-R-T probabilities over the rotational quantum number change at $E_t < 10^5 \text{ cm}^{-1}$ is due to V-T probabilities in this range of total collision energies being very low, $P(v=0 \rightarrow w=0) \gg P(v=0 \rightarrow w=1) \gg P(v=0 \rightarrow w=2) \gg P(v=0 \rightarrow w=3)$. Note that the “pointed arch” distribution observed for purely rotational relaxation, $P(v=0, j_1 \rightarrow w=0, j_2)$, is not

duplicated for V-R-T relaxation processes, $P(v=0, j_1 \rightarrow w=1-3, j_2)$, in the collision energy range $E_t \sim 10^3 - 3 \cdot 10^4 \text{ cm}^{-1}$ (see Fig. I.10). A more detailed analysis shows that this effect is due to contribution of molecules with very high initial rotational energies (j_0 values), i.e. near “breathing spheres”, for which V-T probabilities are significantly lower than for moderately rotating molecules, due to absence of strong modulation of the interaction potential by rotational motion [29,30]. At a high collision energy, $E_t = 10^5 \text{ cm}^{-1}$, this effect is no longer very pronounced, and distributions over $\Delta j = j_0 - j$ become more similar, for both pure R-T and V-R-T relaxation processes. The difference in shape between analytic and trajectory V-R-T probability distributions over Δj for $\Delta v=1-3$ at $E_t=3 \cdot 10^4 \text{ cm}^{-1}$, evident from Fig. I.10, is caused by factorization of V-R-T transition probabilities into R-T and V-T probabilities in Eq. (I.8), $P_{VRT}(v, j_1 \rightarrow w, j_2) = P_{RT}(j_1 \rightarrow j_2) \cdot P_{VT}(v \rightarrow w)$, since both purely R-T analytic probabilities, obtained in the present work, and “free rotation” V-T analytic probabilities, predicted in Ref. [29], are in very good agreement with trajectory calculations.

Figure I.11 plots V-R-T transition probabilities in molecule-molecule collisions, averaged over the impact parameter and initial rotational quantum numbers of the target molecule, as given by Eq. (I.18), as well as over initial and final rotational quantum numbers of the projectile molecule, as given by Eq. (I.11a). Figure I.11 shows the results obtained only for three values of total collision energy, $E_t = 10^4$, $3 \cdot 10^4$, and 10^5 cm^{-1} , since extensive trajectory calculations for molecule-molecule collisions necessary to accumulate sufficient statistics for individual vibrational-rotational transitions (10^5 trajectories in Fig. I.11) are computationally expensive, especially at low collision energies. From Fig. I.11, it can be seen that the difference between analytic and trajectory V-R-T probability distributions over Δj for $\Delta v=1-3$ at $E_t=3 \cdot 10^4 \text{ cm}^{-1}$, also apparent from Fig. I.10, becomes more pronounced. Also, at $E_t=10^5 \text{ cm}^{-1}$ it is clear that the present model overestimates rotational energy transfer probabilities for $\Delta v=0$ and underestimates them for $\Delta v=3$, although V-T probabilities for transitions $\Delta v=0-3$ (summed over the rotational quantum numbers) at this energy are predicted quite accurately, within $\sim 30\%$. More detailed analysis shows that this effect is due to contribution of rotational energy transfer in the “projectile” molecule to the vibrational excitation of the “target” molecule at high collision energies, which so far has not been accounted for in the present model.

Figure I.12 compares V-T transition probabilities in atom-molecule collisions (i.e. V-R-T probabilities for $\Delta v=0-3$ plotted in Fig. I.10, averaged over the impact parameter as well as over initial and final rotational quantum numbers),

$$\langle P_{VT}(v \rightarrow w, E_t) \rangle = \sum_{j_2=0}^{j_{2,\max}} \frac{\sum_{j_1=0}^{j_{1,\max}} (2j_1 + 1) P_{VRT}(v, j_1 \rightarrow w, j_2, E_t)}{(j_{1,\max} + 1)^2}, \quad (\text{I.19})$$

vs. total collision energy. As expected, the agreement between the analytic model and the trajectory calculations is quite good, over a wide range of total collision energies, $E_t = 10^3 - 10^6 \text{ cm}^{-1}$. Again, the difference between the analytic and numerical probabilities is due to V-R-T probability factorization in Eq. (I.8), i.e. not accounting for full coupling between rotational and vibrational modes. As can be seen from Fig. I.13, which compares atom-molecule V-T transition probabilities for $v=40 \rightarrow w=35-40$ ($\Delta v=v-w=0-5$), similar level of agreement is obtained for V-T transitions of initially highly vibrationally excited molecules, for $v>0$. Figure I.14 plots the same results for molecule-molecule collisions, for which the agreement with the trajectory calculations is not as good, especially for multiquantum transitions with $\Delta v=3$, where additional analysis is needed to account for coupling between vibrational and rotational modes. The results of Figs. I.12 - I.14 demonstrate that the present analytic model generates a complete, self-consistent set of V-R-T transition probabilities in atom-molecule and molecule-molecule collisions, $P_{VRT}(v, j_1 \rightarrow w, j_2)$, predicting vibrational and rotational energy transfer vs. total collision energy, as well as initial and final vibrational and rotational quantum numbers. Although the present results are obtained for purely repulsive interaction potential, they are fully applicable for modeling of

nonequilibrium flows behind strong shock waves, when the effect of attractive forces on energy transfer rates is negligible.

I.4. Conclusions

A three-dimensional semiclassical analytic model of vibrational energy transfer in collisions between a rotating diatomic molecule and an atom, and between two rotating diatomic molecules (Forced Harmonic Oscillator – Free Rotation model), has been extended to incorporate rotational relaxation and coupling between vibrational, translational and rotational energy transfer. The model is based on analysis of classical trajectories of rotating molecules interacting by a repulsive exponential atom-to-atom potential. The model predictions are compared with the results of three-dimensional close-coupled semiclassical trajectory calculations using the same potential energy surface. The comparison demonstrates good agreement between analytic and numerical probabilities of rotational and vibrational energy transfer processes, over a wide range of total collision energies, rotational energies, and impact parameter. Specifically, rotational relaxation time (RMS average rotational energy transferred) predicted by the present model is within 10-20% of trajectory calculation results for the same interaction potential, and individual R-T relaxation probabilities are typically within 50-100% of the trajectory calculation results, except for collisions of very rapidly rotating molecules. For V-R-T relaxation probabilities, the difference between the present model predictions and the trajectory calculations is within a factor of 2 for atom-molecule collisions and up to about a factor of 3 for multi-quantum transitions in molecule-molecule collisions. The main source of the difference is the approximate nature of coupling between vibrational energy mode and rotational energy modes of one or two collision partners, assumed in the present approach. The model predicts probabilities of single-quantum and multi-quantum vibrational-rotational transitions and is applicable up to very high collision energies and quantum numbers. Closed-form analytic expressions for these transition probabilities lend themselves to straightforward incorporation into DSMC nonequilibrium flow codes.

Future work will focus on taking into account coupling between vibrational and rotational energy modes of both colliding molecules and predicting state-specific rates of molecular dissociation from highly excited vibrational-rotational energy states. Also, detailed comparison with state-specific V-R-T databases for N₂-N [18-21] and N₂-N₂, obtained using *ab initio* potential energy surfaces, is desirable. Although vibrational and rotational energy transfer at high collision temperatures is likely to be dominated by the repulsive part of the interaction potential, such as used in the present work, the role of atom exchange reactions at these conditions may well be significant, and needs to be quantified.

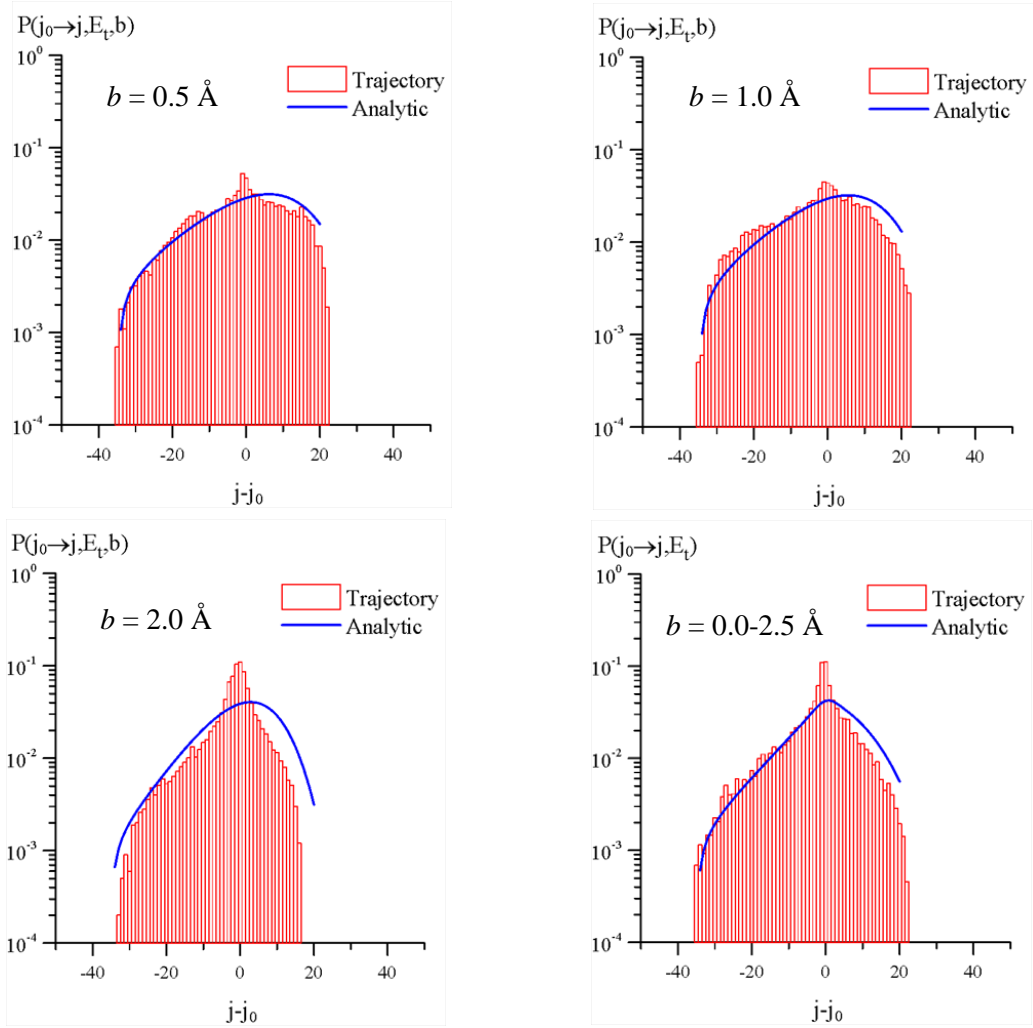


Figure I.1. Comparison of analytic and numerical (10^4 trajectories) rotational energy transfer probabilities, for different impact parameter values. Atom-molecule, $E_t = 10^4 \text{ cm}^{-1}$, $E_r / E_t = 1/4$, $b = 0.5 \text{ \AA}$, 1.0 \AA , 2.0 \AA , and averaged over $0.0-2.5 \text{ \AA}$.

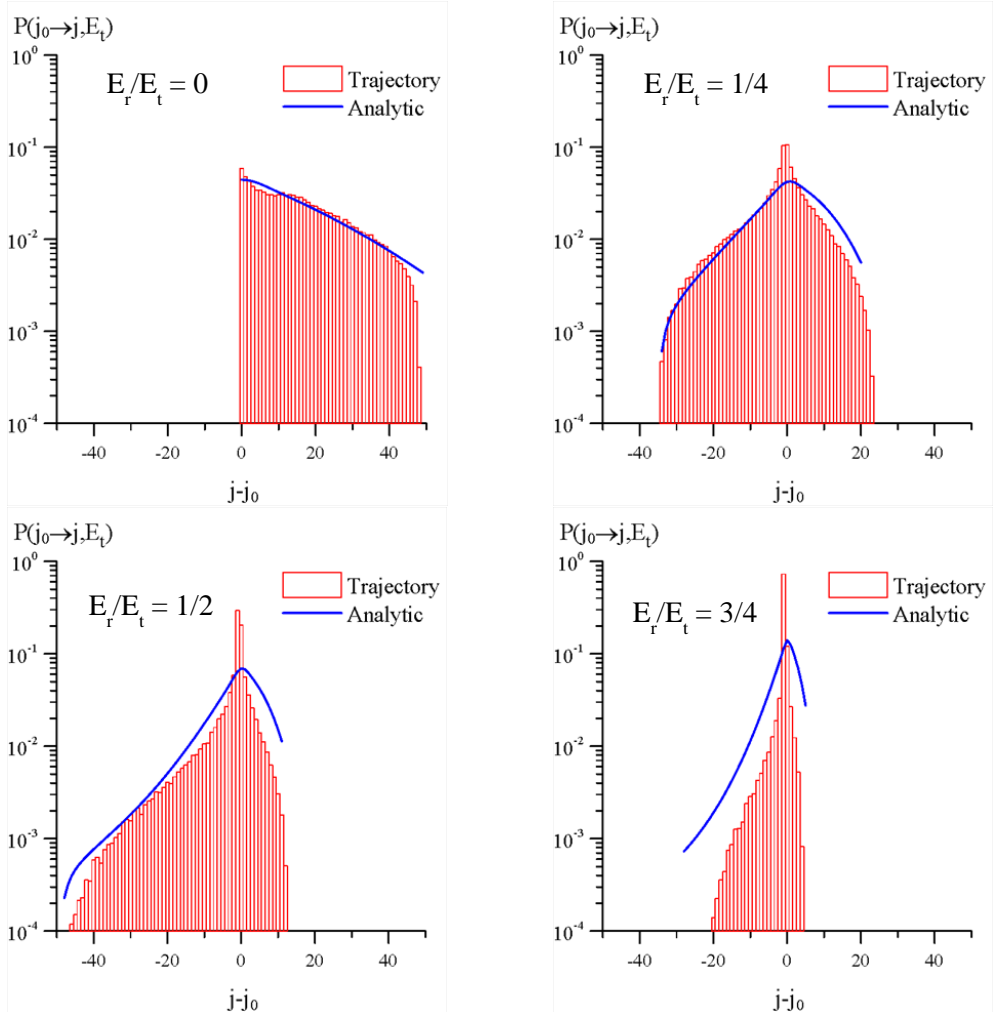


Figure I.2. Comparison of analytic and numerical (10^5 trajectories) rotational energy transfer probabilities averaged over the impact parameter, for different initial rotational energies. Atom-molecule, $E_t = 10^4 \text{ cm}^{-1}$, $E_r / E_t = 0, 1/4, 1/2$, and $3/4$.

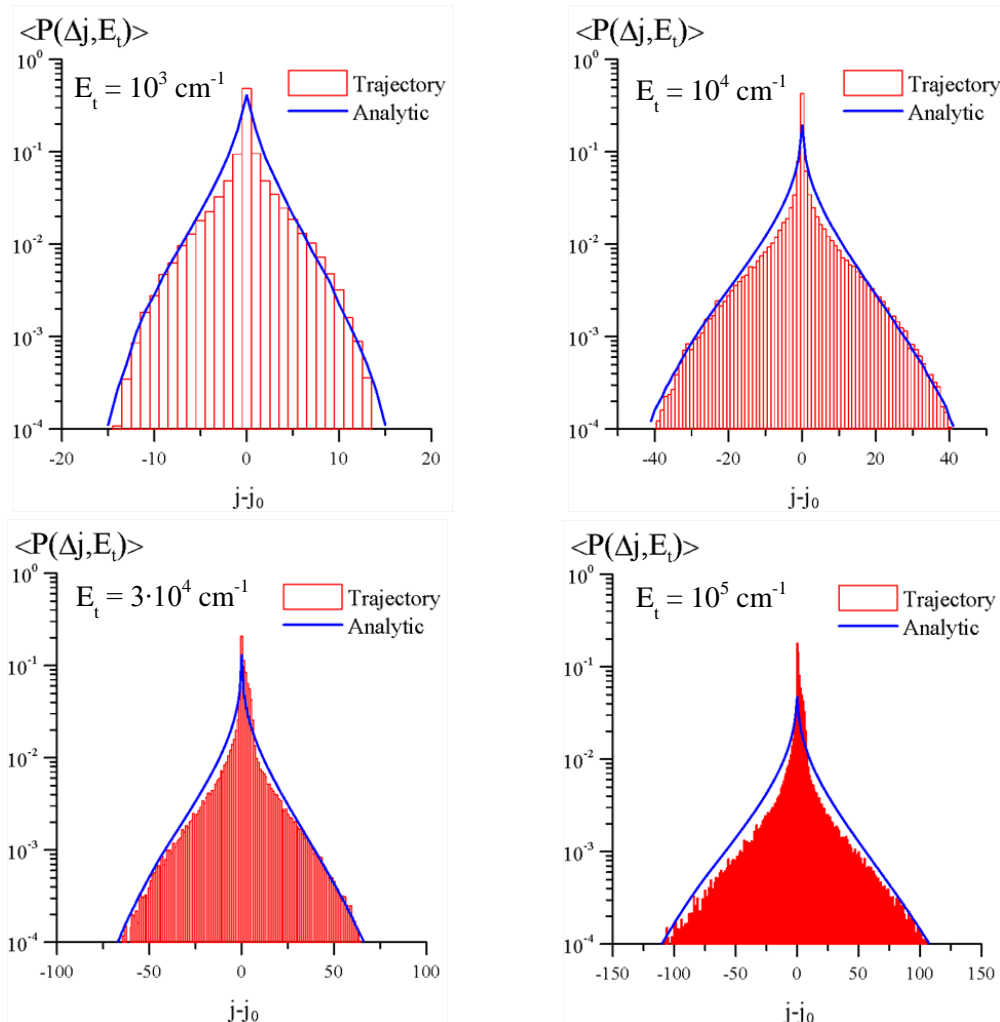


Figure I.3. Comparison of analytic and numerical (10^5 trajectories) rotational energy transfer probabilities averaged over the impact parameter and rotational energies, for different total energies. Atom-molecule, $E_t = 10^3, 10^4, 3 \cdot 10^4$, and 10^5 cm^{-1} .

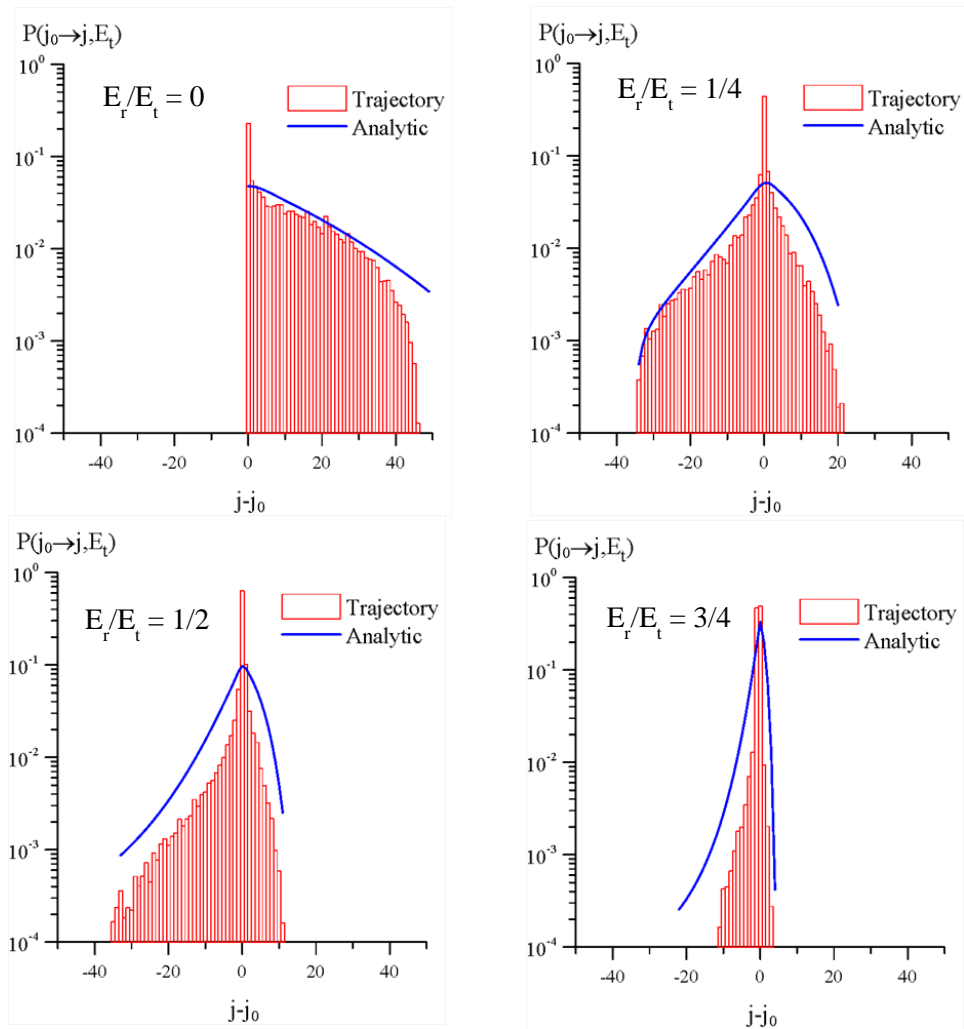


Figure I.4. Comparison of analytic and numerical (10^4 trajectories) rotational energy transfer probabilities averaged over the impact parameter, for different initial rotational energies. Molecule-molecule, $E_t = 10^4 \text{ cm}^{-1}$, $E_r / E_t = 0, 1/4, 1/2$, and $3/4$.

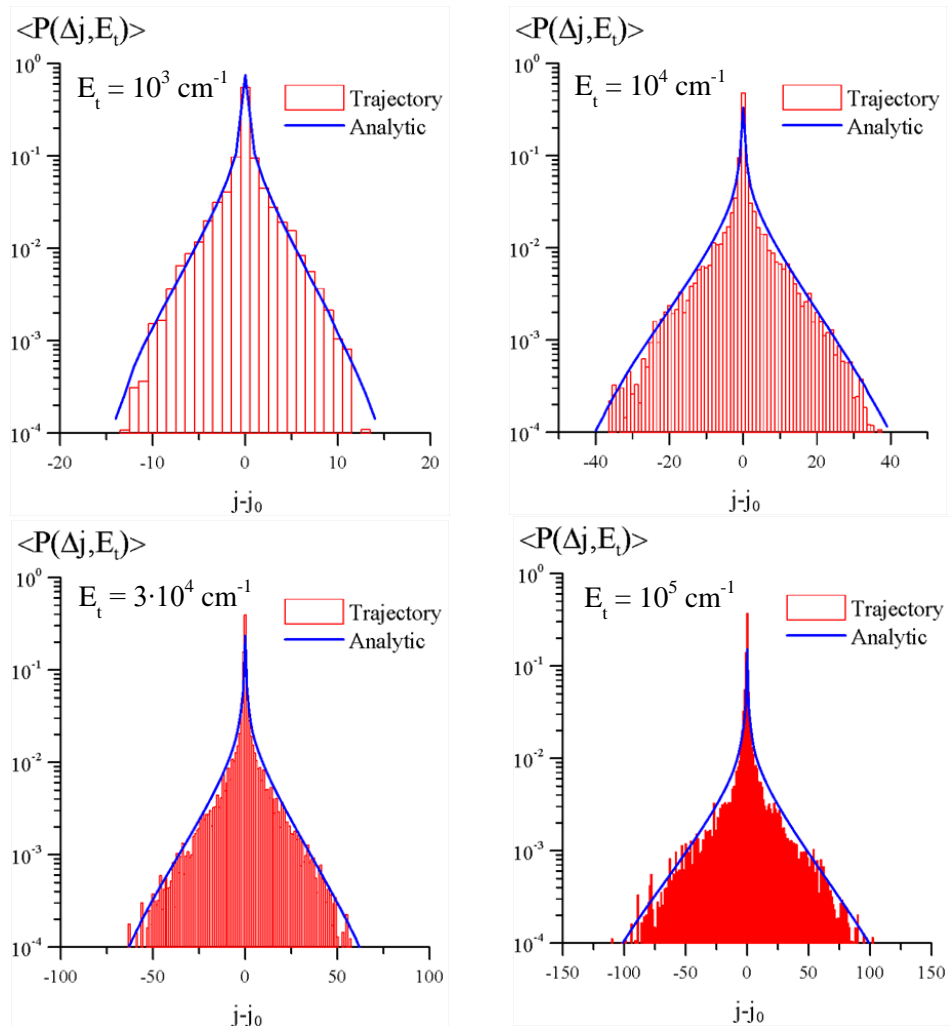


Figure I.5. Comparison of analytic and numerical (10^5 trajectories) rotational energy transfer probabilities averaged over the impact parameter and rotational energies, for different total energies. Molecule-molecule, $E_t = 10^3, 10^4, 3 \cdot 10^4$, and 10^5 cm^{-1} .

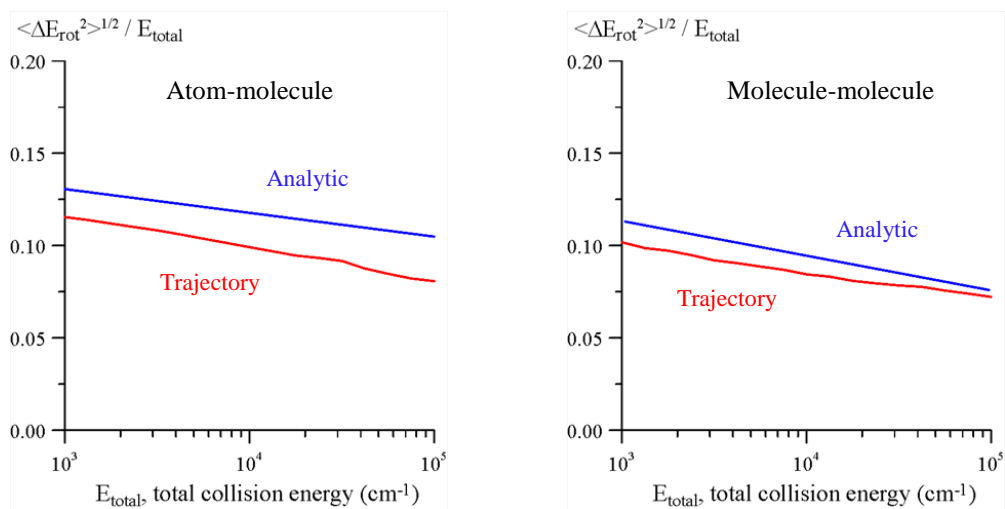


Figure I.6. Comparison of analytic and numerical RMS average rotational energy transferred per collision. Left: atom-molecule, right: molecule-molecule.

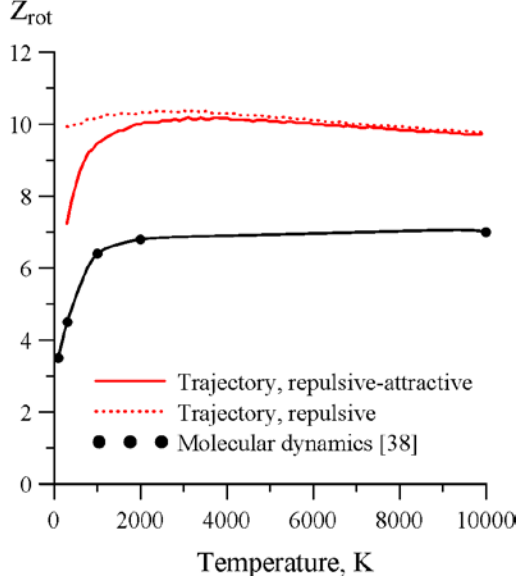


Figure I.7. Comparison of rotational collision number in nitrogen predicted by the present trajectory calculations with previous results.

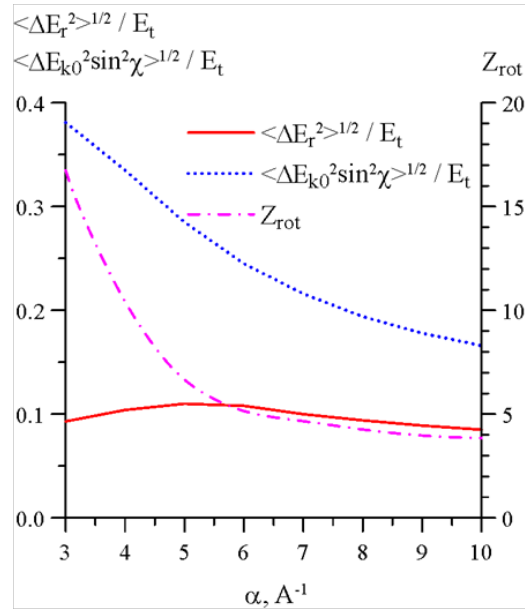


Figure I.8. Effect of repulsive potential parameter α on rotational collision number, and on rotational and translational energy transfer in nitrogen. $E_t=10^4 \text{ cm}^{-3}$.

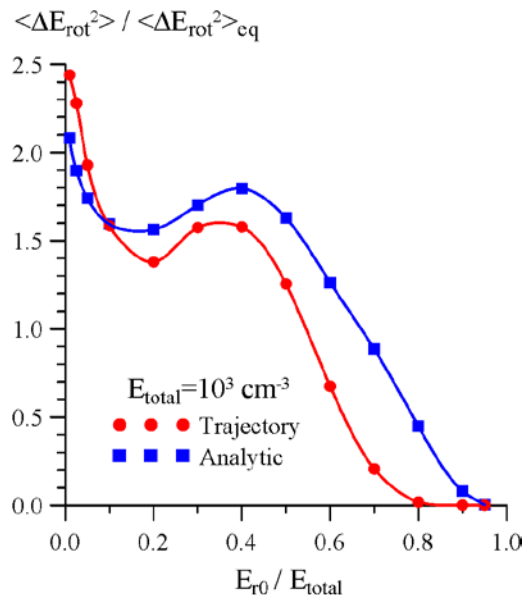


Figure I.9. Average squared rotational energy transferred in atom-molecule collisions, normalized on its value in equilibrium, vs. ratio of the initial rotational energy to the total collision energy, E_{r0}/E_t . $E_t=10^3 \text{ cm}^{-1}$.

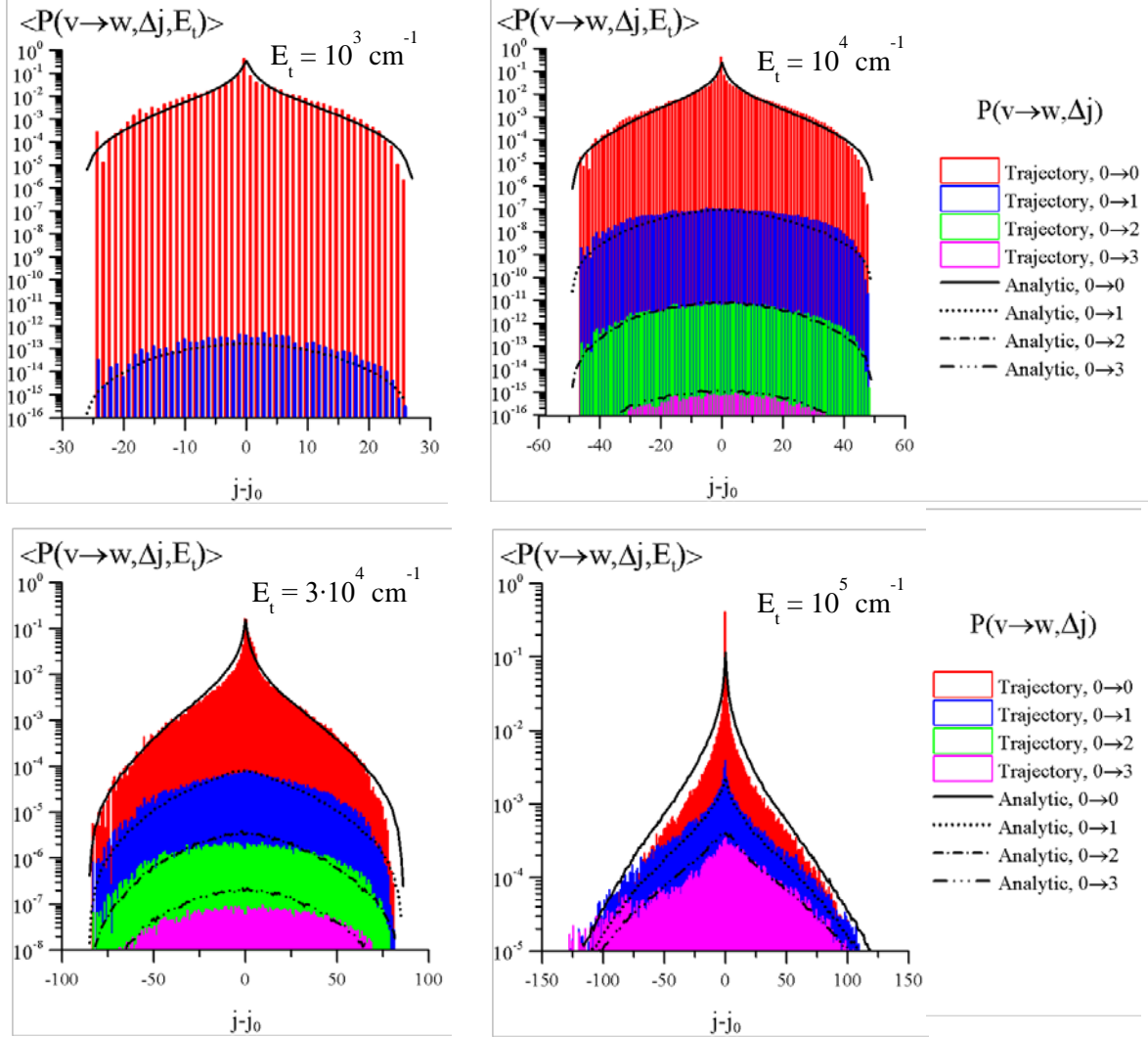


Figure I.10. Comparison of analytic and numerical (10^5 trajectories) V-R-T energy transfer probabilities ($v=0 \rightarrow w=0-3$), averaged over the impact parameter and initial rotational quantum numbers, for different total energies. Atom-molecule, $E_t = 10^3, 10^4, 3 \cdot 10^4$, and 10^5 cm^{-1} .

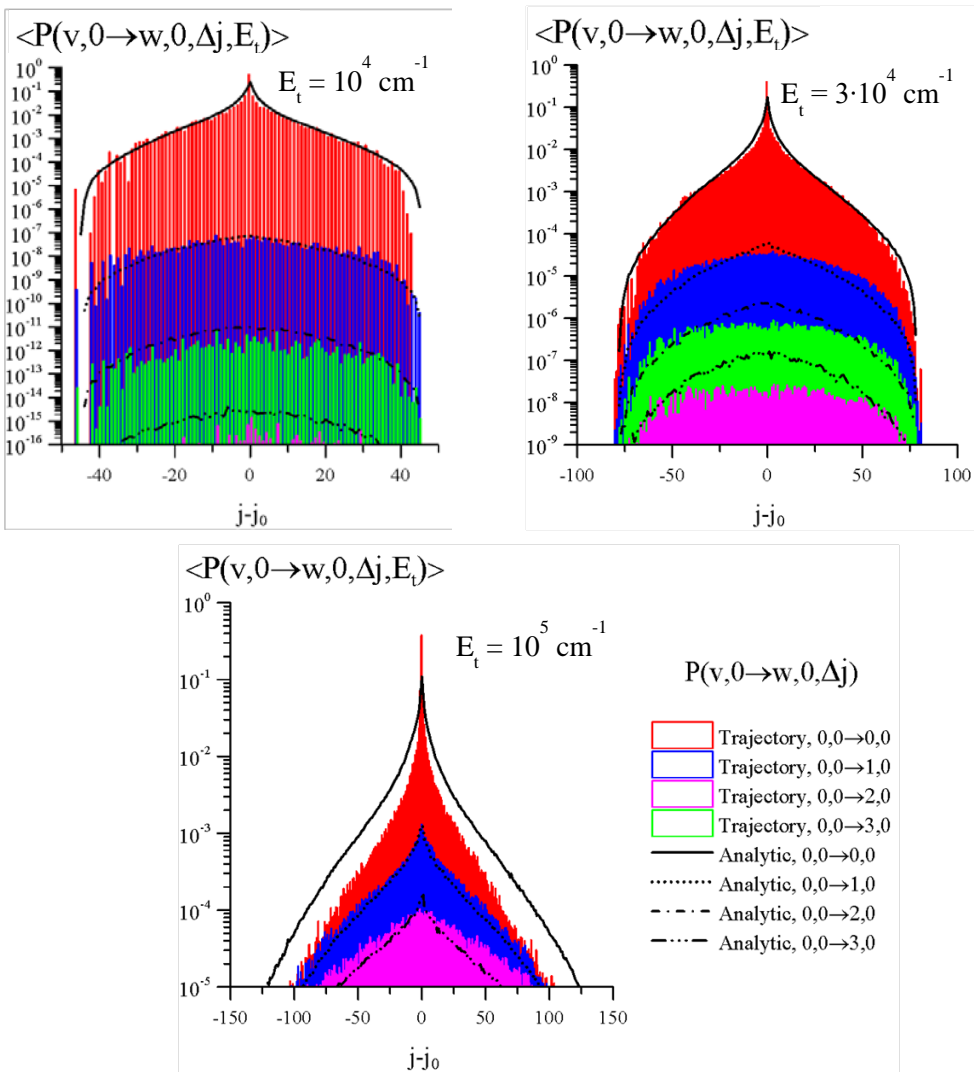


Figure I.11. Comparison of analytic and numerical (10^5 trajectories) V-R-T energy transfer probabilities ($v=0 \rightarrow w=0-3$, $v'=w'=0$), averaged over the impact parameter and initial quantum numbers, for different total energies. Molecule-molecule, $E_t = 10^4$, $3 \cdot 10^4$, and 10^5 cm^{-1} .

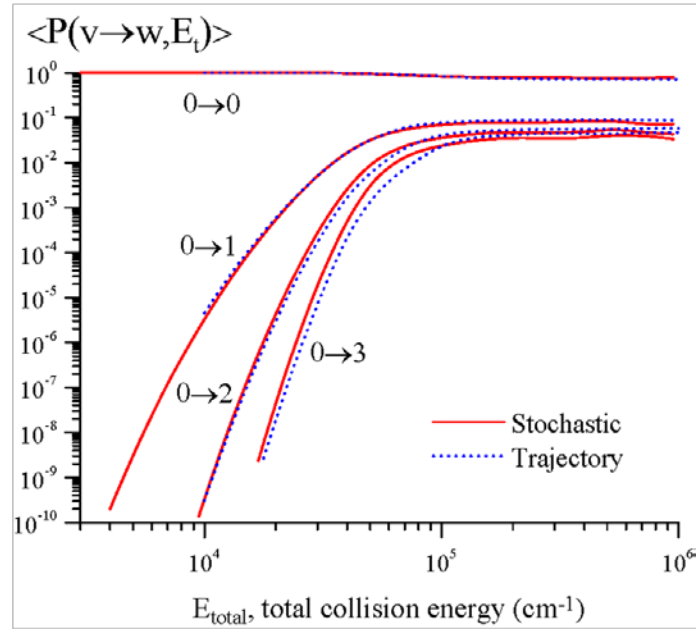


Figure I.12. Comparison of analytic and numerical (10^4 trajectories) V-T energy transfer probabilities in atom-molecule collisions ($v=0 \rightarrow w=0-3$), averaged over the impact parameter as well as initial and final rotational quantum numbers, vs. total collision energy.

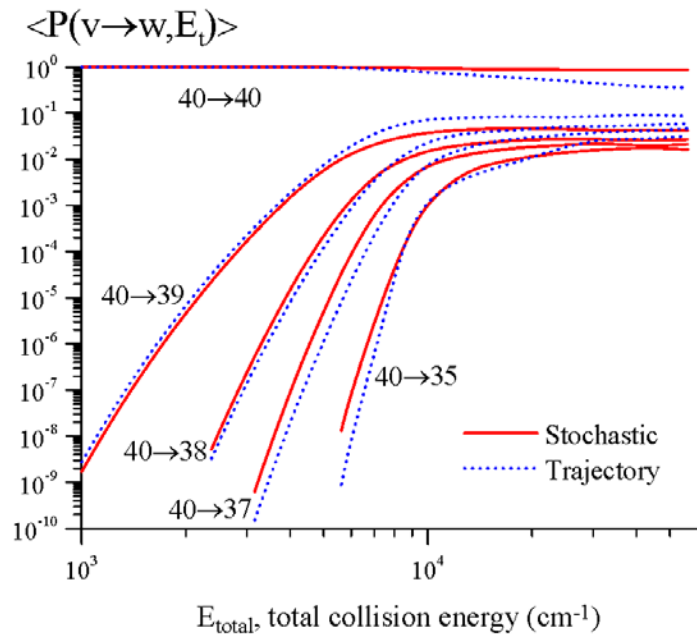


Figure I.13. Comparison of analytic and numerical (10^4 trajectories) V-T energy transfer probabilities in atom-molecule collisions ($v=40 \rightarrow w=35-40$), averaged over the impact parameter as well as initial and final rotational quantum numbers, vs. total collision energy.

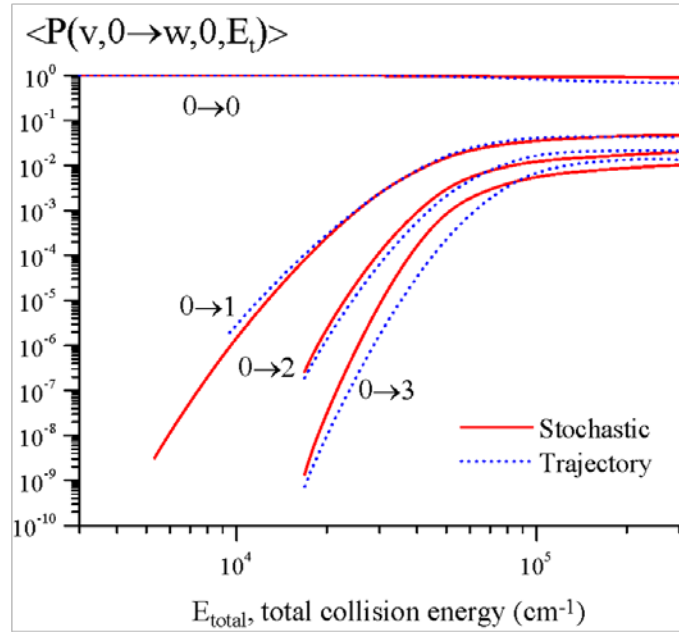


Figure I.14. Comparison of analytic and numerical (10^4 trajectories) V-T energy transfer probabilities in molecule-molecule collisions ($v=0 \rightarrow w=0-3$, $v'=w'=0$), averaged over the impact parameter as well as initial and final rotational quantum numbers, vs. total collision energy.

II. Kinetics of Excited States and Radicals in a Nanosecond Pulse Discharge and Afterglow in Nitrogen and Air

II.1. Introduction

High voltage nanosecond pulse discharges have received considerable attention over the recent decade, both from the viewpoint of fundamental kinetics of breakdown development, molecular energy transfer, and plasma chemical reactions, and due to a number of engineering applications, such as plasma-assisted combustion [40-42], high-speed flow control [43-45], and biological applications [46]. It is well known that short pulse duration prevents development of discharge instabilities and that high peak reduced electric field during the pulse results in efficient generation of electronically excited species and molecular dissociation [47]. Also, short pulse duration makes possible time-resolved studies of rapid energy transfer processes and reactions of excited electronic species and radicals in the afterglow. Over the last decade, there have been numerous studies of nanosecond pulse discharges operated in molecular gases, both theoretical [48-52] and experimental [53-57], to name just a few.

The focus of the present work is on a kinetic modeling study of a high peak voltage, nanosecond pulse duration (~ 200 ns), “diffuse filament” discharge generated between two spherical copper electrodes in nitrogen and dry air. This type of discharge has been studied in our recent work [58,58]. Ref. [59], closely related to the present work, reports time-resolved measurements of temperature, N_2 vibrational level populations, and absolute number densities of N, O, and NO, demonstrating significant N_2 vibrational excitation and radical species generation in plasma chemical reactions during the discharge pulse and the afterglow. Short pulse duration used in these experiments “separates” in time electron impact vibrational excitation of nitrogen during the pulse from vibration-vibration (V-V) energy exchange in collisions of nitrogen molecules, occurring on a longer time scale, ~ 1 - 100 μ s [60]. At these conditions, vibration-translation (V-T) relaxation does not affect N_2 vibrational level populations, except for very long time delays after the discharge pulse in air, ~ 1 ms. In Ref. [59], time-resolved N, O, and NO number densities have been measured in the afterglow, ~ 5 μ s to ~ 10 ms after the discharge pulse, i.e. on the time scale when most excited electronic species generated during the pulse have been quenched. Kinetic model analysis of time-resolved measurements of temperature and multiple key species concentrations in the afterglow, over a wide range of time scales, provides an opportunity to obtain new quantitative insight into kinetics of plasma chemical reactions.

The main objective of the present work is to elucidate the kinetic mechanisms of ground state N, O, and NO formation and decay in the discharge and in the afterglow, and to determine which excited states generated in the discharge, but not measured directly, are among the dominant “precursors” of these species. Section II.2 describes the kinetic model of a nanosecond pulse discharge in nitrogen and dry air. Section II.3 compares the kinetic modeling predictions with the experimental results of Ref. [59]. Finally, Section II.4 summarizes the results.

II.2. Kinetic Model

Kinetic modeling of the discharge pulse and the afterglow was carried out using a one-dimensional model discussed below. A schematic of the discharge filament sustained between two spherical electrodes is shown in Fig. II.1. One of the electrodes is grounded and the other is powered by a positive polarity high voltage pulse. In the experiments [58,59], the diameter of the electrodes is 8 mm and the distance between the electrodes is 10 mm. The apparent diameter of the discharge filament, determined from ICCD images of broadband UV/visible emission of the plasma [59], is approximately $d=2.1$ mm. In the experiments, the discharge filament is located in the center, along the axis of symmetry of the electrodes, as shown schematically in Fig. II.1. Since the diameter of the electrodes is much larger compared to the filament diameter, the electrode curvature has almost no effect on discharge parameters. The radial fluxes of charged species during the discharge pulse (pulse duration of about 200 ns) are much

lower compared to the axial fluxes, except for a thin region in the cathode layer. At these conditions, the discharge parameters (such as the electric field and the rate of ionization) are controlled by the transport of charged species in the axial direction. This justifies the use of a one-dimensional pulsed discharge model, with the spatial coordinate, z , perpendicular to the electrode surfaces, as shown in Fig. II.1. The model assumes constant volume conditions during the discharge pulse and constant pressure conditions after the voltage is turned off. Since gas temperature rise during the pulse is insignificant, except in the cathode layer, where considerable increase of gas temperature is caused by rapid energy transfer from ions to neutrals, this approach does not result in a significant pressure increase in the afterglow. The simulations were carried out in nitrogen and in dry air, modeled as a 78.5% N_2 / 21.5% O_2 mixture at a pressure of 100 Torr.

The kinetic model used in the present work includes time-dependent conservation equations for the number densities of electrons, ions (positive and negative ions in air), and neutral species; equation for the electron temperature; Poisson equation for the electric field; and heavy species energy equation. In nitrogen, the model includes N^+ , N_2^+ , N_3^+ , and N_4^+ ions. In air, the following ions are added: O^- , O_2^- , O_3^- , O_4^- , NO^- , N_2O^- , NO_2^- , O^+ , O_2^+ , O_4^+ , $N_2\cdot O_2^+$, NO^+ , N_2O^+ , NO_2^+ , $N_2\cdot NO^+$, $O_2\cdot NO^+$, and $NO\cdot NO^+$. Excited states of nitrogen and oxygen molecules included are $N_2(v=1-40)$, $N_2(A^3\Sigma_u^+)$, $N_2(B^3\Pi_g)$, $N_2(W^3\Delta_u)$, $N_2(B^3\Sigma_u^-)$, $N_2(C^3\Pi_u)$, $N_2(E^3\Sigma_g^+)$, $N_2(a'^1\Sigma_u^-)$, $N_2(a'^1\Pi_g)$, $N_2(w^1\Delta_u)$, $N_2(a''^1\Sigma_g^+)$, $N(^4S)$, $N(^2D)$, $N(^2P)$, $O_2(^1\Delta_g)$, $O_2(^1\Sigma_g)$, O_2^{**} , $O(^3P)$, $O(^1D)$, and $O(^1S)$. Here O_2^{**} is a sum of Herzberg excited electronic states ($A^3\Sigma_u$, $C^3\Delta_u$, and $c^1\Sigma_u^-$) of O_2 molecule; $O(^3P)$, $O(^1D)$, $O(^1S)$ are the ground and electronically excited states of atomic oxygen; $N(^4S)$, $N(^2D)$, $N(^2P)$ are the ground and electronically excited states of atomic nitrogen. Neutral species incorporated are N , O , O_3 , NO , NO_3 , N_2O , N_2O_4 , N_2O_5 .

The governing equations used in the present model are listed below:

$$\frac{\partial n_\alpha}{\partial t} = -\partial \vec{J}_\alpha / \partial x + S_\alpha - L_\alpha \cdot n_\alpha \quad (\text{II.1})$$

$$\frac{\partial n_\beta}{\partial t} = -\partial \vec{J}_\beta / \partial x + S_\beta - L_\beta \cdot n_\beta \quad (\text{II.2})$$

$$\frac{\partial^2 \phi}{\partial x^2} = -\frac{1}{\epsilon_0} e \cdot \sum_\alpha n_\alpha \quad (\text{II.3})$$

$$\frac{\partial}{\partial t} \left(\frac{3}{2} n_e T_e \right) = \vec{j} \cdot \vec{E} - \frac{\partial}{\partial x} \left(-k_e \frac{\partial T_e}{\partial x} + \frac{5}{2} T_e \cdot n_e \cdot v_e \right) - n_e \sum \Delta \epsilon_i k_i n_i \quad (\text{II.4})$$

$$\frac{\partial}{\partial t} (\rho \epsilon) = -\frac{\partial Q_\lambda}{\partial x} - \frac{\partial}{\partial x} \left(\sum_{i=1}^k h_i J_i \right) + \vec{j} \cdot \vec{E} + W_\epsilon \quad (\text{II.5})$$

$$\begin{aligned} \frac{\partial n_v}{\partial t} = & n_e [N_2] k_v^+ - n_e [N_2] k_v^- + n_{v-1} [N_\beta] K_{v,v-1} + n_{v+1} [N_\beta] K_{v+1,v} - n_v (K_{v,v-1} + K_{v,v+1}) \\ & + n_{v-1} \sum_w n_{w+1} K_{v-1,v}^{w+1,w} + n_{v+1} \sum_w n_w K_{v+1,v}^{w,w+1} - n_v (\sum_w n_{w+1} K_{v,v+1}^{w+1,w} + \sum_w n_w K_{v,v-1}^{w,w+1}) + (Chem)_v - D_r \frac{n_\beta - n_\beta^\infty}{R^2} \end{aligned} \quad (\text{II.6})$$

Eqs. (II.1, II.2) are time-resolved conservation equations for number densities of charged species, n_α (in particular, n_e is the electron number density) and neutral species, n_β . $\vec{J}_\alpha = \pm \vec{v}_{dr}^\alpha \cdot n_\alpha - D_\alpha \cdot N_0 \cdot \frac{\partial}{\partial x} (n_\alpha / N_0)$ stand for electron and ions fluxes (+ and - signs are used for positively and negatively charged species, respectively), and

$\vec{J}_\beta = \vec{v} \cdot n_\beta - D_\beta \cdot N_0 \cdot \frac{\partial}{\partial x} \left(\frac{n_\beta}{N_0} \right) - D_r \frac{n_\beta - n_\beta^\infty}{R^2}$ denote neutral species fluxes. In the expressions for the fluxes, N_0 is the total number density, v_{dr}^α are the charged species drift velocities, v is the gas flow velocity, D_α and D_β are diffusion coefficients of the charged and the neutral particles, D_r is the diffusion coefficient for the neutral particles in the radial direction, and R is the filament radius. Initial electron and ion concentrations used (N_2^+ for nitrogen and $[N_2^+] = [O_2^+] = 0.5 \cdot [e]$ for air) are 10^4 cm^{-3} . Varying the initial electron concentration within a range of 10^3 - 10^6 cm^{-3} did not have a significant effect on breakdown moment or the predicted current waveform.

In Eqs. (II.3 – II.5), φ , ρ , e and T_e are the electric potential, density, elementary charge, and electron temperature, respectively; k_e , k_i , $\Delta\varepsilon_i$ are electron thermal conductivity, inelastic collisions rate coefficients, and electron energy losses in inelastic collision processes. In the energy equation (Eq. (5)),

Q_λ is the thermal conductivity term, Q_J is Joule heating term, $W_e = \mu \frac{7}{3} \left(\frac{\partial v}{\partial x} \right)^2$ is the viscous dissipation term, and h_i is the enthalpy of species i .

The system of equations listed above is solved self-consistently, using the same time scale for all equations. The boundary conditions for species number densities are as follows: the charged particles concentrations are zero ($n_\alpha=0$) at the electrodes and neutral particles fluxes to the electrodes surfaces ($j_\beta=0$) are zero. The secondary electron emission coefficient used is $\gamma=0.1$ [47], such that the electron and ion fluxes on the surface of the cathode are related as follows, $\vec{J}_e|_{cathode} = -\gamma \cdot \vec{J}_{ions}^+|_{cathode}$. Note that the value of secondary electron emission coefficient, within a range of $0.05 < \gamma < 0.2$, did not have a significant effect on the discharge current. The quenching coefficients for the excited species on the electrode surfaces are taken to be 10^{-3} for all excited states (both nitrogen and oxygen). Note that the effect of surface quenching of the excited species quenching during the $\sim 200 \text{ ns}$ long discharge pulse is negligible, since excited states do not come to the electrodes on this short time scale. Surface quenching of the excited states in the afterglow is also of minor importance since diffusion fluxes to the electrodes are very slow, compared to the gas flow in the radial direction. The boundary conditions for the energy equation (Eq. (II.5)) on the electrode surfaces assume constant temperature, $T_{electrodes}=300 \text{ K}$.

Vibrational level populations of nitrogen (n_v) are calculated using Eq. (II.6). Here, n_v are absolute populations of excited vibrational levels of N_2 , $v>0$. Eq. (II.6) includes N_2 vibrational excitation by electron impact, vibration-to-vibration (V-V) energy exchange, vibration-to-translation (V-T) energy relaxation, and chemical reactions of vibrational excited molecules. K_v^+ and K_v^- are rate coefficients for electron impact excitation and de-excitation of vibrational level v , $K_{v,v\pm l}$ are rate coefficients for V-T relaxation, N_β are number densities of “relaxer” species (N_2 , O_2 , N , and O), and $K_{v,v\pm l}^{w,w\pm l}$ are rate coefficients of V-V exchange (only N_2 - N_2 exchange was taken into account).

The present model includes 40 excited vibrational levels of nitrogen, of which the first 17 levels are assumed to be excited by electron impact. Cross sections for electron impact excitation of these levels are taken from Refs. [61,62]. Note that cross sections for electron impact excitation of high vibrational levels ($v>9$) decrease rapidly, such that peak value for electron impact excitation of $v=9$, $\sigma_{09}=6.1 \cdot 10^{-18} \text{ cm}^2$, is a factor of 4 lower than that of $v=8$, $\sigma_{08}=2.52 \cdot 10^{-17} \text{ cm}^2$. The rates for V-T relaxation of vibrationally excited states of nitrogen by N_2 , O_2 , N , and O used in the model were taken from Ref. [63], with $K_{1,0}$ taken from [64]. Expressions for N_2 - N_2 V-V exchange rates were taken from Ref. [63], with $K_{0,1}^{1,0}$ taken from Ref. [60], where it has been measured directly.

Terms $S_{\alpha,\beta}$ and $L_{\alpha,\beta} n_{\alpha,\beta}$ in Eqs. (II.1, II.2) represent rates of production and loss of ions and excited species (α and β , respectively) in chemical reactions, including electron impact and ion-molecule reactions. Rate coefficients of electron impact processes were determined using cross sections taken from

Refs. [61,65] and the electron energy distribution function (EEDF) calculated by solving the Boltzmann equation for the electrons in the two-term approximation by the method described in Ref. [66]. Rate coefficients of ion-molecule reactions and of chemical reactions among neutral species were taken from Refs. [67,68].

The Boltzmann equation for the isotropic part f_0 of the EEDF, used to calculate rate coefficients of electron impact processes, is listed below [66,69]:

$$\frac{\partial f_0}{\partial t} = \frac{e\vec{E}}{3m \cdot v^2} \frac{\partial}{\partial v} \left(\frac{v^3}{v} \vec{\nabla} f_0 + \frac{v^2 e \vec{E}}{m \cdot v} \frac{\partial f_0}{\partial v} \right) - Q_{inel} + \left(\frac{\delta f_0}{\delta t} \right)_{ee} \quad (\text{II.7})$$

Here, Q_{inel} is the collision integral for inelastic electron-neutral collisions and $\left(\frac{\delta f_0}{\delta t} \right)_{ee}$ is the electron-electron collision integral; m , v , e are electron mass, velocity, and charge, respectively; and v , E are the electron-neutral elastic collision frequency and the electric field. The Rosenbluth–Shkarowsky method [70] was used to take into account Coulomb collisions between electrons:

$$\left(\frac{\delta f_0}{\delta t} \right)_{ee} = \frac{Y}{v^2} \frac{\partial}{\partial v} \left[f_0 I_0^0 + \frac{mv^2}{3} (I_2^0 + J_{-1}^0) \frac{\partial f_0}{\partial \varepsilon} \right]. \quad (\text{II.8})$$

Here, $I_j^i = \frac{4\pi}{v^j} \int_0^\infty f_i v^{2+j} dv$, $J_j^i = \frac{4\pi}{v^j} \int_v^\infty f_i v^{2+j} dv$, $Y = \frac{4\pi e^2}{m_e^2} \ln \Lambda (CGS)$. Note that at electron densities of $n_e \sim 10^{13}\text{-}10^{14} \text{ cm}^{-3}$ and electron temperatures of $T_e \sim 2\text{-}3 \text{ eV}$, the estimated electron-electron collision frequency is $\sim 10^8\text{-}10^9 \text{ s}^{-1}$. Therefore the electron energy relaxation time in these collisions is of the order of $\sim 10 \text{ ns}$, i.e. shorter than the discharge pulse duration. This demonstrates the importance of taking into account electron-electron collisions at the conditions of the experiments [59].

Incorporating the electron-electron collision integral in Eq. (II.7) requires solving the Boltzmann equation self-consistently with the rest of governing equations. This results in considerable increase of computational time since the model becomes essentially two-dimensional, the first dimension being the axial coordinate (see Fig. II.1), and the second dimension the electron energy. If electron-electron collisions are neglected, the electron energy relaxation time is less than 1 ns and the following approach was used instead: first, electron swarm parameters and electron impact coefficients were calculated over a wide range of reduced electric field (E/N) values, and tabulated as functions of mean electron energy (electron temperature). After that, the EEDF was recalculated when the composition of the plasma (including number densities of excited species) had changed significantly, to account for the EEDF change due to superelastic collisions. Typically, the EEDF was recalculated approximately 5 times during the discharge pulse. Note that this approach (i.e. using electron impact coefficient as functions of electron temperature, calculated from Eq. (II.4)) allows taking into account nonlocal effects, such as electron thermal conductivity. The results of modeling calculations carried out with and without electron-electron collisions taken into account are compared in Section II.3 below.

II.3. Results and discussion

As discussed in Section II.2, nanosecond pulse discharge simulations were carried out for two gases, nitrogen and dry air. The model predictions are compared with the experimental data for discharge current, gas temperature, N₂ vibrational level populations, and absolute number densities of N, O and NO [59]. The modeling calculation results are discussed below.

II.3.1. Discharge pulse

Figure II.2 plots experimental voltage and current pulse waveforms, as well as the discharge current predicted by the kinetic model in nitrogen and air. As discussed in Section II.2, the experimental voltage pulse waveform is used as one of the input parameters of the model. Note that the present one-dimensional model predicts the current density rather than the total current, measured in the experiment. To predict the current, the current density was multiplied by the estimated cross sectional area of the discharge filament. The filament diameter was determined from broadband ICCD images of UV / visible discharge emission [59]. Fig. II.3 plots the radial distribution of emission intensity halfway between the electrodes, with the full width at half maximum (FWHM) of 2.1 mm. Thus, the current density predicted by the model was multiplied by the filament cross sectional area of $A=0.0346 \text{ cm}^2$ to compare it with the experimentally measured current. Comparison of the experimental and the predicted current traces in nitrogen (see Fig. II.2a) shows that the model somewhat overpredicts the current during breakdown (when the applied voltage falls rapidly) but is in good agreement with the rest of the experimental current pulse shape. The predicted current pulse shape in air (see Fig. II.2b) is also in fairly good agreement with the experimental current waveform, although the model somewhat overpredicts the current decay after breakdown. Note that the “bump” in the experimental current pulse shapes occurring during the initial voltage rise (before breakdown) is due to significant stray capacitance of the external circuit, which was not incorporated in the present model.

As discussed in Section II.2, initial electron concentration was assumed to be very low, 10^4 cm^{-3} . During the initial rise of the applied voltage (before breakdown), the electrons drift toward the anode. Breakdown occurs when the applied voltage reaches its maximum value of about 12 kV (at $t\approx0 \text{ ns}$, see Fig. II.2). During breakdown, the “forward” ionization wave initiated by volumetric electron impact ionization propagates from the anode to the cathode. The “reverse” ionization wave propagates back to the anode, after secondary electron emission from the cathode begins. These two stages occur very rapidly, over $\sim 10 \text{ ns}$, while the current increases sharply. This is consistent with the experimental observations of the forward and the reverse ionization waves in Ref. [61]. After breakdown, the voltage drops to approximately 2.5 kV, due to the presence of the current-limiting ballast resistor ($1 \text{ k}\Omega$) in the external circuit. Since the external circuit is not incorporated in the model, the experimental voltage trace measured between the electrodes is used as one of the entry parameters of the model. A quasi-DC discharge phase follows the breakdown phase. During the quasi-DC phase, the applied voltage remains nearly constant, $\sim 2.5\text{-}3.0 \text{ kV}$, and the change in the discharge current is not very significant (see Fig. II.2).

Note that reproducing the shape of the time-dependent discharge current pulse is even more important than matching the absolute value of the current. For this, the model must correctly predict axial distributions of electric field and electron density in the plasma, as well as the rates of ionization processes in the discharge. The results of Fig. II.2 suggest that the present model predicts these parameters adequately, which justifies the use of one-dimensional approach at the present experimental conditions. The results also suggest that the model accurately predicts rates of generation of excited states and radicals by electron impact.

Figure II.4 plots some of the predicted discharge parameters in nitrogen, including voltage fall across the cathode layer (Fig. II.4a), and reduced electric field and electron density in the middle of the discharge gap (i.e. halfway between the electrodes, Fig. II.4b). From Fig. II.4a, one can see that after breakdown, the cathode voltage fall, approximately 1.5 kV, is quite high is comparable with the applied voltage, approximately 2.5 kV, thus limiting the field in the plasma.

The reduced electric field first increases up to about $E/N=350 \text{ Td}$ ($1 \text{ Td} = 10^{17} \text{ V}\cdot\text{cm}^2$) after the voltage is applied, and then decreases sharply after breakdown, due to the voltage drop on the ballast resistor in the external circuit. After breakdown, the reduced electric field in the plasma (outside of the cathode layer) remains fairly low, $E/N=50\text{-}100 \text{ Td}$ (see Fig. II.4b). The electron number density reaches its maximum value of about $n_e=3\cdot 10^{14} \text{ cm}^{-3}$ during breakdown, after which it decreases gradually, due to recombination

processes dominating over ionization. Thus, after breakdown the electric field in the plasma is relatively low and the electron concentration is quite high.

Note that it is possible that a significant cathode voltage fall predicted by the present one-dimensional model may be somewhat overpredicted because the model underpredicts the area occupied by the discharge on the surface of the cathode (“cathode spot”). After the reverse ionization wave reaches the anode, the current channel near the cathode spreads out, such that the cathode spot may occupy significantly greater surface area than the filament cross section, which is not accounted for in the present model. Indeed, NO PLIF images taken in the experiment [59] demonstrate that the cathode spot area is significantly larger compared to the cross section of the discharge filament. Thus, the cathode fall value predicted by the present model represents an upper bound value. However, the current density distribution across the cathode spot is not necessarily uniform, such that the cathode voltage fall evaluated based on this assumption would be a lower bound estimate. A more accurate prediction of the cathode fall would require using a two-dimensional model of the discharge. However, comparison of the present model predictions with the experimental data, including current waveforms, N, NO, and O number densities, and N₂ vibrational level populations suggests that the model provides an adequate description of the discharge kinetics and plasma chemistry.

II.3.2. Effect of electron-electron collisions

The results of modeling calculations predict that the electron concentration during the discharge pulse at the present conditions exceeds 10¹⁴ cm⁻³ (peak electron densities in nitrogen and air are n_e=2.5·10¹⁴ cm⁻³ and n_e=1.4·10¹⁴ cm⁻³, respectively, with peak ionization fraction of n_e/N~10⁻⁴). It has been shown previously [66,72] that electron-electron collisions become important above ionization fraction of n_e/N~10⁻⁶ (in noble gases) and above n_e/N~10⁻⁵-10⁻⁴ (in molecular gases), such that incorporating them into the present model (see Section II.2) is necessary.

Most of the ionization during the discharge pulse occurs during the first few tens of nanoseconds, in two stages. First, a “forward” ionization wave propagates from the anode to the cathode, increasing the electron number density in the plasma up to n_e~10¹²-10¹³ cm⁻³. After the wave front reaches the cathode, secondary electron emission from the cathode is triggered by the ions generated in the ionization wave front. This results in a “reverse” ionization wave, propagating from the cathode to the anode and increasing the electron number density up to n_e~10¹⁴ cm⁻³. The electric field ahead of the forward ionization wave is very high because charge separation in the wave front shields the plasma behind the wave. This leads to a dramatic increase of the voltage fall across the cathode layer, up to 4.5 kV (see Fig. II.4). The electric field ahead of the reverse ionization wave is also high since the sudden increase in the secondary emission from the cathode results in a significant reduction of the cathode voltage fall and increases the electric field in the rest of the discharge gap. This makes the effect of electron-electron collisions on the rate of ionization during this stage insignificant, since this effect is reduced as the electric field is increased [66].

After breakdown, the electron concentration in the plasma is fairly high while the electric field in the plasma becomes rather low, due to a significant voltage drop across the cathode layer. Note that most of the energy is coupled to the plasma after breakdown, during the quasi-DC discharge phase (see Fig. II.2), resulting in significant vibrational excitation, as well as some electronic excitation and dissociation. To illustrate the effect of electron-electron collisions on the coupled energy partitioning among different excited states, modelling calculations were carried out with electron-electron collisions turned on and off, with the results discussed below. First, Fig. II.5 plots EEDFs predicted in a nitrogen plasma at E/N=100 Td and n_e=2·10¹⁴ cm⁻³, with and without electron-electron collisions taken into account. As is well known, the EEDF has a well-pronounced, nearly “step-wise” drop at electron energy of ε~2 eV, produced by significant electron energy loss in inelastic collisions (primarily N₂ vibrational excitation by electron impact). Also, as expected, the EEDF with electron-electron collisions taken into account exhibits a more

gradual reduction with the electron energy (see Fig. II.5). This occurs since Coulomb collisions result in “maxwellization” of the distribution function [47], i.e. bring it closer to a straight line in a semilog plot in Fig. II.5 and raise the higher energy “tail”.

Note that electron-electron collisions conserve the electron energy, simply redistributing it between the collision partners, such that some of the electron impact rate coefficients may increase while others may be reduced. Figure II.6 compares N₂ vibrational level populations during the discharge pulse predicted by the model with and without electron-electron collisions taken into account, illustrating a significant difference between these two cases. In particular, incorporating electron-electron collision results in higher v=1,2 level populations but lower v=3,4 level populations. Comparison with the experimental data points, also shown in Fig. II.6, shows that including electron-electron collisions results in a much better agreement with the experiment, and demonstrates that electron impact vibrational excitation and de-excitation processes of N₂ are represented by the model adequately. Note the electron-electron collisions have almost no effect on the dissociation process since it takes place mostly in the beginning of the discharge pulse, when electric field in the discharge gap is still very high. At higher electric fields, the effect of electron-electron collisions becomes weaker.

II.3.3. Excitation and decay of N₂ vibrational levels

As discussed in Section II.2, the present model incorporates 40 vibrational levels of the ground electronic state of N₂, with vibrational levels v=1-17 excited by electron impact during the discharge pulse. The simulation results are compared with psec CARS measurements in nitrogen and air [20], where the first five vibrational levels, v=0-4, were detected. Time-resolved N₂(v=0-4) vibrational level populations predicted by the model in nitrogen are compared with the experimental results in Fig. II.7(a)). It can be seen that the model predictions are in very good agreement with the experimental data, over a wide range of time scales, from $\sim 10^{-7}$ until $\sim 10^{-2}$ s. Note that vibrational level population reduction beyond $\sim 10^{-3}$ s is not produced by V-V exchange or by V-T relaxation, both of which are significantly slower, and is most likely due to diffusion in the radial direction. In the present work, the characteristic diffusion time is estimated to be $\tau_{\text{diff}} \approx (d/2)^2/D \approx 8$ ms, much shorter compared to the convection time, $\tau_{\text{conv}} \approx d/u \approx 40$ ms, where the flow velocity, estimated from the flow rate, is $u \approx 5$ cm/s. This estimate for the diffusion time is shorter compared to the diffusion time estimated from NO number density measurements in later afterglow in Ref. [59], $\tau_{\text{diff}} \approx 20$ ms, which is most likely due to the size of CARS signal collection region being significantly smaller compared to LIF and TALIF diagnostics (see the discussion in Ref. [59]).

From Fig. II.7(a), it can be seen that time-resolved populations of excited vibrational levels of N₂ exhibit several different trends. Specifically, the N₂(v=1) population increases after the discharge pulse (on the time scale of $\sim 10^{-7} - 10^{-4}$ s), before decaying on the long time scale, $\sim 10^{-3} - 10^{-2}$ s. On the other hand, N₂(v=3,4) populations start decreasing soon after the voltage is turned off. Comparison with the modelling calculations shows that, as expected, this behaviour is controlled by the “downward” V-V exchange, N₂(v=0) + N₂(w) \rightarrow N₂(v=1) + N₂(w-1), due to overpopulation of high vibrational levels, N₂(w>2), during the discharge pulse. This results in net vibrational energy transfer to the low levels in the afterglow, transient overpopulation of N₂(v=1), and increase of the “first level” N₂ vibrational

temperature, $T_v = \frac{\theta_{10}}{\ln(n_0/n_1)}$, where $\theta_{10}=3353$ K is the energy spacing between vibrational levels v=1 and v=0. Note that dynamics of N₂(v=0-4) vibrational level populations in nitrogen is not affected by V-T relaxation processes since their rates are very low.

Time evolution of N₂(v=0-4) vibrational level populations in air are shown in Fig. II.7(b). In this case, the agreement with the experimental data points is not as good as in nitrogen; however, it can be seen that the overall trend of transient overpopulation of v=1 and gradual decay of higher level

populations is still reproduced rather well. The model reproduces the rise of the first excited vibration level population ($v=1$) within $\sim 10^{-4}$ s, although it somewhat underpredicts its peak absolute value. The prediction for $N_2(v=2)$ population, which remains nearly unchanged until $\sim 10^{-3}$ s in the experiment, is not as good, with the model predicting its gradual decay after $\sim 10^{-5}$ s.

The experimental and predicted “first level” N_2 vibrational temperature, translational/rotational temperature, and the apparent number of vibration quanta per N_2 molecule, $Q = \sum_{v=1}^4 v n_v / n_{N_2}$, in nitrogen

and air are shown in Fig. II.8(a,b). It can be seen that the model prediction for peak vibrational temperature in nitrogen is in good agreement with the experiment and is somewhat lower compared with the experimental value in air. Note that the experimentally measured number of vibrational quanta per N_2 molecule appears to increase after the pulse, both in nitrogen and air, until $\sim 10^{-4}$ s. In fact, the increase of Q after the pulse in nitrogen, predicted by the model (see Fig. II.8(a)), is due to the effect of downward V-V energy transfer from higher vibrational level, $v>4$, not measured in the experiments and therefore not included in the sum. The total number of quanta per molecule after the pulse, predicted by the model, remains nearly constant, since N_2 - N_2 V-V exchange conserves the number of vibrational quanta, until $\sim 10^{-3}$ s, when removal of vibrationally excited molecules by diffusion becomes significant. Finally, at the present low-temperature conditions (peak translational/rotational temperature of $T\sim 360$ K), the effect of V-T relaxation on N_2 vibrational mode energy on the number of quanta per molecule is negligibly small.

II.3.4. Production and decay of electronically excited species and radicals in the afterglow

Simulations of the experimental conditions were carried out for the time interval of 10 ms, starting approximately 50 ns before the applied pulse voltage rise from near zero (see Fig. II.4). This time interval includes (a) breakdown stage, including onset of electron impact ionization in the discharge gap, ionization wave propagation toward the cathode, and onset of secondary electron emission from the cathode; (b) quasi-steady-state discharge state reached after the breakdown, with a “plateau” reached in the applied voltage; and (c) afterglow stage, after the applied voltage is turned off. The model predictions for time-dependent species number densities, specifically atomic oxygen and nitrogen, as well as NO, were compared with the experimental results [59]. Comparison with time-resolved, absolute species concentration measurements in the afterglow puts the plasma chemistry mechanism used in the present model to a stringent test. Figure II.9 compares experimental O, N, and NO number densities in the afterglow [59] with the predictions of the “baseline” model described in Section II.2. Figure II.9 also plots the predicted gas temperature.

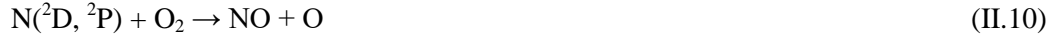
As can be seen from the experimental data points plotted in Fig. II.9, atomic nitrogen, which is mainly produced by electron impact during the discharge pulse, is decaying in the afterglow, starting at 5 μ s after the discharge pulse (the shortest delay time after the pulsed measured in the experiments [59]). The concentration of atomic oxygen, which is also generated during the discharge pulse, keeps increasing in the afterglow, most likely due to quenching of excited nitrogen molecules quenching in the following reactions:



The rate coefficients for this reaction are $2.54 \cdot 10^{-12}$ cm³/s for $N_2(A^3\Sigma_u^+)$ state and $3 \cdot 10^{-10}$ cm³/s (gas kinetic) for $N_2(B^3\Pi_g)$ and $N_2(C^3\Pi_u)$ states. The characteristic time for O_2 dissociation during reactive quenching of $N_2(A^3\Sigma_u^+)$ is 0.5 μ s.

Finally, experimental results show that NO number density is highest, approximately $2 \cdot 10^{15}$ cm⁻³, 5 μ s after the discharge pulse (first experimental point taken), and decreases after that. Since noticeable NO concentration reduction occurs over ~ 100 μ s (see Fig. II.9), it cannot be caused by diffusion or convection (gas flow), both of which are insignificant on this time scale. Also note that initial NO

concentration is almost two times higher than N atoms concentration (see Fig. II.9). Thus, rapid reactions of excited metastable states of nitrogen atoms, $N(^2D)$ or $N(^2P)$,



usually assumed to control NO formation in air afterglow [73-77], are unlikely to be the main mechanism of NO generation at the present conditions, since their number densities are even lower than that of the ground state nitrogen atoms.

Since the gas temperature in the presen experiments remains relatively low, below $T=400$ K (see Figs. II.8, II.9), reactions of Zel'dovich thermal mechanism of NO formation



do not affect nitric oxide generation in the discharge afterglow. Similarly, vibrational excitation of nitrogen at the present conditions is quite low (see Figs. II.7, II.8), such that it is unlikely to affect NO generation in a vibrationally enhanced first Zel'dovich reaction,



as has been suggested previously [79,79]. Indeed, based on the trend given by the experimental measuresnts of N_2 vibrational level populations in the ground electronic state (see Fig. II.7), estimated relative population of $v \sim 12$, which corresponds to the activation energy barrier of reaction (13), $E_a \sim 38,000$ K, is only $f_{12} \sim 10^{-5}$ (absolute population of $\sim 10^{13} \text{ cm}^{-3}$), which is about 2 orders of magnitude less than NO number density measured in the experiment.

This leaves quenching of electronically excited nitrogen,



where N_2^* is used as a generic symbol for N_2 excited electronic states, as the most likely primary mechanism of NO formation in the afterglow. Reaction (14) involving a metastable excited state $N_2(A^3\Sigma_u^+)$, with the rate coefficient of $7 \cdot 10^{-12} \text{ cm}^3/\text{s}$ [63], is routinely incorporated in plasma chemistry kinetic models as one of key reactions for NO formation in nonequilibrium air plasmas [74,76]. Indeed, significant NO yield in reaction (14) is expected due to high atomic oxygen number density measured at the present conditions (up to $\sim 10^{16} \text{ cm}^{-3}$, see Fig. II.9). Although the baseline kinetic model used in the present work (see Section II.2) does incorporate reactive quenching processes of reaction (14), only three excited triplet states, $N_2(A^3\Sigma_u^+)$, $N_2(B^3\Pi_g)$, $N_2(C^3\Pi_u)$, have been considered as a reaction (14) channel. However, Fig. II.9 shows clearly that the baseline model strongly underpredicts peak NO number density (by about a factor of 5, $4 \cdot 10^{14} \text{ cm}^{-3}$ vs. $2 \cdot 10^{15} \text{ cm}^{-3}$) and overpredicts NO decay rate by about 2 orders of magnitude (primarily in the reverse 2nd Zel'dovich reaction, reaction of Eq. 12)). Also, the rate of N atom decay is strongly underpredicted. This behaviour suggests that quenching of other electronic states of N_2 contributes to NO production rate in the afterglow.

To test this hypothesis, the kinetic model has been expanded to incorporate other excited electronic states of nitrogen, specifically the triplet states $N_2(W^3\Delta_u)$, $N_2(B^3\Sigma_u^-)$, $N_2(E^3\Sigma_g^+)$ and the singlet states $N_2(a'^1\Sigma_u^-)$, $N_2(a'^1\Pi_g)$, $N_2(w^1\Delta_u)$, $N_2(a''^1\Sigma_g^+)$, as additional channels of reactive quenching (14). Although these states have allowed, rapid radiative transitions to lower energy excited electronic states or to the ground state (singlet states), collisional quenching is quite critical at the relatively high pressures involved (100 torr). Since non-reactive collisional quenching of these states, such as



is already included into the baseline model, expanding the model allows for quenching processes with $M=O$ to be reactive. Note that measurements of electronic state specific rates of reaction (14) are not available, due to scarcity of time-resolved NO measurements at strongly transient conditions, rather than

in steady state discharges or late afterglow. In the present work, the rate coefficient of reaction (14) for $N_2(A^3\Sigma_u^+)$ is $7 \cdot 10^{-12} \text{ cm}^3/\text{s}$ [63], and rate coefficients for all other excited states are assumed to be gas kinetic, $3 \cdot 10^{-10} \text{ cm}^3/\text{s}$. A similar approach was used for reactive quenching of excited electronic states N_2^* by O_2 (reaction (9), other than $N_2(A^3\Sigma_u^+)$), for which the rate coefficients were assumed to be the same as for $N_2(B^3\Pi_g)$ and $N_2(X^3\Pi_u)$, $3 \cdot 10^{-10} \text{ cm}^3/\text{s}$.

Time evolutions of N, O, and NO number densities, predicted by the expanded model, are presented in Figure II.10. Note that expanding the model significantly increases the amount of NO generated during the discharge pulse, although most of it is still produced in the afterglow, up to $\sim 1 \mu\text{s}$ after the pulse. It can be seen that the extended model reproduces the experimental data quite well. Specifically, the model accurately predicts peak NO number density, as well as [N] and [NO] reduction in the reverse 1st Zel'dovich reaction,



Note that the measured and the predicted reduction in NO number density up to $\sim 10^{-3} \text{ s}$ after the discharge pulse, $\Delta[NO] \sim 10^{15} \text{ cm}^{-3}$, is close to the peak measured N atom number density (see Fig. II.10). This demonstrates that at the present conditions, reaction (16) is the dominant channel of NO and N atom decay in the afterglow, on the time scale $\sim 10^{-5}$ - 10^{-3} s . Although the second Zel'dovich reaction ($NO + O \rightarrow N + O_2$) also affects NO formation and decay in the afterglow, it is important only when NO number density is low, below $\sim 10^{13} \text{ cm}^{-3}$. Finally, NO decay on the long time scale, $\sim 10^{-3}$ - 10^{-1} s (see Fig. II.10), is primarily due to diffusion rather than its conversion to higher nitric oxides, such as NO_2 and N_2O . To illustrate that, Fig. II.11 plots time-resolved number densities of NO_2 and N_2O , predicted by the kinetic model, which includes chemical reactions among NO_2 , NO_3 , N_2O , N_2O_4 , and N_2O_5 . N_2O is primarily produced during reactive quenching of N_2^* by oxygen molecules,



(rate coefficient $8.7 \cdot 10^{-16} \text{ cm}^3/\text{s}$ [63]) on the time scale ~ 1 - $10 \mu\text{s}$, and remains nearly constant after this. NO_2 generation and decay is primarily controlled by the following reactions,



on the time scale ~ 1 - $10 \mu\text{s}$, and



on the time scale ~ 0 - $100 \mu\text{s}$ (see Fig. II.11).

II.4. Conclusions

The modelling calculations results discussed in the present paper provide key new insight into the kinetics of vibrational excitation of nitrogen and plasma chemical reactions in a nanosecond pulse, “diffuse filament” discharges in nitrogen and dry air at a moderate energy loading per molecule, $\sim 0.1 \text{ eV/molecule}$, studied in our recent work [59]. The present results demonstrate that ionization fraction achieved in the discharge filament, $n_e/N \sim 10^{-4}$, is sufficiently high for electron-electron collisions to affect the electron energy distribution function, the rates of electron impact processes, and the electron energy partitioning among different molecular energy modes. Specifically, taking electron-electron collisions into account produces much better agreement with the measured $N_2(X^1\Sigma, v=0-4)$ vibrational level populations at the end of the discharge pulse. Also, the results illustrate that self-consistent modelling of the cathode layer development in high peak current, nanosecond pulse duration discharges is critical for predicting the electric field in the plasma after breakdown, since at these conditions the cathode voltage fall may be comparable to the voltage between the electrodes after breakdown.

The present modelling calculations demonstrate that the apparent transient rise of N_2 “first level” vibrational temperature after the discharge pulse, detected in the experiment [59], is due to net downward

V-V energy transfer in N₂-N₂ collisions, which increases N₂(X¹ Σ , v=1) population. Finally, comparison of the present results with the experimental data shows that NO formation in the afterglow occurs during reactive quenching of multiple excited electronic levels of nitrogen molecule, N₂^{*}, by O atoms. Specifically, taking into account NO formation in reactive quenching of only the lowest metastable triplet level N₂(A³ Σ_u^+) results in a much lower predicted NO number density compared to the experimental results [59]. Incorporating NO formation during quenching of both singlet and triplet electronic states of N₂ resolves this issue, resulting in a much better agreement with the data. According to the expanded model predictions, nitric oxide is formed on the time scale of ~0.1-1 μ s after the discharge pulse, reaching its maximum value at ~1 μ s. After this, NO is predicted to decay mainly in a reaction with N atoms, NO + N \rightarrow N₂ + O, in good agreement with the experiment. Both measured and predicted reduction in NO number density in the afterglow is close to peak N atom number density, demonstrating that this reaction is the dominant channel of NO and N atom decay in the afterglow.

The present work demonstrates critical importance of time-resolved, absolute, multiple species concentrations measurements in highly transient plasmas, for quantitative insight into kinetics of plasma chemical reactions and confidence in the kinetic model predictions. Most N, O, and NO measurements available in the literature [73-76] have been done in steady-state discharges or in late afterglow, i.e. on time scales much longer than characteristic time for reactions of electronically excited species and radicals produced in the discharge (e.g. see [80]). This may result in a significant uncertainty in identification of plasma chemical processes controlling formation and decay of these species in the discharge and in the afterglow. Measurements of these radical species concentrations at shorter delay times after the discharge pulse, and/or at lower energy loadings per molecule would provide better time resolution of both their rise and decay. These data would help isolate kinetic processes involved and provide additional confidence in model predictions.

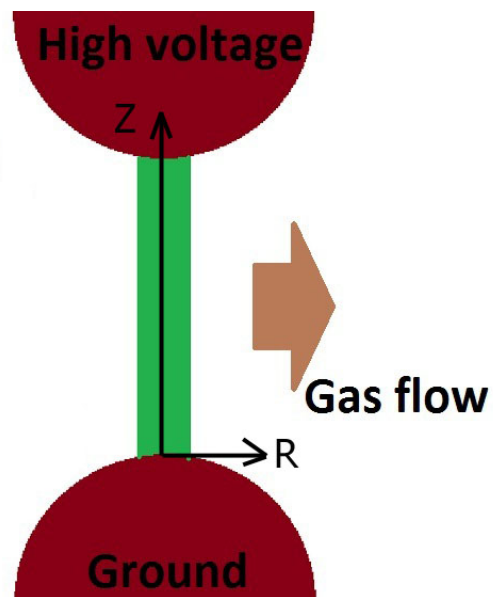


Figure II.1. Schematic of the discharge filament modeled in the present work.

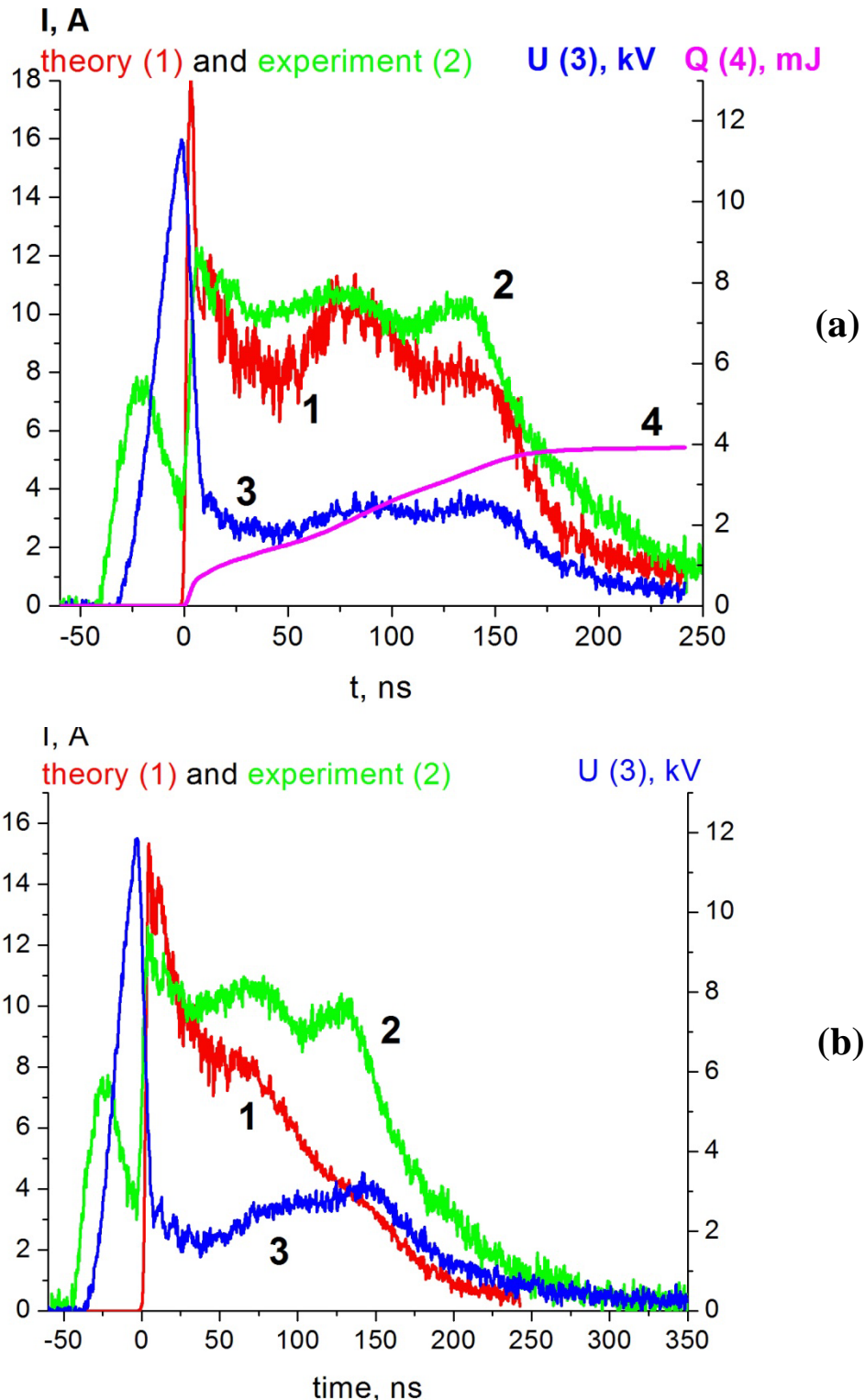


Figure II.2. Applied voltage pulse (experimental), discharge current pulse (experimental and predicted), and pulse input energy (predicted) in nitrogen (a) and in air (b).

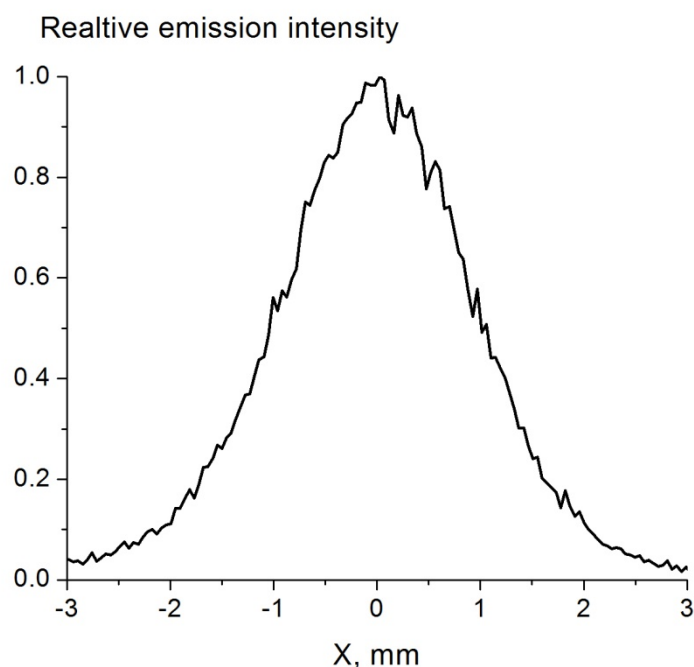


Figure II.3. Radial distribution of broadband emission intensity in the discharge filament in nitrogen.

Cathode fall (1) and applied voltage (2), kV

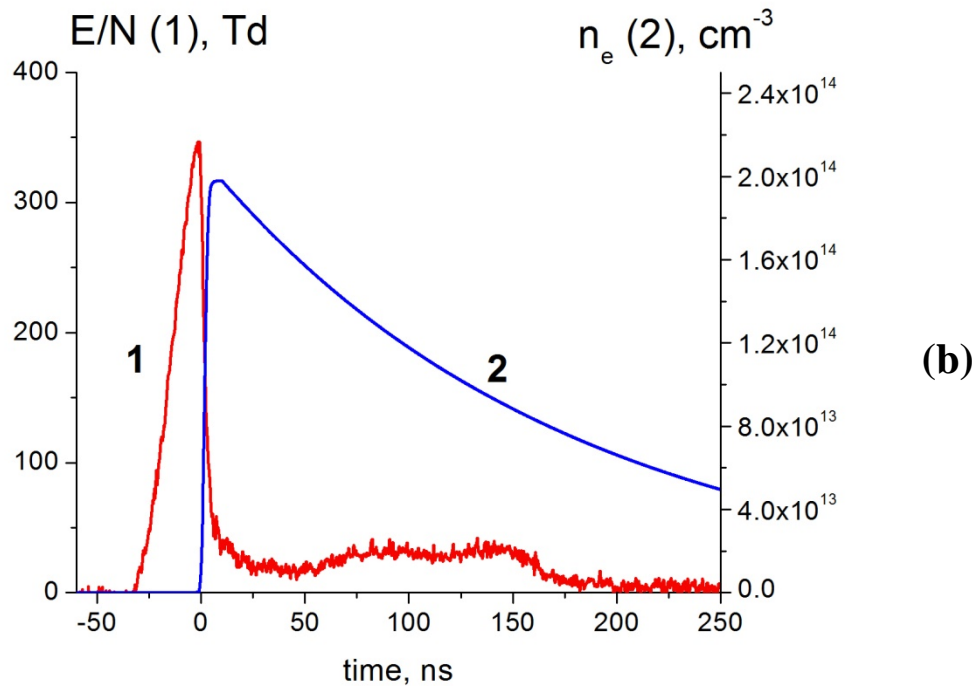
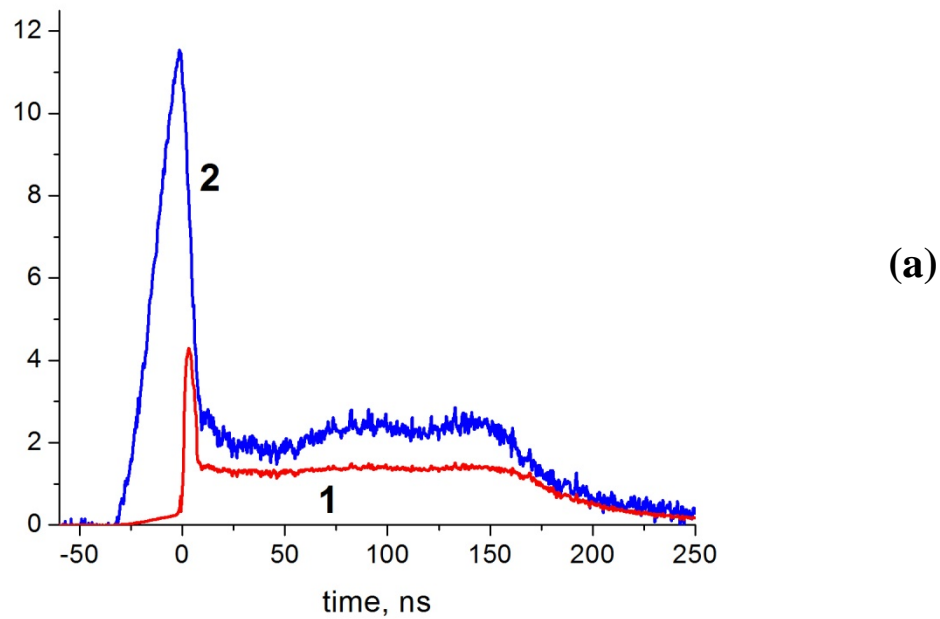


Figure II.4. (a) Experimental applied voltage and predicted voltage drop across the cathode layer in nitrogen; (b) Predicted reduced electric field and electron concentration in the plasma (halfway between the electrodes).

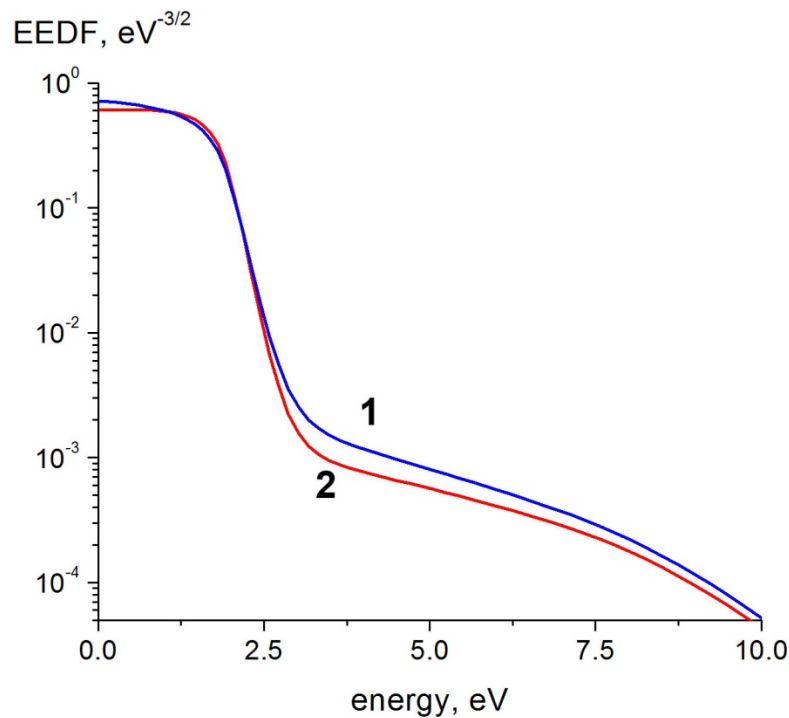


Figure II.5. Electron energy distribution functions (EEDF) in nitrogen, calculated with (1) and without (2) electron-electron collisions taken into account. $E/N=50 \text{ Td}$, $n_e=10^{14} \text{ cm}^{-3}$.

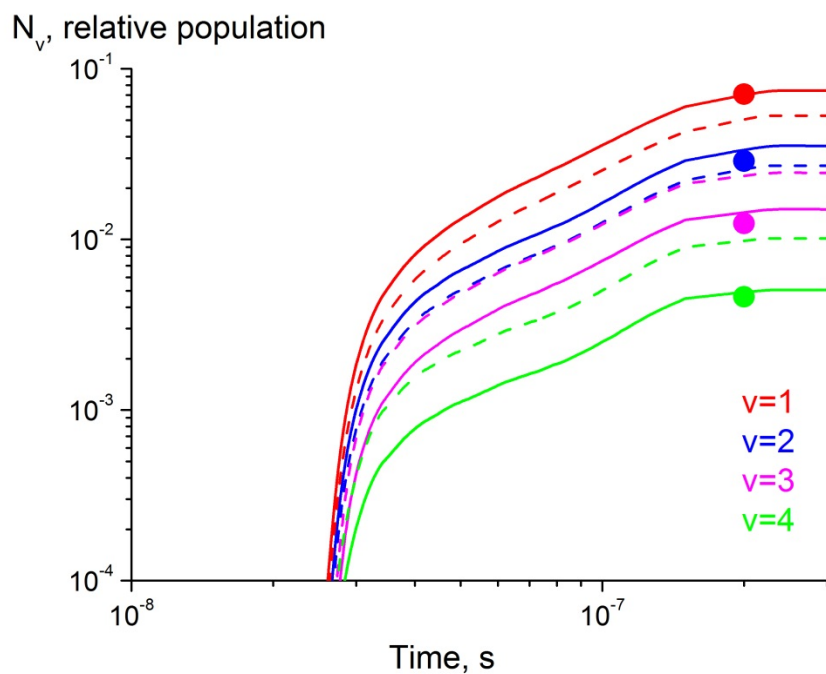


Figure II.6. N_2 vibrational level populations during the discharge pulse, calculated with electron-electron collisions (solid curves) and without electron-electron collisions (dashed curves) taken into account. Symbols show experimental measurements at the end of the discharge pulse.

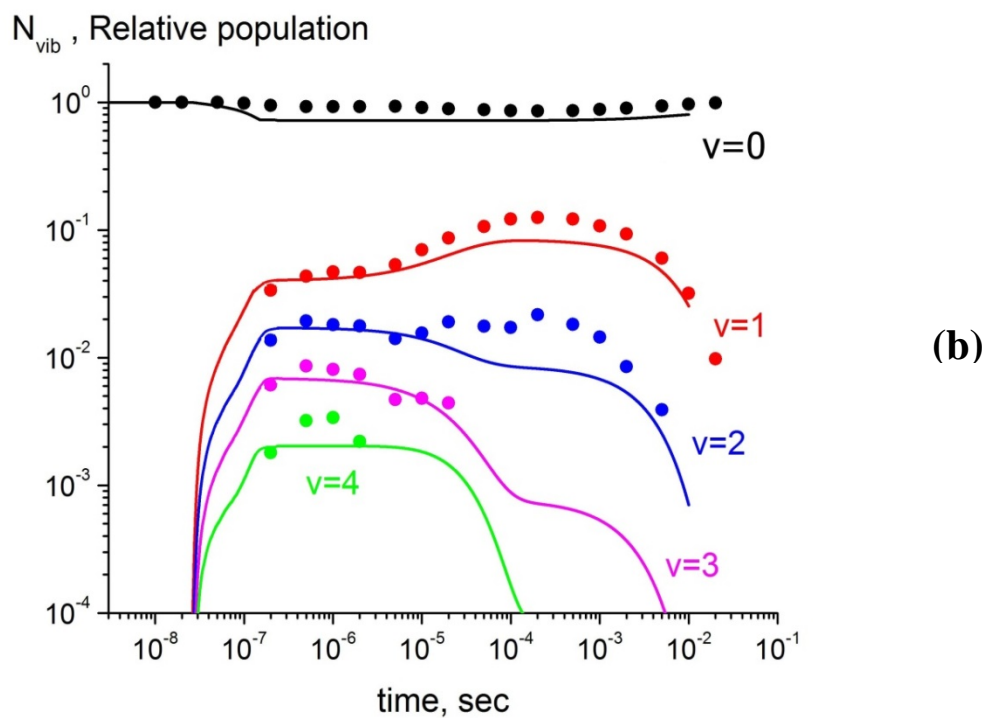
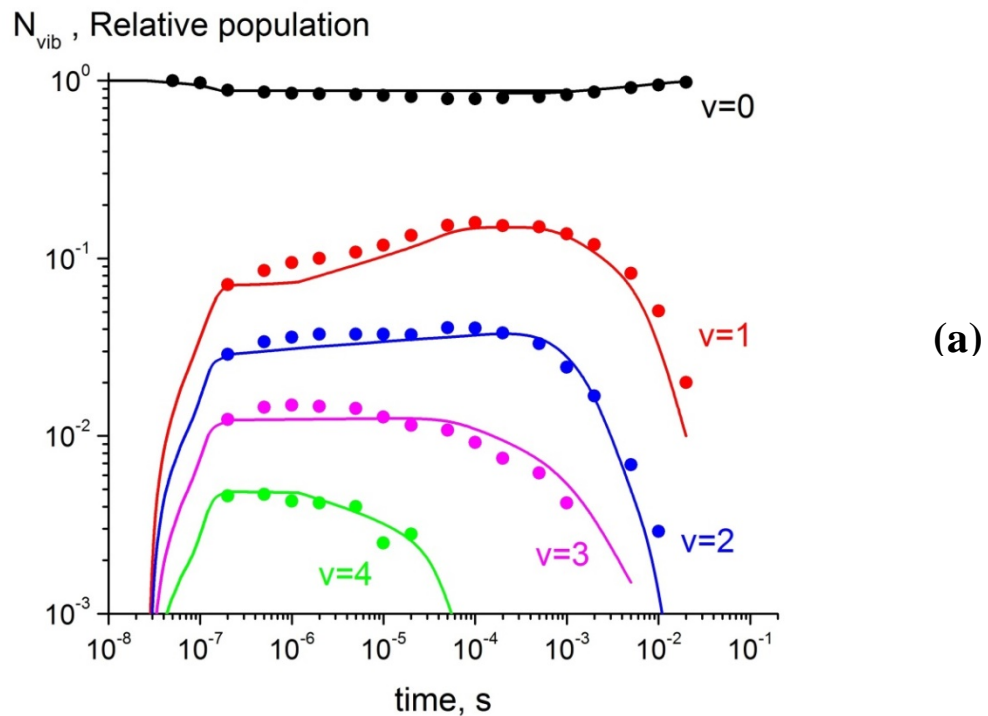


Figure II.7. Experimental (symbols) and predicted (curves) N_2 vibrational level populations during the discharge pulse and in the afterglow in nitrogen (a) and in air (b).

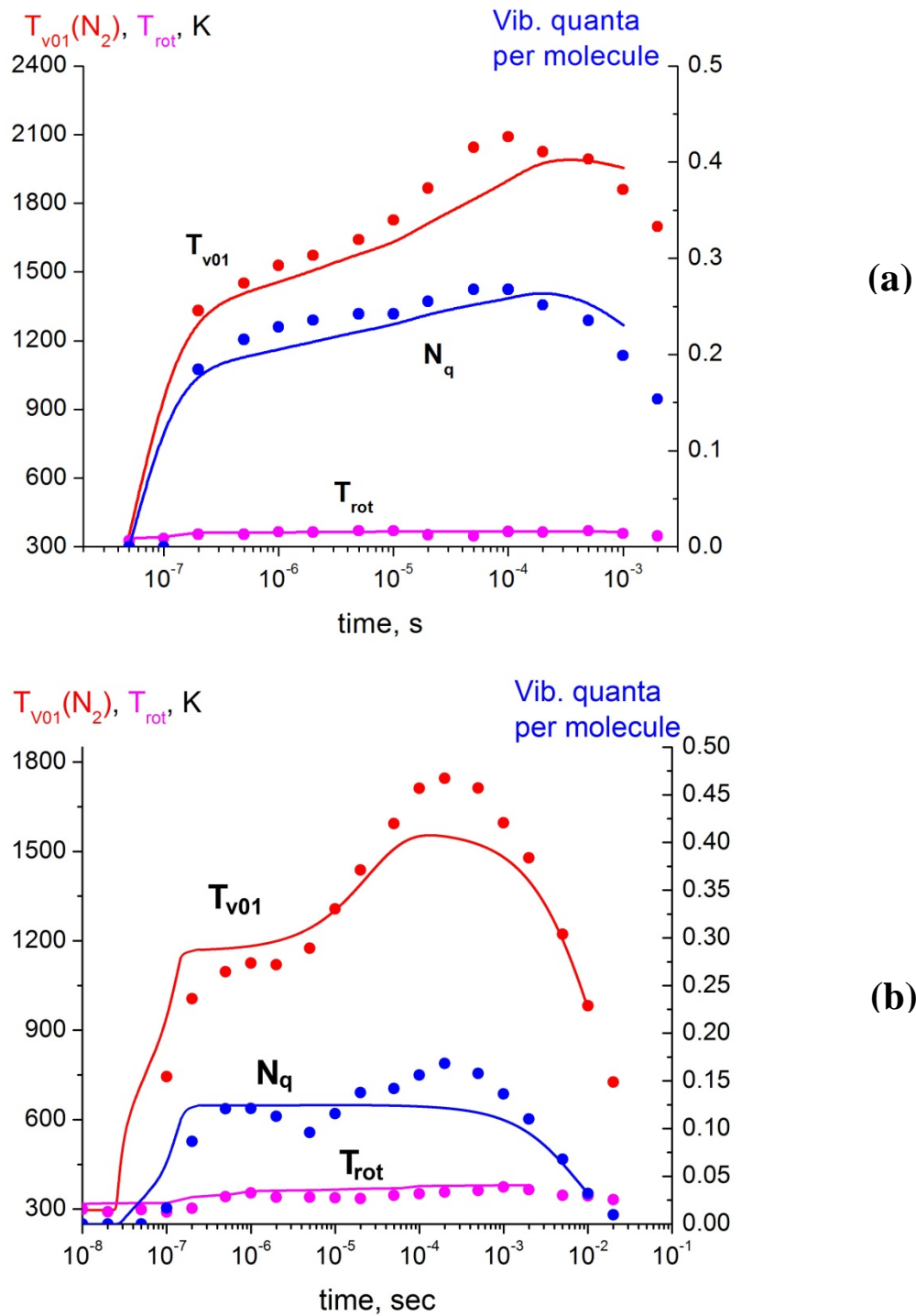


Figure II.8. Experimental (symbols) and predicted (curves) rotational-translational temperature, “first level” N_2 vibrational temperature, and number of vibration quanta per N_2 molecule in nitrogen (a) and in air (b).

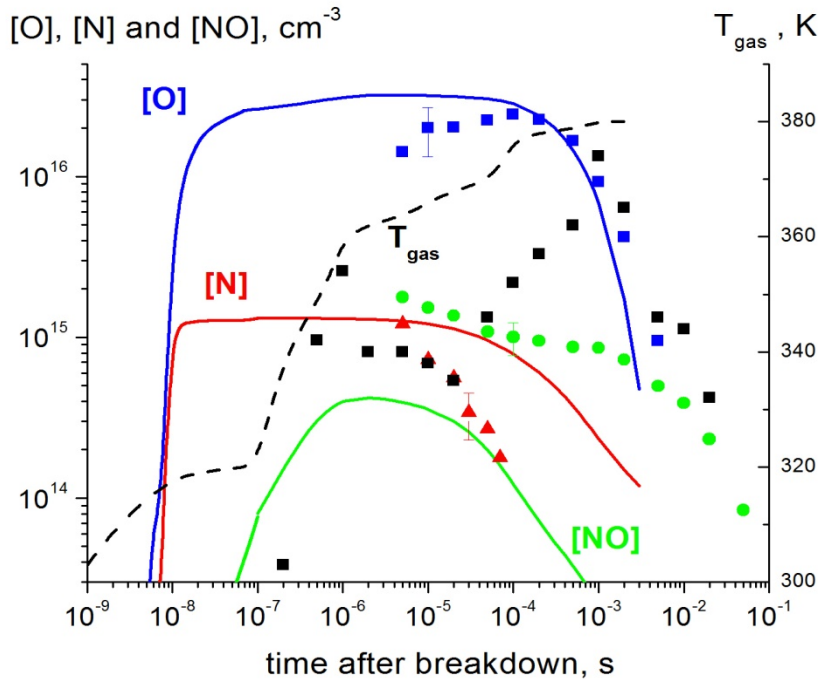


Figure II.9. Experimental (symbols) and predicted (curves) N, O, and NO number densities, and gas temperature in air, with reactive quenching of only $\text{N}_2(\text{A}^3\Sigma_u^+)$, $\text{N}_2(\text{B}^3\Pi_g)$, and $\text{N}_2(\text{C}^3\Pi_u)$ states contributing to NO formation.

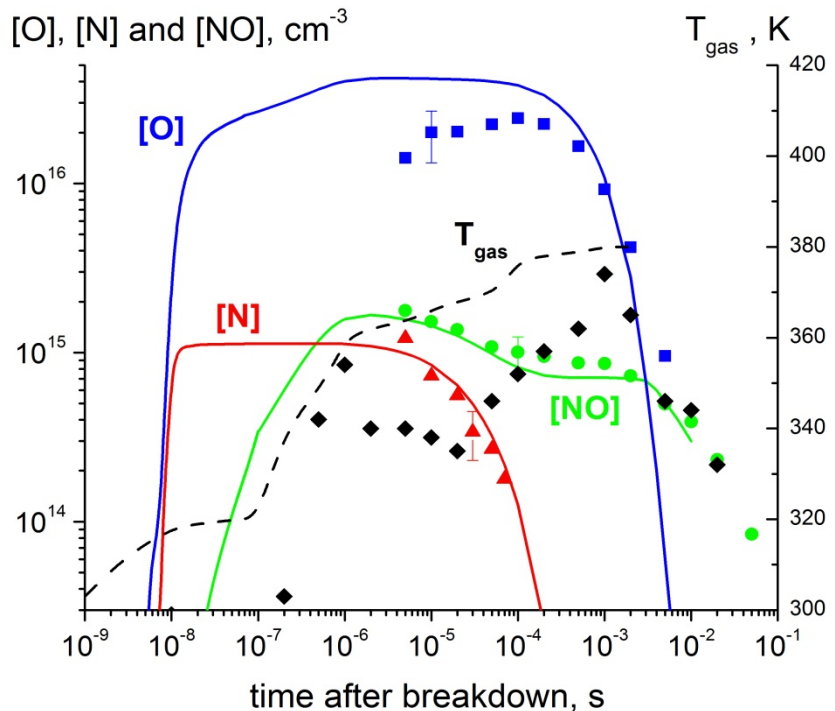


Figure II.10. Experimental (symbols) and predicted (curves) N, O, and NO number densities, and gas temperature in air, with reactive quenching of multiple N_2 excited electronic states contributing to NO formation.

$[N_2O]$ and $[NO_2]$, relative population

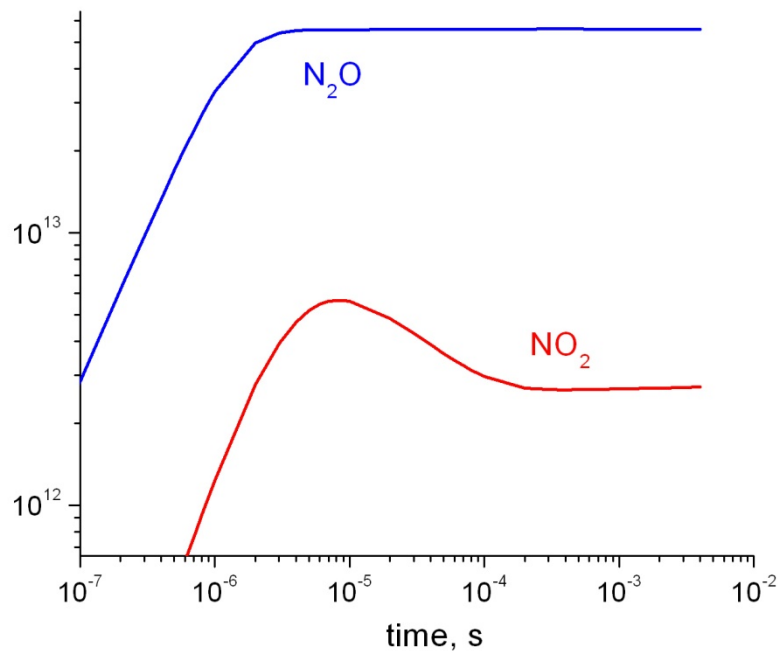


Figure II.11. Predicted N_2O and NO_2 number densities in the afterglow at the conditions of Fig. II.10.

III. Two-Stage Energy Thermalization Mechanism in Nanosecond Pulse Discharges in Air and Hydrogen-Air Mixtures

III.1. Introduction

Kinetics of energy transfer and thermalization in nonequilibrium electric discharges and afterglow in molecular gases is of considerable interest from a fundamental viewpoint and for applications such as plasma assisted combustion and plasma flow control [81-89]. In pulsed electric discharges used for plasma assisted combustion applications, temporal dynamics of gas temperature controls the rates of reactions among plasma-generated radicals, due to their strong dependence on temperature, and may critically influence fuel oxidation, ignition, and flameholding. In electric discharge plasmas used for high-speed flow control (“plasma actuators”), the rate of temperature rise strongly affects the amplitude of pressure perturbations and compression wave formation, which contribute to flow forcing.

It is well known that in nonequilibrium molecular plasmas only a small fraction of energy coupled by the electric field to electrons goes directly to gas heating, since electron-neutral collisions are extremely inefficient for elastic and rotational energy transfer [90]. Energy coupling to ions, with subsequent efficient thermalization via elastic and charge transfer ion-neutral collisions, is significant only in space charge dominated regions. The bulk of energy coupled to electrons is stored in electron impact excitation of vibrational and electronic states of molecules, as well as molecular dissociation and ionization. Thus, kinetics of subsequent energy transfer processes among internal energy states, as well as recombination of atoms, electrons, and ions, where significant energy fraction is dissipated as heat, are critically important for predicting the rate of energy thermalization in electric discharges and afterglow.

Time scales for energy thermalization during collisional quenching (relaxation) of excited states and recombination may vary by several orders of magnitude, depending on the type of excited states involved (vibrational and electronic), temperature, pressure, chemical composition of the mixture, and ionization fraction. For example, energy thermalization processes in dry air plasma range from fairly slow (such as vibrational relaxation of the ground electronic state of nitrogen) to quite rapid (such as quenching of excited electronic states of N₂ and O atoms). Adding rapid “relaxer” species to air plasmas, such as CO₂, NO, or water vapor, may significantly accelerate the rate of vibrational energy relaxation / energy thermalization [91]. Finally, adding fuel species, such as hydrogen or hydrocarbons, may considerably complicate kinetics of temperature rise, due to chemical energy release in plasmachemical reactions of fuel oxidation [92,93]. Quantitative insight into kinetics of energy thermalization and temperature rise over a wide range of time scales requires (i) energy coupling to the plasma by short duration pulsed discharges, and (ii) gas temperature measurements during the discharge pulse and in the afterglow, with high time resolution. Spatially resolved temperature measurements are also desirable because of significant temperature gradients generated in high specific energy loading electric discharges.

Kinetics of “rapid” heating in nitrogen and air plasmas (rapid in the sense of the time scale being much shorter compared to vibrational relaxation time) has been extensively studied recently, both experimentally and using kinetic modeling calculations. Discharge input energy fraction dissipated during rapid heating in air plasmas over a wide range of reduced electric fields, E/N = 60-250 Td, was predicted in Ref. [94], in good agreement with experimental data on dynamics of temperature rise in gas discharges in air. More recent experimental studies focused on time-resolved temperature measurements in single-pulse nanosecond duration discharges, primarily by optical emission spectroscopy [95-98], although spatially resolved CARS and spontaneous Raman scattering measurements have also become available [99-102]. Kinetic modeling analysis of rapid heating processes based on optical emission spectroscopy data, up to E/N = 1000 Td, has been done in Refs. [96,103]. The results suggest that at E<200 Td, quenching of electronically excited N₂ molecules by O₂ and of excited O(¹D) atoms by N₂ are the main energy transfer channels contributing to rapid heating, while at E>400 Td, quenching of excited N(²D)

atoms, as well as electron-ion and ion-ion recombination become dominant. An extensive review of relevant experimental and modeling results is given in a recent kinetic modeling study [104], where predictions of a self-consistent kinetic model of an electric discharge in N₂-O₂ mixtures were compared with time-resolved temperature measurements in a ms pulse DC discharge and afterglow in air by Quantum Cascade Laser Absorption Spectroscopy (QCLAS) [105]. The results show that gas heating on short time scales occurs via quenching of electronically excited N₂ molecules by O₂, consistent with Ref. [96], while temperature rise on a longer time scale is also affected by vibrational relaxation of N₂ by O atoms, O atom recombination on the wall, and an exothermic reaction N(⁴S) + NO(X²Π) → N₂(X¹Σ) + O(³P).

Our previous psec CARS temperature measurements in a single pulse, “diffuse filament” nanosecond pulse discharge in air at P=100 torr [100,106], on nanosecond to millisecond time scales, demonstrated that temperature rise during and after the discharge pulse occurs in two well-pronounced stages, separated in time. These results provide direct evidence of “rapid” and “slow” energy thermalization mechanisms in air plasmas. They also suggest significant effect of N₂ vibrational relaxation on oxygen species since “slow” temperature rise, detected in air, was almost entirely missing in nitrogen [106].

The objective of the present work is to use pure rotational psec CARS for time-resolved and spatially resolved temperature measurements in this type of discharge, along with kinetic modeling, to elucidate the dominant kinetic mechanisms involved in energy thermalization in air and H₂-air plasmas.

Short discharge pulse duration used in the present work (~100 ns) and high time resolution of CARS diagnostics allow resolving temperature rise on a short (nanosecond) time scale, while fairly large diameter of the discharge filament (approximately 2 mm) makes possible temperature measurements on a long (millisecond) time scale, before radial diffusion becomes dominant. The advantage of using pure rotational CARS, compared to vibrational CARS using in Ref. [100,106], is that the spacing between the individual pure rotational transitions is much larger than that for the Q-branch vibrational transitions. In Refs. [100,106], rotational-translational temperature was inferred from partially resolved vibrational CARS spectra ($v=0$ to $v=1$ Q-branch transition), which somewhat limits its accuracy. The use of pure rotational CARS also mitigates Stark line broadening effects when high pulse energies are used.

III.2. Experimental

The experiments were carried out in a six-arm cross glass cell with quartz windows, shown schematically in Fig. III.1. The discharge cell is similar to the cell used in [100,106] to study a stable, reproducible point-to-point discharge between two spherical electrodes, where the filament dimensions are sufficiently small to achieve significant specific energy loading, yet large enough to enable diagnostic studies and reduce mass diffusion effects. In the present work, the discharge was sustained between two copper spherical electrodes 7.5 mm in diameter, separated by a gap of 9 mm. The experiments were carried out in dry air and fuel-air mixtures at the pressure of 40 Torr.

The volumetric flow of air through the discharge cell was set to 310 sccm for all gas mixtures used in the present work. The hydrogen flow rate was set to 18 sccm for the equivalence ratio of $\varphi = 0.14$, 54 sccm for $\varphi = 0.42$, and 107 sccm for $\varphi = 0.83$. These conditions correspond to an estimated flow velocity of approximately 2 cm/s at room temperature, assuming uniform flow through a circular tube 3 in. diameter (the diameter of the cell arms). This flow velocity is sufficiently high to ensure that the CARS probe region ~ 0.5 mm long [100] experiences only one discharge pulse, and that heat generated during and after the discharge pulse is dissipated by convection and radial heat conduction.

The discharge electrodes were connected to a custom-made high voltage pulse generator [107], generating alternating polarity pulses and operated at a pulse repetition rate of 60 Hz. The pulse generator is designed to generate a relatively low voltage “pre-pulse” several microseconds prior to producing a

“main” high-voltage pulse. The pre-pulse polarity is opposite to the main pulse polarity; also, the polarity of main pulses alternates during the operation. For open load conditions (i.e. when the pulse generator is disconnected from the electrodes), or for dielectric barrier discharge load [108], the pre-pulse voltage is typically 4-5 kV for the main pulse voltage of 15-20 kV. At the present conditions of a pulsed discharge between two metal electrodes, when breakdown voltage is significantly lower compared to open load pulse voltage, peak voltages for the pre-pulse and the main pulse, separated by approximately 6 μ s, were close to each other, approximately 4.5 kV. Thus, at the present conditions the discharge is sustained by pairs of opposite polarity pulses (a “pre-pulse” and a “main” pulse), generated at the repetition rate of 60 Hz.

To assess shot-to-shot reproducibility of the discharge filament, broadband plasma emission images of a single-pulse discharge in air and in H₂-air mixtures were taken by Princeton Instruments PIMAX ICCD camera with a UV lens (UV-Nikon 105 mm f/4.5 Nikon).

Time-resolved translational-rotational temperature during and after the discharge pulse has been measured by picosecond, broadband, pure Rotational Coherent Anti-Stokes Raman Scattering (R-CARS). The main advantage of broadband CARS, compared to narrowband or scanning CARS, is that it allows single-shot acquisition of highly transient phenomena and reduces the overall acquisition time [109].

The schematic of the diagnostic set-up is shown in Fig. III.2. The second harmonic output of a picosecond Nd:YAG, ~ 150 ps pulse duration, (Ekspla SL333) is divided into two beams using a half wave-plate and a thin-film polarizer. The ratio of power between the two beams can be adjusted by rotating the half-wave plate. The high power beam, which is vertically polarized, is reserved to pump a custom-built broadband modeless dye laser. The horizontally polarized low-power beam is used to produce the probe pulse and passes through a second half wave plate to rotate the polarization so that it is orthogonal to the polarization of the pump pulse. In the present work, the probe beam has horizontal polarization and energy ranging from ~1 to 5 mJ/pulse.

As shown in Fig. III.2, the pump, Stokes, and probe beams are focused into the test cell with a 150 mm spherical lens using a planar-BOXCARS phase matching configuration [120], producing a cylindrical probe region with diameter of less than 100 μ m and interaction length of ~0.5 mm. The diameter of the probe region was estimated by passing the laser beams through a 100 μ m pinhole. The interaction length is measured by translating a glass plate (microscope cover slip 100 μ m thick) along the length of the beam overlap region using a translation stage, and measuring the resulting non-resonant background signal from the plate. These measurements have shown that approximately 95% of the signal originated over the interaction length of 0.5 mm. The CARS signal is generated over the interaction length, and is spatially filtered using irises, after re-collimation by a 200 mm lens. The signal is then focused by a 100 mm spherical lens into a 0.75-m spectrometer equipped with a 1200 line/mm grating (Shamrock 750). The spectra are detected using a back-illuminated electron-multiplying CCD camera (EMCCD, Andor). The signal was accumulated over 1000 to 3500 laser shots (i.e. over 100 to 350 seconds).

To improve signal discrimination and reduce noise due to scattering of the probe beam, a polarization approach [121] is employed, previously used by Zuzeek [92,93] for pure rotational CARS temperature measurements in H₂-air and C₂H₄-air plasmas. Briefly, since the signal and the probe beam have orthogonal polarizations, placing a high extinction thin-film polarizer (CVI) into the CARS signal path reduces the polarized stray light by more than a factor of 1000. CARS resonant and non-resonant signals, however, are reduced to a factor of 9/16 and 1/9, respectively, compared to signals which would be obtained for parallel polarizations. This has the effect of reducing the influence of the non-resonant background. Time delay between the probe and the Stokes beam is controlled by translating a prism mounted on a translation stage, placed into the beam path. By adjusting the time delay, the temporal overlap of all three beams was optimized by maximizing the non-resonant signal obtained from a microscope cover slip, and was held the same for the work present here.

Background, caused mainly by scattering of the probe and pump beams, was subtracted from the experimental spectra by blocking the Stokes beam. After background subtraction, the spectra were normalized and corrected for the dye laser output distribution. For this, the spectra were divided by the reference non-resonant background spectrum, obtained before data collection by placing a 1 mm thick glass microscope slide into the CARS probe region. The reference spectrum also accounts for the convolution of the probe beam with the broadband dye laser. Finally, the square root of the spectrum was compared with synthetic CARS spectra generated using the Sandia CARSFIT code [112], using least squares fitting to the experimental data.

III.3. Kinetic model

A kinetic modeling study of the nanosecond pulse discharge between two spherical electrodes was carried out using a one-dimensional axial model of a nanosecond pulse discharge developed in our previous work [113]. The model has been validated by comparing its predictions with time-resolved measurements of N₂(v=0-4) vibrational level populations, as well as time-resolved, absolute number densities of O atoms, N atoms, and NO [114], showing good agreement [113]. In particular, these results demonstrated that reactive quenching of multiple excited electronic levels of N₂ by O atoms is the dominant channel of NO formation in the afterglow of a nanosecond pulse discharge in air.

Briefly, the kinetic model includes time-dependent conservation equations for number densities of charged species (electrons, positive ions, and negative ions) and neutral species (including excited electronic states of N₂, O₂, N, and O), equation for the electron temperature, Poisson equation for the axial electric field, and heavy species energy equation. Full description of the model can be found in Ref. [113]. Vibrational level populations of nitrogen in the ground electronic state are calculated using master equation, which includes state-specific processes of N₂ vibrational excitation by electron impact, vibration-to-vibration (V-V) energy exchange, vibration-to-translation (V-T) energy relaxation, and chemical reactions of vibrationally excited molecules. The present model includes 40 excited vibrational levels of nitrogen, of which the first 17 levels are excited by electron impact.

Experimental cross sections for electron impact excitation of low vibrational levels, v=1-8, are taken from [115], and theoretical cross sections for excitation of higher levels, v=9-17, are taken from [116]. The expressions for state-specific single-quantum rates of V-T and V-V energy transfer in nitrogen, used in the present model, were taken from [117],

$$k_{v \rightarrow v-1} = v \cdot k_{1 \rightarrow 0} \cdot e^{\delta_{VT}(v-1)} \quad (\text{III.1})$$

$$k_{v \rightarrow v+1}^{w+1 \rightarrow w} = (v+1) \cdot (w+1) \cdot k_{0 \rightarrow 1}^{1 \rightarrow 0} \cdot e^{\delta_{VV}|v-w|} \cdot \left(\frac{3}{2} - \frac{1}{2} e^{\delta_{VV}|v-w|} \right) \quad (\text{III.2})$$

In Eqs. (III.1, III.2), v and w are vibrational quantum numbers, δ_{VT} and δ_{VV} are “radii” for V-T and V-V energy transfer,

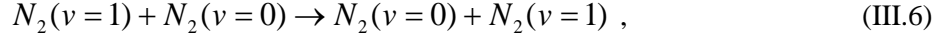
$$\delta_{VT} = \frac{2.87}{T^{1/3}}, \quad (\text{III.3})$$

$$\delta_{VV} = \frac{6.85}{\sqrt{T}}, \quad (\text{III.4})$$

T is the rotational-translational temperature (“gas temperature”), $E_1 = 3353$ K and $\Delta E = 20.6$ K are the energy of N₂ vibrational transition $v=1 \rightarrow 0$ and the molecular anharmonicity, respectively, and $k_{1 \rightarrow 0}(T)$ and $k_{1 \rightarrow 0}^{0 \rightarrow 1}(T)$ are the rates of V-T and V-V energy transfer processes



and



respectively. Temperature-dependent rates of V-T relaxation of nitrogen by N_2 , O_2 , N , and O , used in the present model, $k_{1\rightarrow0}(T)$, were taken from Ref. [118], which provides curve fits to the available experimental data. Specifically, the room temperature rate coefficient for N_2 V-T relaxation by O atoms is $k_{1\rightarrow0}(T = 300\text{ K}) = 3 \cdot 10^{-15} \text{ cm}^3/\text{s}$ [119]. The rates of N_2 V-T relaxation by N atoms were taken the same as relaxation rates by O atoms. Note that this is an upper bound estimate since theoretically predicted low-temperature V-T rates for N_2 - N are very slow [120]. The same assumption was made for N_2 V-T relaxation by H atoms. This use of this assumption, however, is unlikely to affect the model predictions significantly, since both N atom and H atom number densities at the present conditions are significantly lower compared to that of O atoms (predicted peak number density of $[O] \approx 9 \cdot 10^{15} \text{ cm}^{-3}$), such that vibrational relaxation of nitrogen occurs primarily in collisions with oxygen atoms. V-T relaxation rates of nitrogen by H_2 were calculated using $k_{1\rightarrow0}(T = 300\text{ K})$ from Ref. [121], with temperature dependence suggested in Ref. [112]. The room temperature rate coefficient of N_2 - N_2 V-V relaxation, $k_{1\rightarrow0}^{0\rightarrow1}(T = 300\text{ K}) = 1.5 \cdot 10^{-14} \text{ cm}^3/\text{s}$, was taken from Ref. [123], where state-specific V-V rates were inferred from measurements of temporal evolution of $N_2(v=0\text{-}6)$ vibrational levels populations, excited by stimulated Raman scattering. The value of thus rate coefficient agrees well with a three-dimensional Forced Harmonic Oscillator – Free Rotation model [124], which also predicts its temperature dependence, $k_{1\rightarrow0}^{0\rightarrow1}(T) \sim (T[K]/300)^{3/2}$, in good agreement with semiclassical trajectory calculations [125].

As will be shown in Section III.4, at the present experimental conditions the net rate of vibrational energy relaxation to heat is dominated by rapid V-T relaxation of nitrogen molecules by O atoms. Vibrational excitation of oxygen molecules was not taken into account, since discharge input energy fraction going into vibrational excitation of O_2 by electron impact is much lower compared to that of N_2 . Also, at the present low-temperature conditions, V-V energy transfer from N_2 to O_2 is very slow, due to large disparity of vibrational quanta [126]. Finally, room-temperature V-T relaxation rate of O_2 by O atoms is much faster compared to that of N_2 by O , $k_{1\rightarrow0}(O_2 - O) = 3 \cdot 10^{-12} \text{ cm}^3/\text{s}$ [127] vs. $k_{1\rightarrow0}(N_2 - O) = 3.5 \cdot 10^{-15} \text{ cm}^3/\text{s}$ [129]. Indeed, recent measurements of N_2 and O_2 vibrational level populations in a nanosecond pulse discharge in air at $P=1$ atm [128] have shown that vibrational disequilibrium of O_2 is much less pronounced compared to that of N_2 .

The cross sections of electron impact reactions were taken from Ref. [129, 130], and rates of ion-molecule reactions with hydrogen-containing species, as well as rates of neutral species chemical reactions in H_2 - O_2 mixtures were taken from Ref. [131].

The apparent diameter of the discharge filament, inferred from ICCD images of broadband plasma emission, is approximately $d=2.0$ mm. The discharge filament diameter determined from the gas temperature radial distribution (see Section III.4) is also approximately $d=2.0$ mm. This value was used in the calculations of discharge current, since the one-dimensional axial model predicted the current density. The modeling calculations were carried out in dry air, modeled as a 78.5% N_2 / 21.5% O_2 mixture, and in hydrogen-air mixtures at a pressure of 40 Torr.

At high discharge specific energy loadings, the one-dimensional axial model, which predicts discharge current density as well as axial distributions of the electric field and species number densities, cannot predict time-dependent gas pressure and temperature. At these conditions, time evolutions of pressure and temperature are controlled to a significant extent by rapid heating in the discharge (rapid

compared to the acoustic time scale, $\tau_{acoustic} \sim R/a$, where R is the filament radius and a is the speed of sound), with subsequent compression wave propagation in the radial direction. The former process may produce a significant temperature and pressure overshoot, while the latter process results in rapid gasdynamic expansion and cooling. To incorporate these process into analysis, temperature and pressure evolution in the afterglow are modeled using a one-dimensional radial axisymmetric model, which includes time-dependent equations for conservation of mass, momentum, energy, species concentrations, and master equation for vibrational excitation of nitrogen, listed below:

$$\frac{\partial}{\partial t} \rho = -\frac{1}{r} \frac{\partial}{\partial r} (r \rho v) \quad (\text{III.7})$$

$$\frac{\partial}{\partial t} (\rho v) = -\frac{1}{r} \frac{\partial}{\partial r} (r \rho v^2) - \frac{\partial p}{\partial r} + \nabla W_r - \frac{2v}{3r} \left(\frac{2\mu}{r} + \frac{\partial \mu}{\partial r} \right) \quad (\text{III.8})$$

$$\frac{\partial}{\partial t} (\rho \varepsilon) = -\frac{1}{r} \frac{\partial}{\partial r} (r \rho v \varepsilon) - \frac{p}{r} \frac{\partial}{\partial r} (rv) + \frac{1}{r} \frac{\partial}{\partial r} \left(r \lambda \frac{\partial T}{\partial r} \right) + W_\varepsilon \quad (\text{III.9})$$

$$\frac{\partial n_i}{\partial t} = -\frac{1}{r} \frac{\partial}{\partial r} \left(r n_i v - r D_i \cdot N \cdot \frac{\partial \left(\frac{n_i}{N} \right)}{\partial r} \right) + S_i - L_i n_i \quad (\text{III.10})$$

$$\begin{aligned} \frac{\partial n_v}{\partial t} = & -\frac{1}{r} \frac{\partial}{\partial r} \left(r n_v v - r D_v \cdot N \cdot \frac{\partial \left(\frac{n_v}{N} \right)}{\partial r} \right) + \\ & + n_e [N_2] k_v^+ - n_e [N_2] k_v^- + n_{v-1} [N_\beta] k_{v,v-1} + n_{v+1} [N_\beta] k_{v+1,v} - n_v (k_{v,v-1} + k_{v,v+1}) + \\ & + n_{v-1} \sum_w n_{w+1} k_{v-1,v}^{w+1,w} + n_{v+1} \sum_w n_w k_{v+1,v}^{w,w+1} - n_v (\sum_w n_{w+1} k_{v,v+1}^{w+1,w} + \sum_w n_w k_{v,v-1}^{w,w+1}) \end{aligned} \quad (\text{III.11})$$

In Eqs. (III.7 – III.9), ρ is the density, v is the radial flow velocity, p is the pressure, T is the temperature, $\mu=\mu(T)$ and $\lambda=\lambda(T)$ are the viscosity and the thermal conductivity, and ε is the specific enthalpy of the mixture, which also includes non-equilibrium vibrational energy of N_2 ,

$$\rho \varepsilon = \frac{1}{N_A} \sum_i (\Delta H_f^i + C_p^i T) n_i + k_B \sum_v E_v n_v , \quad (\text{III.12})$$

where n_i is the number density of species i , ΔH_f^i and C_p^i are the standard formation enthalpy and the equilibrium specific heat at constant pressure, E_v and n_v are the energy (in K) and the population of vibrational level v of N_2 molecule, N_A and k_B are the Avogadro number and the Boltzmann constant. The viscous dissipation terms, W_r and W_ε , are the same as in Ref. [131]. In Eq. (III.10), n_i is the number density of species i , N is the total number density, D_i is the diffusion coefficient, and terms S_i and L_i represent its production and loss rates. In Eq. (III.11), n_v are absolute populations of excited vibrational levels of $N_2(v>0)$, k_v^+ and k_v^- are rate coefficients for electron impact excitation and de-excitation of vibrational level v , $k_{v,v\pm 1}$ are rate coefficients for V-T relaxation, N_β are number densities of “relaxer” species (N_2 , O_2 , H_2 , N , O , and H), and $k_{v,v\pm 1}^{w,w\pm 1}$ are rate coefficients for N_2-N_2 V-V exchange.

The calculations using the radial model begin after the applied voltage falls to zero. The initial conditions for the radial model on the discharge centerline are predicted by the axial model at the end of the discharge pulse, halfway between the electrodes. The initial radial distributions of temperature,

pressure, and species number densities are assumed to be Gaussian with FWHM of $d=2.0$ mm, e.g. $n_i(r) = n_i(r=0) \cdot \exp\{-[r/(d/2)]^2\}$. Thus, the pressure overshoot caused by heating on sub-acoustic time scale, and the subsequent pressure reduction caused by compression wave propagation, were taken into account using the radial axisymmetric model for afterglow simulations. This approach works well in the entire discharge gap, except in the cathode layer region, where the compression wave becomes markedly non-one-dimensional [106]. Note that the present temperature measurements are made halfway between the electrodes, where the effect of the cathode layer on energy thermalization dynamics is minor. The present approach provides a straightforward, low computational cost alternative to a two-dimensional model of a transient high-pressure electric discharge in a compressible gas mixture, coupled to master equation and nonequilibrium plasma chemistry processes.

III.4. Results and Discussion

Figure III.3 shows typical ICCD camera images of broadband plasma emission in a nanosecond pulse discharge in air. The camera gate was set to 100 ns and timed to overlap with the discharge pulse, during a single shot, pre-pulse or main pulse discharge. The images in Fig. III.3(a,b) are taken during the pre-pulse discharge (positive and negative polarity, respectively), and the images in Fig. III.3(c,d) are taken during the main pulse discharge. In all images, the bottom electrode is grounded. In all four cases, the plasma filament images were reproducible, exhibiting essentially no detectable difference shot-to-shot. It can be seen that the discharge filament generated during the pre-pulse is more diffuse compared to the filament generated by the main pulse, produced approximately 6 μ s after the pre-pulse, such that filament contraction is evident. From Fig. III.3, it can also be seen that weak plasma emission envelopes the electrode that plays the role of the cathode during the pulse. Since the energy coupled to the plasma during the main pulse is significantly higher compared to the pre-pulse, the effective plasma filament diameter (FWHM) used in the kinetic modeling calculations, $d=2.0$ mm, was inferred from the radial distributions of plasma emission intensity shown in Fig. III.3(c,d).

Figure III.4 shows typical experimental and synthetic “best fit” rotational CARS spectra taken at two different conditions, (a) at relatively low temperature, in air, and (b) at relatively high temperature, in a hydrogen-air mixture at the equivalence ratio of $\phi=0.42$. It can be seen that individual rotational transitions are widely separated, and significant difference between these two spectra is apparent. Specifically, at higher temperatures high rotational energy levels are populated, such that signal is detected primarily from transitions with larger Raman shift. The synthetic spectra were generated by a computer code CARSFIT [112]. From Fig. III.4, it can be seen that the experimental and the synthetic spectra match each other closely. The “best fit” rotational temperature, $T=297\pm1$ K and $T=733\pm26$ K, respectively, were determined from the least squares fits, using the following procedure. For both sets of experimental conditions shown in Fig. III.4, five CARS spectra were taken. For each experimental spectrum, the temperature was inferred from the best fit synthetic spectrum, and the average of the five temperature values was determined. The uncertainties reported in the present work represent the 95% confidence interval for the average temperature values inferred using this procedure. This corresponds to the precision of the temperature data. As discussed in Section III.1, pure rotational CARS has the inherent advantage compared to vibrational Q-branch CARS, that high pump/Stokes beam intensities can be employed without distortion of the spectra caused by Stark broadening/shifting effects.

Figure III.5 plots experimental voltage and current pulse waveforms, as well as discharge current waveforms predicted by the kinetic model in air, during (a) negative polarity pre-pulse and (b) positive polarity main pulse produced approximately 6 μ s later. The experimental voltage pulse waveform is used as one of the input parameters of the kinetic model. Since the one-dimensional axial model predicts current density rather than current, the predicted current density was multiplied by the estimated filament cross sectional area based on the FWHM diameter inferred from the radial distribution of plasma emission (see Fig. III.3) and temperature distributions (see Fig. III.5), $d=2.0$ mm. Comparison of the

experimental and the predicted current during the pre-pulse and the main pulse shows good agreement. Note that although peak voltages during the pre-pulse and the main pulse are close to each other, 4.4 kV and 4.6 kV, respectively (see Fig. III.5), the initial electron concentration before the pre-pulse is much lower compared to that before the main pulse. This results in much higher peak current and significantly higher coupled energy during the main pulse than during the pre-pulse (compare Figs. III.5(a) and (b)). Additional energy is coupled to the plasma between the pre-pulse and the main pulse (at $t < 1 \mu\text{s}$, see Fig. III.5(a)), since voltage and current do not fall completely to zero.

Figure III.6 plots radial distributions of rotational/translational temperature measured in air at three different moments in time, (a) 1.74 μs before the positive polarity main pulse (i.e. 4.3 μs after the negative polarity pre-pulse), (b) 1.44 μs after the main pulse, and (c) 168 μs after the main pulse. Temperatures measured after the pre-pulse are in the range $T=305\text{--}335 \text{ K}$. After the main pulse, temperature on the centerline increases considerably, peaking at $T=680 \text{ K}$ 168 μs after the pulse. Radial temperature distributions predicted by the kinetic model 1.44 μs and 168 μs after the main pulse are also plotted in Fig. III.6, showing good agreement with the experimental results.

Figure III.7 presents experimental and predicted temperature during and after the discharge pulse in air, as well as the experimental discharge energy coupled to the plasma. Energy coupling to the plasma during the pre-pulse (at $t < 100 \text{ ns}$, $\approx 0.7 \text{ mJ}$) and by the main pulse (at $t \approx 6 \mu\text{s}$, $\approx 3.2 \text{ mJ}$) is clearly evident. The duration of both current pulses (the pre-pulse and the main pulse) is comparable, $\sim 100 \text{ ns}$ (see Fig. III.5). From Fig. III.7, it is apparent that the pre-pulse generates fairly modest heating of the plasma filament, up to $\Delta T \sim 50 \text{ K}$, while the main pulse produces rapid heating of the plasma by $\Delta T \sim 150 \text{ K}$, up to $T \approx 500 \text{ K}$, consistent with the model predictions. Note that this rapid temperature rise is not fully resolved in time in Fig. III.7, and is shown in greater detail in Fig. III.8. In the afterglow after the main pulse, the temperature continues to increase gradually, on the time scale of approximately 200 μs , peaking at $T \approx 680 \text{ K}$, after which it decreases slowly to near room-temperature over about 20 ms, again consistent with the model predictions (see Fig. III.7).

Experimental and predicted gas temperature during and after the main positive polarity discharge pulse in air, plotted in Fig. III.7, are shown in greater detail in Fig. III.8, where $t=0$ corresponds to the beginning of the main pulse current rise. To illustrate the dominant kinetic mechanisms controlling dynamics of temperature rise at these conditions, Fig. III.8 also plots (a) the total number density of excited electronic states of nitrogen, N_2^* , including $N_2(A^3\Sigma_u^+)$, $N_2(B^3\Pi_g)$, $N_2(W^3\Delta_u)$, $N_2(B^3\Sigma_u^-)$, $N_2(C^3\Pi_u)$, $N_2(E^3\Sigma_g^+)$, $N_2(a^1\Sigma_u^-)$, $N_2(a^1\Pi_g)$, $N_2(w^1\Delta_u)$, and $N_2(a''^1\Sigma_g^+)$, (b) O atom number density, and (c) “first level”

$$\text{vibrational temperature of } N_2, T_v(N_2) = \frac{E_1}{\ln(n_0/n_1)}.$$

Both vibrational and electronic excitation are produced by electron impact during the discharge pulse. From Fig. III.8, it can be seen that collisional quenching of excited electronic states of N_2 occurs on the time scale of a few hundred ns after beginning of the discharge pulse, such that their number densities become insignificant by $t \sim 1 \mu\text{s}$. The quenching occurs primarily in collisions with O_2 , resulting in oxygen dissociation, e.g.



with the rate coefficient for the lowest excited state, $N_2(A^3\Sigma)$, of $k(A^3\Sigma)=2.5 \cdot 10^{-12} \text{ cm}^3/\text{s}$, which at the present conditions corresponds to decay time of $\sim 1.5 \mu\text{s}$. For other excited triplet states of N_2 , $C^3\Pi$ and $B^3\Pi$, quenching by O_2 are considerably faster, $k(B^3\Pi)=3 \cdot 10^{-10} \text{ cm}^3/\text{s}$ and $k(C^3\Pi)=3 \cdot 10^{-10} \text{ cm}^3/\text{s}$, respectively, which correspond to decay rates of $\sim 10 \text{ ns}$, such that the decay of these states is controlled primarily by the discharge pulse duration. Figure III.8 illustrates that rapid temperature rise after the main discharge pulse occurs on the same time scale as quenching of excited electronic states of nitrogen molecules by O_2 (a few hundred nanoseconds). Thus, the reaction of Eq. (III.13) is the dominant kinetic process controlling “rapid” heating in ns pulse air plasma at the present conditions, as has been pointed

out previously [94,96].

From Fig. III.8, it can also be seen that the second stage of gas heating occurs on the time scale of $\sim 200 \mu\text{s}$. Comparing the behavior of gas temperature with N_2 vibrational temperature, $T_v(\text{N}_2)$, it can be seen that this “slow” temperature rise begins at the same time when the vibrational temperature starts to decrease. Analysis of the kinetic modeling predictions shows that it occurs due to energy thermalization during V-T relaxation of vibrationally excited N_2 by O atoms,

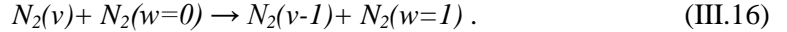


the rate of which is several orders of magnitude faster compared to V-T self-relaxation in nitrogen (at $T=500 \text{ K}$, the rate coefficients are $k_{1 \rightarrow 0}[\text{N}_2-\text{O}] \approx 2 \cdot 10^{-14} \text{ cm}^3/\text{s}$ [122] and $k_{1 \rightarrow 0}[\text{N}_2-\text{N}_2] \sim 10^{-19} - 10^{-20} \text{ cm}^3/\text{s}$ [133]). The time scale for the slow heating can be estimated from the net rate of V-T relaxation of nitrogen by O atoms, as follows,

$$\tau_{\text{slow}} \sim \left(\frac{E_1}{\gamma_2 T} \sum_{v=1} k_{v \rightarrow v-1} [\text{N}_2 - \text{O}] \frac{n_v}{N} n_o \right)^{-1} \sim (10 \cdot k_{0 \rightarrow 1} [\text{N}_2 - \text{O}] n_o)^{-1} \sim 500 \mu\text{s} . \quad (\text{III.15})$$

In Eq. (III.15), the scaling of the V-T rates with the vibrational quantum number is given by Eqs. (III.1, III.3), $n_0 \approx 9 \cdot 10^{15} \text{ cm}^{-3}$ (see Fig. III.8), and relative N_2 vibrational level populations are as predicted by the model (plotted in Fig. III.9 at $t=1 \mu\text{s}$, $50 \mu\text{s}$, and $100 \mu\text{s}$). The estimate of Eq. (III.15) predicts a somewhat longer time scale for the slow heating since τ_{slow} is the time for the temperature to increase by a factor of e .

Note that N_2 vibrational temperature, which increases considerably during the main discharge pulse, due to vibrational excitation by electron impact, continues to rise during the afterglow, on the time scale of a few tens of microseconds after the pulse, peaking at $T_v(\text{N}_2) \approx 1450 \text{ K}$ (see Fig. III.8). This effect, detected in our previous experiments in the afterglow of nanosecond pulse discharges [100,114], as well as in the experiments elsewhere [101,102,128], is due to “downward” V-V transfer in nitrogen with vibrational levels $v \geq 2$ strongly overpopulated by electron impact during the discharge,



Basically, electron impact vibrational excitation in short duration pulsed discharges, with pulse duration shorter compared to the characteristic time for V-V energy exchange,

$$\tau_{vv} \sim \left[\sum_{v=2}^{v \sim 4} k_{v \rightarrow v-1} n_0 \frac{n_v}{n_1} \right]^{-1} \sim [6k_{0 \rightarrow 1}^2 n_0]^{-1} \sim 10 \mu\text{s} , \quad (\text{III.17})$$

produces vibrational level populations $v > 1$ with the slope close to the electron temperature, much higher than the “first level” vibrational temperature. Thus, although the forward rate coefficient of the reaction of Eq. (III.16), $k_{vv}(v,0 \rightarrow v-1,1)$, is lower than the reverse rate coefficient, $k_{vv}(v-1,1 \rightarrow v,0)$ (which can be easily verified from detailed balance), this energy transfer processes occurs in the forward, i.e. “downward”, direction, increasing the $\text{N}_2(v=1)$ population and $T_v(\text{N}_2)$ in the afterglow. In the estimate of Eq. (III.17), we used vibrational level populations $\text{N}_2(1 \leq v \leq 4)$ at the end of the discharge pulse (at $t=1 \mu\text{s}$), plotted in Fig. III.9. This effect is well understood and has been reproduced in modeling calculations in our previous work [113].

At the present conditions, V-T relaxation of N_2 by O atoms relaxation occurs on the time scale of $\sim 200 \mu\text{s}$, approximately an order of magnitude slower compared to N_2-N_2 V-V exchange, and is the dominant process controlling “slow” gas heating. Significant difference between the characteristic times of “rapid” heating (caused by N_2 excited electronic states quenching) and “slow” heating (caused by N_2 V-T relaxation by O atoms), as well as short time scale used for discharge energy addition ($\sim 100 \text{ ns}$) make possible clear separation of these two energy thermalization processes in time (see Fig. III.8). The

two-stage heating mechanism in a nanosecond pulse discharge in air, observed in the present experiments, has also been detected in our previous work [100,106]. However, the present pure rotational CARS temperature measurements are more accurate compared to Q-branch vibrational CARS measurements used in Ref. [100]. Also, in the present work, the two-stage energy thermalization mechanism has been quantified using a self-consistent kinetic model of electric discharge and energy transfer processes in air plasmas.

Figure III.10 compares time-resolved temperature measurements after the main discharge pulse in air and in a H₂-air mixture at $\phi=0.83$. It can be seen that in H₂-air, gas heating also occurs in two stages, similar to air. In this case, however, additional temperature rise occurs between the initial “rapid” heating stage and the “slow” heating stage controlled by vibrational relaxation, in good agreement with kinetic modeling predictions. Analysis of the model predictions shows that this occurs due to energy release during partial oxidation of hydrogen in chemical reactions with radicals generated in the plasma (primarily O and H atoms), both via dissociation by electron impact and in reactive quenching of excited electronic states of N₂ by O₂ and H₂, resulting in their dissociation.

As discussed in Section III.3, the one-dimensional axial kinetic model developed in our previous work [113] is not directly applicable for modeling of nanosecond pulse discharges with significant specific energy loading. Indeed, at the present experimental conditions, significant temperature rise, from $T \approx 350$ K to $T \approx 500$ K occurs on the time scale less than ~ 1 μ s (see Fig. III.8), which is shorter compared to the acoustic time scale, $\tau_{acoustic} \sim R/a \sim 3$ μ s. Such rapid heating results in a significant pressure rise in the discharge filament, with subsequent rarefaction due to gasdynamic expansion and compression wave propagation in the radial direction. These effects have been taken into account by supplementing the one-dimensional axial model, where pressure on the filament centerline was an input parameter, with a one-dimensional radial model, which predicted time-resolved pressure distribution in the discharge gap, plotted in Figs. III.11, III.12. From Fig. III.11, a significant pressure overshoot (by about 50%) on the centerline of the discharge in air, occurring on the time scale of ~ 0.1 - 1.0 μ s, is evident. This overshoot is caused by rapid gas heating due to collisional quenching of N₂ excited electronic states (see Fig. III.8), resulting in temperature rise by $\sim 50\%$ on the same time scale. After initial pressure overshoot, the discharge filament begins to expand and a compression wave begins to propagate in the radial direction (see Fig. III.12), causing rapid pressure fall on the centerline and slight transient rarefaction to $P \approx 35$ Torr, before returning to baseline pressure of $P = 40$ Torr (see Fig. III.11). As expected, the second “slow” stage of gas heating did not produce a finite amplitude compression wave since it occurred on the time scale of ~ 100 μ s, which is much longer compared to the acoustic time scale.

The results of Figs. III.11, III.12 illustrate critical importance of incorporating transient compressibility effects into kinetic modeling of nanosecond pulse discharge with high specific energy loading. The present results also quantify the effect of “rapid” heating on the amplitude of compression waves generated by these discharges, which control flow forcing in nanosecond pulse discharge plasma flow actuators.

III.5. Conclusions

In the present work, time-resolved and spatially resolved temperature measurements, by pure rotational picosecond broadband Coherent Anti-Stokes Raman Spectroscopy (CARS), and kinetic modeling calculations are used to study kinetics of energy thermalization in nanosecond pulse discharges in air and hydrogen-air mixtures. The diffuse filament, nanosecond pulse discharge (pulse duration ~ 100 ns) is sustained between two spherical electrodes at $P=40$ torr and is operated at a low pulse repetition rate, 60 Hz, to enable temperature measurements over a wide range of time scales after the discharge pulse. The experimental results demonstrate high accuracy of pure rotational ps CARS for thermometry measurements in highly transient nonequilibrium plasmas. Rotational-translational temperatures are measured for time delays after the pulse ranging from tens of ns to tens of ms, spanning several orders of

magnitude of time scales for energy thermalization in nonequilibrium plasmas. In addition, radial temperature distributions across the plasma filament approximately 2 mm in diameter are measured for several time delays after the discharge pulse. Kinetic modeling calculations using a state-specific master equation kinetic model of reacting hydrogen-air plasmas show good agreement with experimental data. The results demonstrate that energy thermalization and temperature rise in these plasmas occur in two clearly defined stages, (i) “rapid” heating, occurring on the time scale $\tau_{\text{rapid}} \sim 0.1\text{-}1 \mu\text{s}$, caused by collisional quenching of excited electronic states of N₂ molecules by O₂, and (ii) “slow” heating, on the time scale $\tau_{\text{slow}} \sim 200 \mu\text{s}$, caused primarily by N₂ vibrational relaxation by O atoms (in air) and by chemical energy release during partial oxidation of hydrogen (in H₂-air). Note that the time scale for slow heating, given by Eq. (III.13), strongly depends on discharge energy loading per molecule, which controls both relative populations of N₂ vibrational levels and O atom number density.

These results are consistent with previous kinetic modeling calculations. However, the present work provides experimental verification of the modeling predictions, based on accurate time-resolved and spatially resolved temperature measurements. Since rapid heating occurs on the time scale shorter compared to acoustic time scale, it produces a strong compression wave propagating in the radial direction, predicted by the present kinetic model and detected in previous experiments in nanosecond pulse filament discharges. Both energy thermalization mechanisms have major implications for plasma assisted combustion and plasma flow control. Specifically, rapid heating may strongly affect rates of chemical reactions among radicals generated by electron impact and by quenching of excited electronic species during plasma assisted ignition. Rapid heating also controls the scale of high-amplitude pressure perturbations produced by nanosecond pulse plasma actuators. Finally, slow heating caused by vibrational relaxation, and resultant broadband density perturbations, may affect stability of boundary layer flows forced by surface plasma actuators. Further experiments in near-surface nanosecond pulse discharges are necessary to provide quantitative insight into dynamics of these processes.

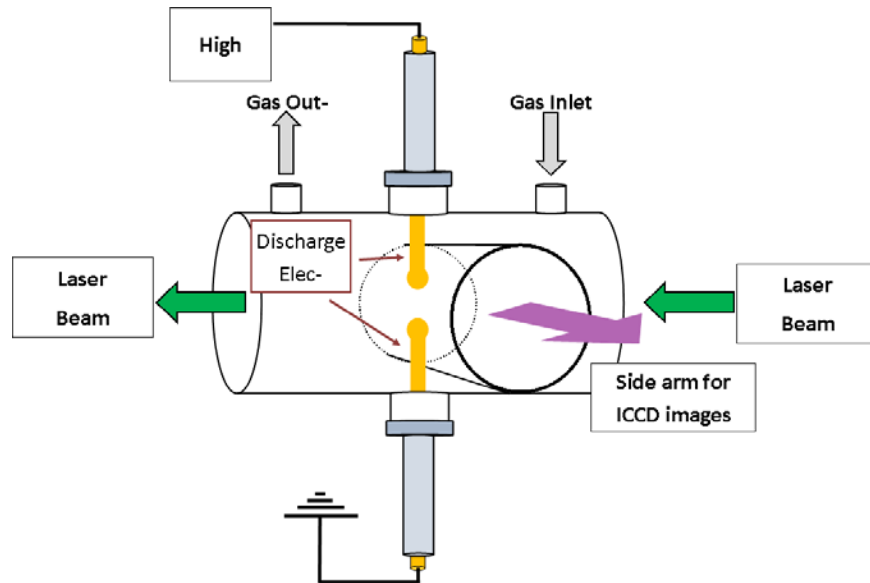


Figure III.1. Schematic of the discharge cell.

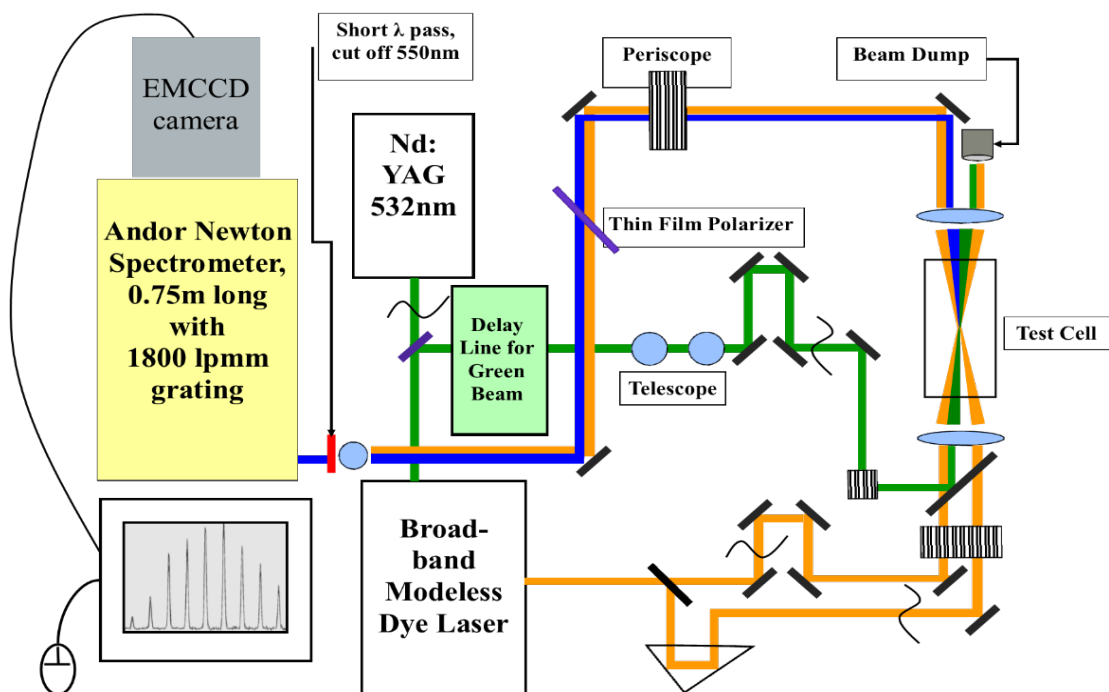


Figure III.2. Schematic of rotational CARS diagnostics.

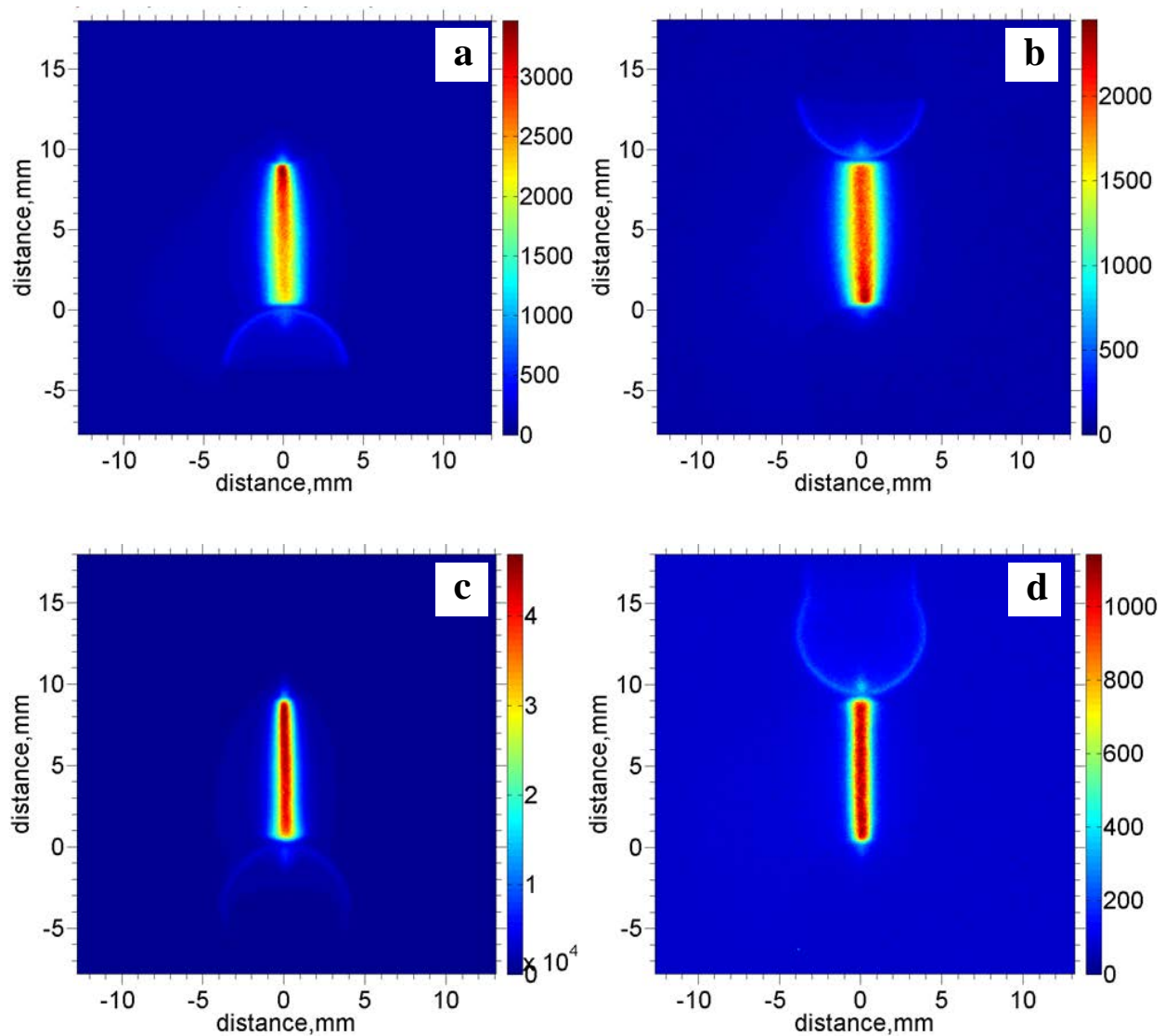


Figure III.3. ICCD images of plasmas generated during pre-pulse, (a) positive polarity and (b) negative polarity, and during main pulse, (c) positive polarity and (d) negative polarity in air at 40 Torr. In all images, bottom electrode is grounded. Camera gate is 100 ns.

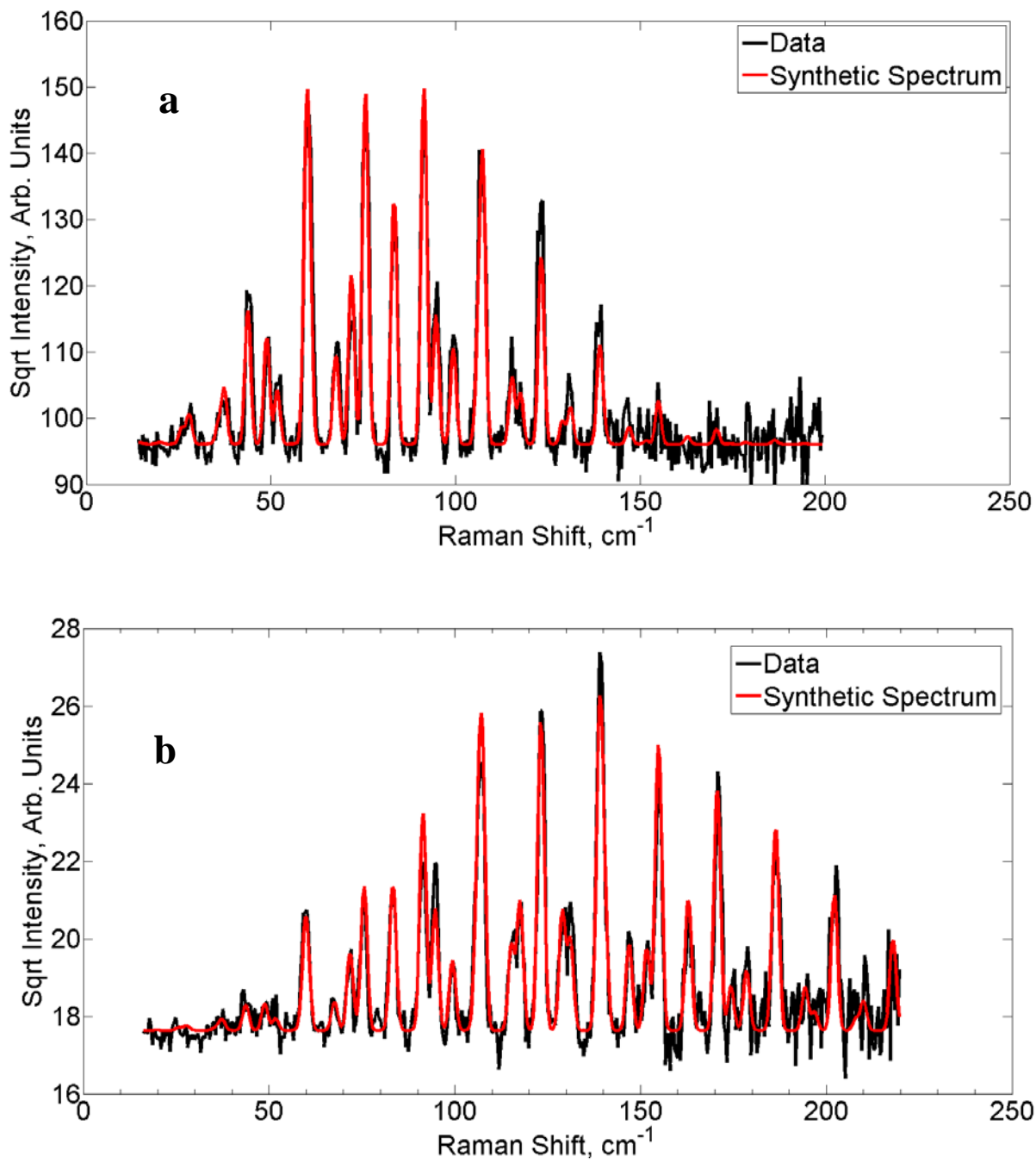


Figure III.4. Typical experimental and synthetic “best fit” rotational CARS spectra taken at two different conditions, (a) at relatively low temperature, in air (top), and (b) at relatively high temperature, in a hydrogen-air mixture at the equivalence ratio of $\phi=0.42$ (bottom). Best fit rotational temperatures for these two cases are $T=297\pm 1$ K and $T=733\pm 26$ K, respectively (the uncertainties represent 95% confidence interval of the average temperature inferred from five experimental spectra).

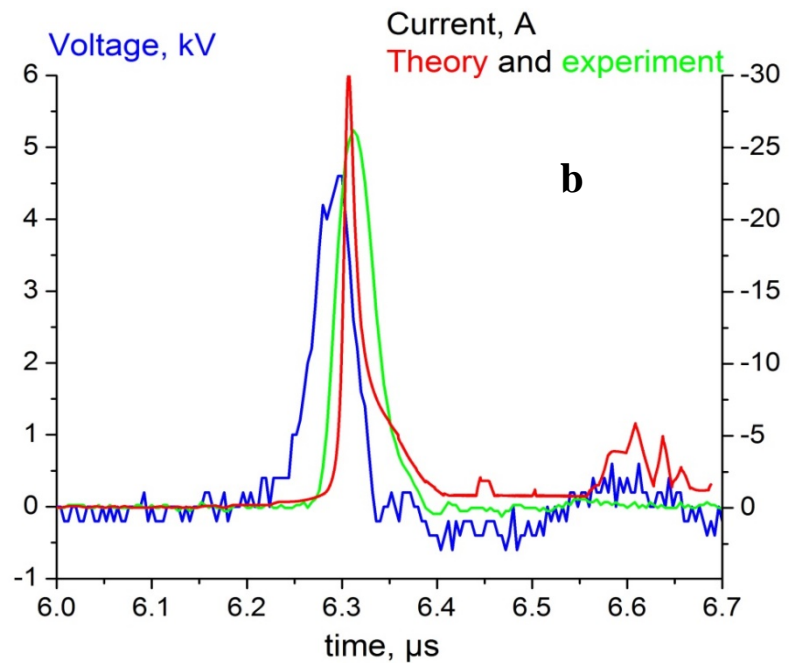
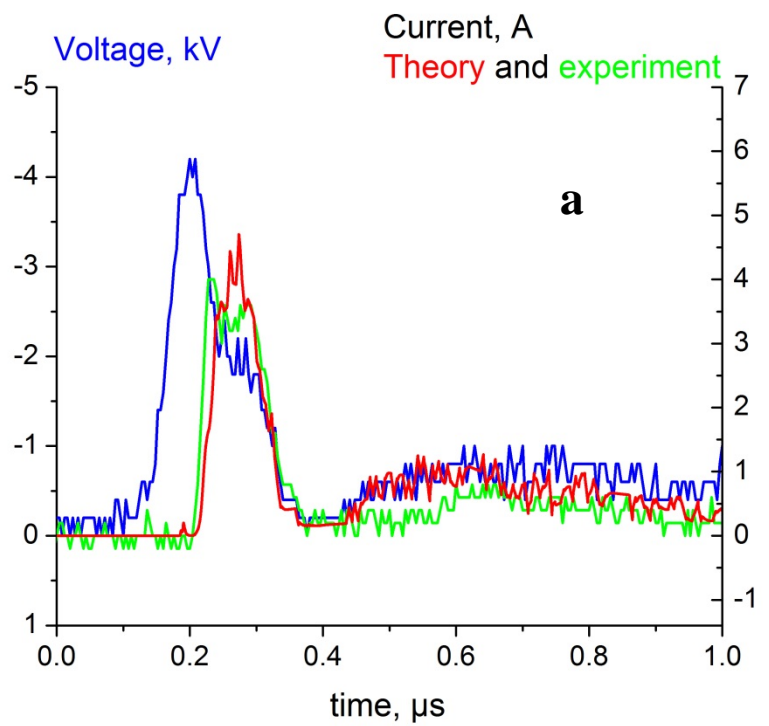


Figure III.5. Applied voltage (experimental) and current (experimental and predicted) waveforms in the discharge in air, (a) during pre-pulse, and (b) during main pulse. Note that pre-pulse is negative polarity and main pulse is positive polarity.

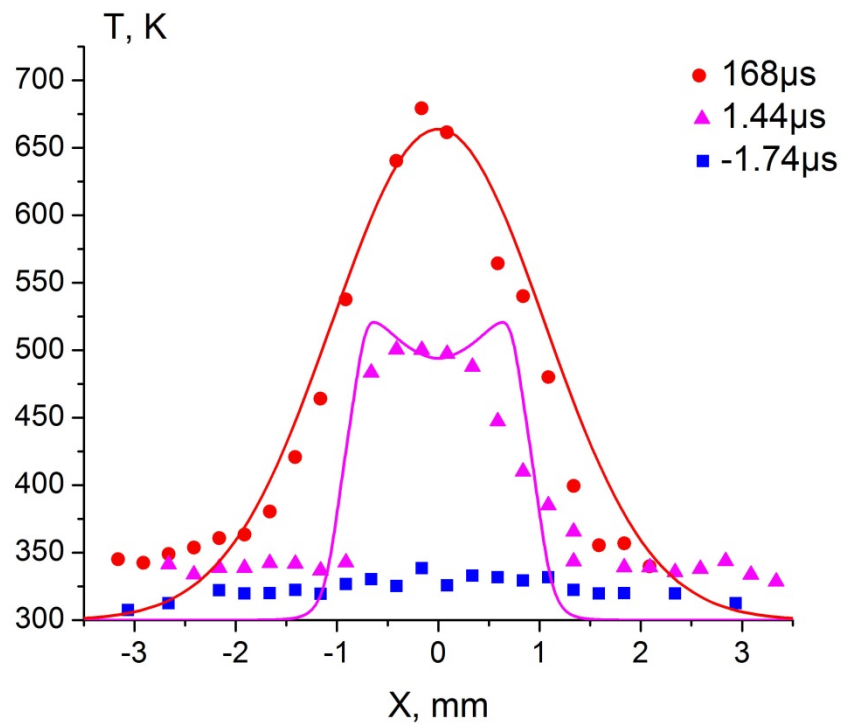


Figure III.6. Experimental and predicted radial distributions of rotational/translational temperature measured at different moments of time, (a) $-1.74 \mu\text{s}$ before the main pulse ($4.3 \mu\text{s}$ after the pre-pulse), (b) $1.44 \mu\text{s}$ after the main pulse, and (c) $168 \mu\text{s}$ after the main pulse. Air, $P=40$ Torr. FWHM of the Gaussian fit shown in 2.0 mm .

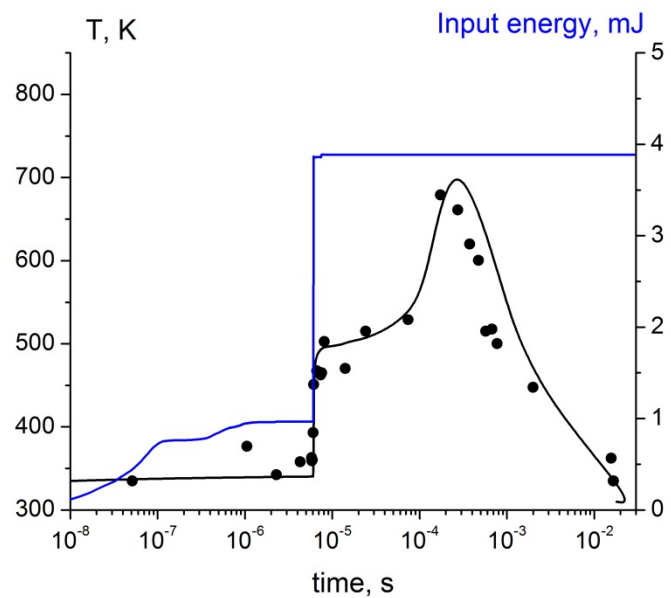


Figure III.7. Experimental (symbols) and predicted (black line) gas temperature, and experimental coupled discharge energy (blue line) in the discharge in air. Energy coupling by the pre-pulse ($t < 100$ ns) and by the main pulse ($\approx 6 \mu\text{s}$) is clearly evident.

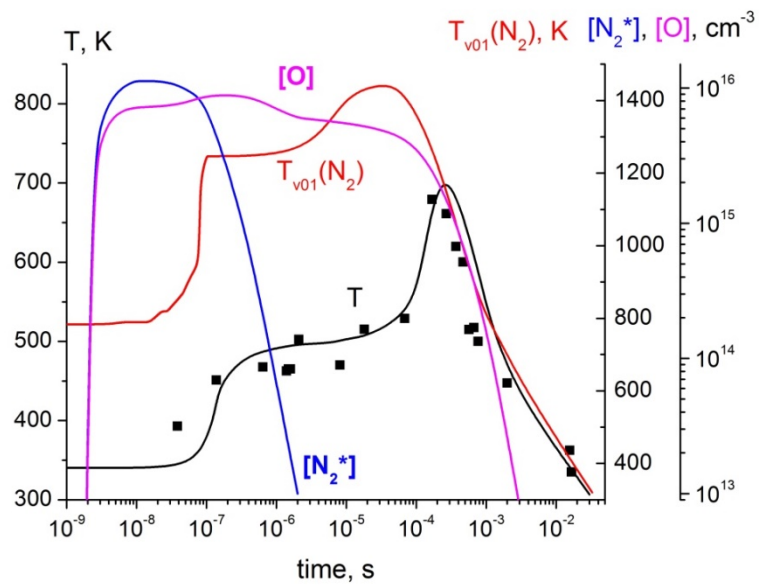


Figure III.8. Time-resolved gas temperature (experimental and predicted), predicted “first level” N_2 vibrational temperature, O atom number density, and total number density of electronically excited states of N_2 during and after main pulse discharge in air.

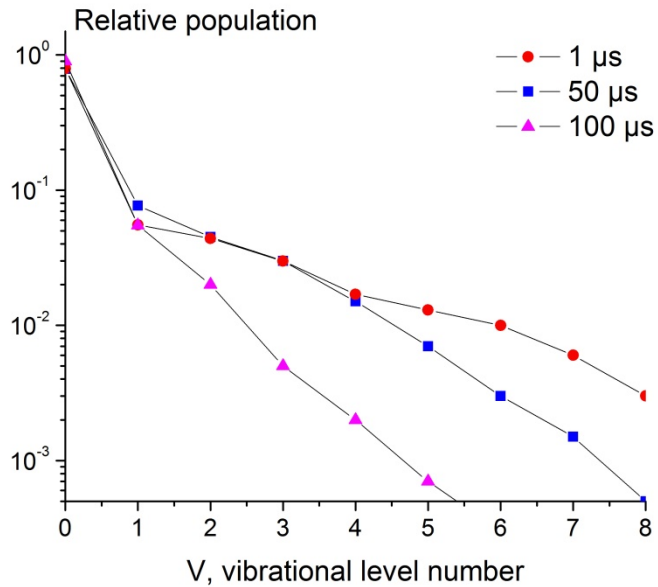


Figure III.9. Predicted N_2 vibrational distribution functions after main pulse discharge in air, at $t = 1 \mu\text{s}$, $50 \mu\text{s}$, and $100 \mu\text{s}$.

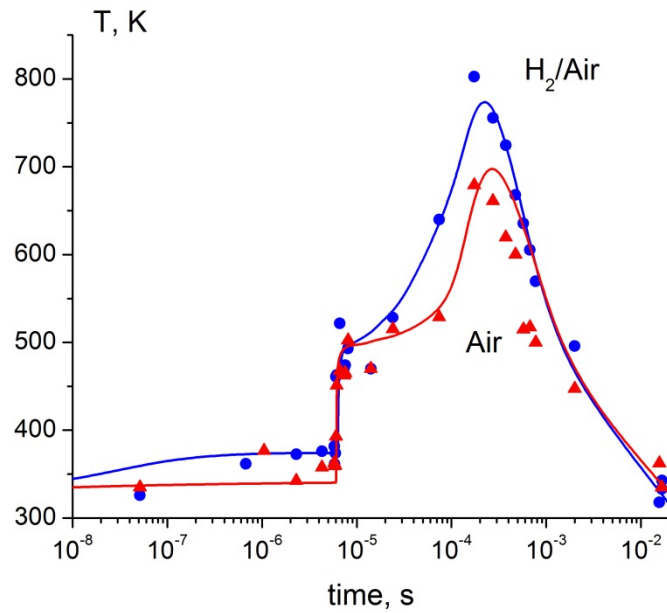


Figure III.10. Time-resolved gas temperature (experimental and predicted) during and after main pulse discharge in air and in H_2 -air mixture at $\varphi=0.42$.

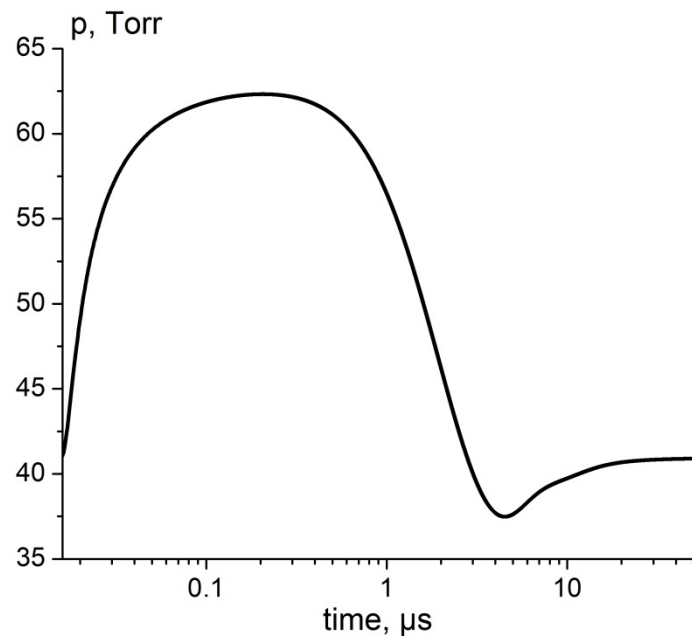


Figure III.11. Time-resolved pressure on the discharge centerline in air, plotted vs. time delay after the main pulse.

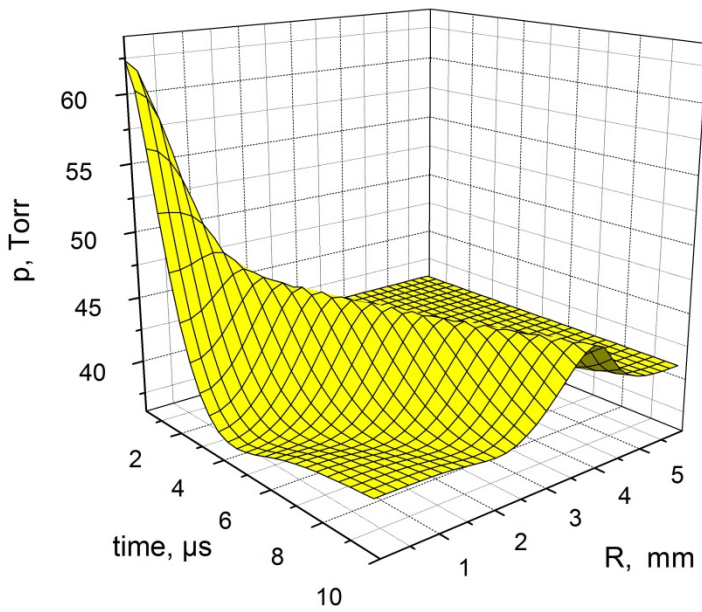


Figure III.12. Contour plot of pressure distribution after the main discharge pulse in air, plotted vs. time delay after the pulse and radial distance.

IV. Energy Balance in Nanosecond Pulse Discharges in Nitrogen and Air

IV.1. Introduction

Kinetics of vibrational and electronic energy transfer, temperature rise, and chemical reactions in nitrogen and air plasmas sustained by ns pulse discharges has been extensively studied over the last decade. Time-resolved measurements of temperature [134-138], absolute populations of excited electronic states of N₂ [135,136], absolute number densities of O atoms [135,136], N atoms and NO [139], and vibrational level populations of ground electronic state N₂ and O₂ [139-143], as well as detection of compression wave formation [144,145] in these discharges generated significant amount of data to provide insight into dominant energy transfer processes and chemical reactions in these highly nonequilibrium plasmas and afterglow. This insight makes possible effective use of ns pulse discharges for a number of applications, including high-speed flow control [146,147] (based on rapid energy thermalization in a discharge, on a time scale shorter than the acoustic time scale), plasma assisted combustion [148], and plasma biomedicine [149] (both based on efficient generation of excited species and chemically active radicals).

In spite of a growing body of experimental data, kinetic modeling of these discharges, incorporating state-specific energy transfer processes at high specific energy loading and in realistic geometry, is still under development. Recent work at Moscow State University [150,151], CNRS [152], Ecole Centrale Paris [152-154], Georgia Tech [155], Tohoku University [156], and Ohio State University [138,157] advanced this field considerably. However, modeling predictions of the experimental results, in particular of experiments with time-resolved measurements of temperature, pressure, vibrational level populations, and species number densities [140-143] require significant additional effort. The main objective of the present work is to use the kinetic model developed and validated in our previous work [138,157] to predict time-resolved N₂ vibrational level populations, temperature, and pressure during and after a single filament ns pulse discharge in nitrogen and air, compare the modeling prediction with experimental results [143,145], and determine energy balance in this type of the discharge.

IV.2. Experimental

The experiments modeled in the present work are discussed in detail in our previous publications [143,145]. Briefly, the experiments were done in a four-arm cross glass cell with quartz windows, with two spherical copper electrodes 7.5 mm in diameter and separated by a 10 mm gap placed in the cell, as shown in Fig. IV.1. A nanosecond pulse, diffuse filament discharge in 100 Torr of nitrogen or dry air was sustained between the electrodes by a custom-made pulsed plasma generator producing 10 kV peak voltage pulses ~100 nsec duration, at a low pulse repetition rate of v=50 Hz. The flow velocity in the cell, estimated from the flow rate, ~0.25 m/s, corresponds to flow residence time of approximately 20 ms, such that the flow in the cell experiences only ~1-2 discharge pulses. Typical voltage, current, and coupled energy waveforms in the discharge in air are shown in Fig. IV.2, both for the “main” discharge pulse and for the weak “after-pulse” discharge, produced by the plasma generator approximately 500 ns after the main pulse. The “after-pulse” is an artifact of the output of the custom-designed high-voltage pulse generator used in the present work. The main advantage of using this power supply compared to commercial pulse generators is high energy coupled per pulse, up to 15-20 mJ, which results in significant rapid heating and vibrational nonequilibrium at the present conditions. Discharge pulse waveforms in nitrogen are very similar to the ones for air. At these conditions, total energy coupled to the plasma is approximately 13 mJ/pulse in nitrogen and approximately 16 mJ in air. It can be seen that the main pulse couples approximately 90% of the energy to the plasma (see Fig. IV.2). Figure IV.3 shows single-shot ICCD images of the main pulse and of the after-pulse taken using a 100 ns camera gate, indicating partial contraction of the discharge filament during the after-pulse. In both images, the bottom electrode is grounded. The diameter of the filament generated during the main pulse is approximately 2.0 mm (FWHM of emission intensity radial distribution).

Time-resolved temperature and N₂(v=0-9) vibrational level populations in the discharge and in the afterglow (on the discharge filament centerline) were measured by picosecond broadband vibrational Coherent Anti-Stokes Raman Scattering (CARS) in BOXCARS phase matching geometry, with spatial resolution (interaction length in the direction of laser beams) of 0.5 mm [143]. Translational/rotational temperature was inferred from partially rotationally resolved vibrational CARS spectra (Q-branch of v=1→0 band) using CARSFIT synthetic spectrum code. Compression waves generated due to rapid heating of the gas in the discharge filament were detected using a custom-built phase-locked schlieren system [145]. These measurements are discussed in greater detail in the original papers [143,145].

IV.3. Kinetic model

The kinetic model used to study energy transfer in the nanosecond pulse discharge between the electrodes and in the afterglow, as well as the effect on the gas mixture in the cell is described in detail in our recent work [157,138]. Briefly, the discharge pulse is modeled using a one-dimensional axial model, with the coordinate axis directed along the filament centerline, and the afterglow is modeled using a one-dimensional radial axisymmetric model. The axial model incorporates Poisson equation for the axial electric field, Boltzmann equation for plasma electrons in two-term approximation including electron-electron collisions, equation for the electron temperature, time-dependent conservation equations for number densities of charged species (electrons, positive ions, and negative ions) and neutral species (including excited electronic states of N₂, O₂, N, and O), equations for relative populations of N₂ vibrational levels (“master equation”), and heavy species energy equation. The model used the experimental voltage waveform, such as shown in Fig. IV.2, as input. In the present work, kinetics of energy transfer during collisional quenching of excited electronic states of N₂ molecules and N atoms has been revised, to account for partial energy storage in the vibrational energy mode of the ground electronic state of N₂ [158]. Without this revision, the model would predict considerably more rapid temperature rise in the discharge and afterglow in nitrogen, at variance with the experimental results [143]. The list of quenching processes of N₂ and N species and their rate coefficients, used in the present model, is given in Table III.1. Note that according to a recent study [159], kinetics of energy transfer among excited vibrational and electronic levels of nitrogen molecules may be strongly coupled to vibrational excitation of nitrogen molecules in the metastable A^{3Σ_u⁺ state. However, incorporating vibrationally excited molecules N₂(A^{3Σ_u⁺,v) into the kinetic model would require knowledge of a significant number of state-specific vibrational / electronic energy transfer rates, which are not available.}}

Table III.1.

	Process	Rate coefficient, cm ³ /s	Energy defect, eV	Ref.
R1	N ₂ (A ^{3Σ_u⁺) + N₂(A^{3Σ_u⁺) → N₂(B^{3Π_g) + N₂(X^{1Σ_g⁺,v=12)}}}}	7.7·10 ⁻¹¹	1.76	[158]
R2	N ₂ (A ^{3Σ_u⁺) + N₂(A^{3Σ_u⁺) → N₂(C^{3Π_u) + N₂(X^{1Σ_g⁺,v=4)}}}}	1.5·10 ⁻¹⁰	0.18	[158]
R3	N ₂ (A ^{3Σ_u⁺) + N(^{4S}) → N₂(X^{1Σ_g⁺,6≤v≤9) + N(^{2P})}}	4.4·10 ⁻¹¹	0.91-0.12	[160]
R4	N ₂ (a' ^{1Σ_u⁻) + N₂ → N₂(B^{3Π_g) + N₂}}	1.9·10 ⁻¹³	0.24	[159]
R5	N ₂ (a' ^{1Π_g) + N₂ → N₂(a'^{1Σ_u⁻) + N₂}}	2·10 ⁻¹¹	0.15	[159]
R6	N ₂ (w ^{1Δ_u) + N₂ → N₂(a'^{1Π_g) + N₂}}	10 ⁻¹¹	0.34	[159]
R7	N ₂ (a'' ^{1Σ_g⁺) + N₂ → N₂(a'^{1Π_g) + N₂}}	3·10 ⁻¹³	3.7	[159]

R8	$N(^4S) + N(^4S) + N_2 \rightarrow N_2(B^3\Pi_g) + N_2$	$8.27 \cdot 10^{-34} \cdot \exp(500/T)$	2.44	[159]
R9	$N(^2D) + N_2 \rightarrow N(^4S) + N_2$	$4.52 \cdot 10^{-14} \cdot T^{0.68} \cdot \exp(-1438/T)$	2.8	[161]
R10	$N(^2P) + N(^4S) \rightarrow N(^4S) + N(^2D)$	$6 \cdot 10^{-13}$	1.2	[158]
R11	$N(^2P) + N(^4S) \rightarrow N(^4S) + N(^4S)$	$1.8 \cdot 10^{-12}$	3.58	[158]
R12	$N(^2P) + N_2 \rightarrow N(^4S) + N_2$	$3 \cdot 10^{-17}$	3.58	[160]
R13	$N_2(B^3\Pi_g) + N_2 \rightarrow N_2(A^3\Sigma_u^+) + N_2(X^1\Sigma_g^+, v=4)$	$2.85 \cdot 10^{-11}$	0.86	[158]
R14	$N_2(W^3\Delta_u) + N_2 \rightarrow N_2(A^3\Sigma_u^+) + N_2(X^1\Sigma_g^+, v=4)$	$2.85 \cdot 10^{-11}$	0.06	[158]
R15	$N_2(B^3\Sigma_u^-) + N_2 \rightarrow N_2(A^3\Sigma_u^+) + N_2(X^1\Sigma_g^+, v=7)$	$2.85 \cdot 10^{-11}$	0.04	[158]
R16	$N_2(B^3\Pi_g) + N_2 \rightarrow N_2(X^1\Sigma_g^+) + N_2$	$1.5 \cdot 10^{-12}$	7.35	[158]
R17	$N_2(W^3\Delta_u) + N_2 \rightarrow N_2(X^1\Sigma_g^+) + N_2$	$1.5 \cdot 10^{-12}$	7.36	[158]
R18	$N_2(B^3\Sigma_u^-) + N_2 \rightarrow N_2(X^1\Sigma_g^+) + N_2$	$1.5 \cdot 10^{-12}$	8.16	[158]
R19	$N_2(C^3\Pi_u) + N_2 \rightarrow N_2(B^3\Pi_g) + N_2(X^1\Sigma_g^+, v=13)$	$3.85 \cdot 10^{-12}$	0.21	[158]
R20	$N_2(E^3\Sigma_g^+) + N_2 \rightarrow N_2(B^3\Pi_g) + N_2(X^1\Sigma_g^+, v=17)$	$3.85 \cdot 10^{-12}$	0.11	[158]

The initial radial distributions of species number densities at the end of the discharge pulse (when the applied voltage falls to zero, at $t=100$ ns), used by the radial model, are assumed to follow experimental broadband plasma emission intensity halfway between the electrodes, approximated as a Gaussian distribution with FWHM of 2.0 mm. The radial model incorporates time-dependent compressible Navier-Stokes equations for conservation of mass, momentum, energy, species concentrations, and master equation for N_2 vibrational level populations [138]. Both Poisson equation and Boltzmann equation are disabled during the afterglow. The main objective of the radial model is to predict evolution of temperature and pressure in the discharge filament, controlled by rapid heating in the plasma (on the time scale shorter than the acoustic time scale), and propagation of a resultant compression wave in the radial direction. The modeling calculations were carried out in nitrogen and dry air, at $P=100$ Torr.

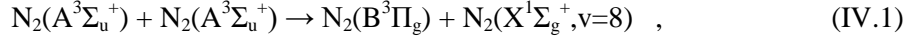
The use of the present approach is justified in the entire discharge gap, except in the cathode layer region, where the compression wave becomes non-one-dimensional [145]. The present approach offers a low computational cost alternative to two-dimensional models of transient high-pressure nonequilibrium electric discharges in compressible molecular gases. The present model is considerably more accurate compared to a zero-dimensional kinetic model used in Ref. [143], where electric field and electron density in the plasma were estimated from experimental voltage and current waveforms.

IV.4. Results and Discussion

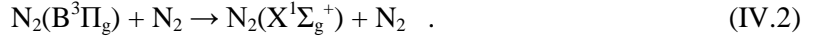
Figure IV.2, which plots experimental discharge voltage, current, and coupled energy waveforms for the main pulse and the after-pulse in air, also shows predicted current pulse waveforms, illustrating good agreement between the model predictions and the data. As in our previous work [138], current density predicted by the one-dimensional axial model was multiplied by the discharge filament cross sectional area based on the FWHM diameter inferred from the radial distribution of plasma emission halfway between the electrodes (see Fig. IV.3), 2.0 mm and 0.67 mm, respectively. Since peak voltage and current during the after-pulse are significantly lower compared to the main pulse (see Fig. IV.2), energy coupling to the plasma during the after-pulse is also much lower, 1.15 mJ vs. 13.3 mJ. However,

specific energy loading during the after-pulse may be fairly significant since it occurs in a partially constricted discharge filament (see Fig. IV.3).

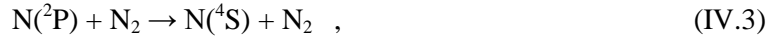
Figure IV.4(a) compares experimental and predicted temperature during and after the discharge pulse in nitrogen, plotted together with predicted rates of energy dissipation in different energy transfer processes. In Fig. IV.4, $t=0$ corresponds to the beginning of the main pulse current rise. It can be seen that on sub- μ s time scale, up to $t \approx 2 \mu\text{s}$, the two dominant processes controlling temperature rise in the discharge and in the afterglow are the energy pooling reaction, R1



and quenching of the $\text{B}^3\Pi$ state of N_2 to the ground electronic state, reaction R16



These two processes are mainly responsible for the “rapid” temperature rise in the plasma on sub-acoustic time scale, $t < \tau_{\text{acoustic}} = r/a \sim 3 \mu\text{s}$, where $r \approx 1 \text{ mm}$ is the filament radius and $a \approx 350 \text{ m/s}$ is the speed of sound. On a longer time scale, $t \sim 3-30 \mu\text{s}$, quenching of metastable N atoms,



(reactions R12 and R9) also contribute significantly to the “slow” temperature rise, $t > \tau_{\text{acoustic}}$.

Figure IV.4(b) compares temperature rise in nitrogen predicted by the model with the experimental data, using three different assumptions. Line 1 shows temperature rise predicted by the baseline model, using reactions listed in Table III.1. It can be seen that temperature reaches $T \approx 500 \text{ K}$ at $t=100 \mu\text{s}$, very close to the experimental value. However, temperature rise predicted on a shorter time scale, $t \sim 1-10 \mu\text{s}$, is noticeably slower compared to the data. Line 2 shows temperature growth predicted by the model assuming that all energy defect in reactions R1 and R2 is thermalized, instead of being stored in the vibrational mode of the ground electronic state of nitrogen, $\text{N}_2(\text{X}^1\Sigma_g^+, v)$. In this case, temperature rise on the short time scale, $t \sim 0.1-1 \mu\text{s}$, is much faster compared to the data, illustrating that not accounting for ground state vibrational excitation during $\text{N}_2(\text{A}^3\Sigma_u^+)$ energy pooling reactions results in significant overprediction of “rapid” temperature rise in the plasma on sub-microsecond time scale, by approximately a factor of two. Note that since quenching of excited electronic states of N_2 occurs on sub-microsecond time scale at the present conditions, it cannot be the mechanism of significant temperature rise at $t \sim 1-10 \mu\text{s}$, detected in the experiment and underpredicted by the baseline model (line 1). However, from Fig. IV.4(a), it is evident that quenching of electronically excited N atoms (e.g. reaction R9) does occur on the right time scale, and is therefore the most likely kinetic mechanism responsible for the temperature rise at this stage. Electronically excited atoms, $\text{N}^2(\text{P})$ and $\text{N}^2(\text{D})$, may well be generated by electron impact during the discharge pulse. However, to the best of our knowledge, experimental cross sections for these processes are not available. To estimate the effect of excited N atoms on temperature rise at $t \sim 1-10 \mu\text{s}$, we assumed that 20% of nitrogen atoms produced during the discharge are generated in $\text{N}^2(\text{D})$ state. Line 3 in Fig. IV.4(b) plots temperature evolution predicted by the model using this assumption. Indeed, it can be seen that in this case the model predictions are closer to the experimental data, suggesting that temperature rise in nitrogen afterglow on microsecond time scale is controlled by quenching of excited nitrogen atoms produced by the discharge.

Figure IV.5 plots experimental and predicted vibrational level populations of the ground electronic state of nitrogen, $\text{N}_2(\text{X}^1\Sigma_g^+, v)$, at different delay times after the beginning of the main discharge pulse ($t=0.1-500 \mu\text{s}$). As detected in several previous studies [162,163,140], the slope of the distribution function for $v=0,1$ is much greater compared to $v=2-8$, indicating that the “first level” N_2 vibrational temperature, $T_{0,1} = \frac{E_{01}}{\ln(n_0/n_1)}$, where E_{01} is the energy difference between vibrational levels $v=1$ and

$v=0$, and n_1 and n_0 are their populations, is much less compared to $T_{0,v}$ ($v=2-8$). This effect, reproduced by the model, is due to the fact that the electron temperature in the pulsed discharge exceeds considerably the vibrational mode temperature. Therefore electron impact produces vibrational level populations $v>1$ with the slope close to the electron temperature, much higher than the “first level” vibrational temperature. A secondary “kink” in the predicted vibrational distributions in Fig. IV.5, at $v=4$, is due to vibrational excitation of the ground electronic state in energy pooling reaction R2 (see Table III.1), since the present model assumes that only these two vibrational levels are populated during these processes.

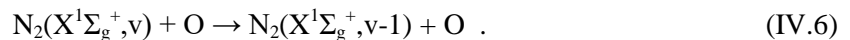
Figure IV.6, which plots experimental and predicted $N_2(X^1\Sigma_g^+, v=0-9)$ populations vs. time shows that the model underpredicts significant transient rise of vibrational level populations on a $\sim 1-10 \mu\text{s}$ time scale. In our previous work [143], as well as in earlier work [162], it was suggested that this rise may be caused by significant ground state vibrational excitation in energy pooling processes, such as reactions R1 and R2. The present more accurate model predictions, however, show that this effect appears to be insufficient to interpret the data. Moreover, incorporating relatively modest energy addition by the after-pulse discharge (about 8.5% of the main discharge pulse, see Fig. IV.2) into the model suggests that it may in fact produce noticeable additional vibrational excitation of the plasma, as illustrated in Fig. IV.7. Indeed, adding the after-pulse discharge filament with the diameter of 0.67 mm, generated at $t=500 \text{ ns}$, results in a significant jump of predicted vibrational level populations, such that they match their peak values measured in the afterglow (see Fig. IV.7). This occurs for two reasons, (i) smaller diameter of the partially constricted after-pulse filament compared to the main discharge pulse filament, producing higher specific energy loading, and (ii) considerably lower reduced electric field in the after-pulse discharge, resulting in higher discharge energy fraction going to vibrational excitation of ground electronic state N_2 . Note, however, that the experimental results exhibit a gradual rise in vibrational level populations (see Fig. IV.7), rather than a sudden jump. This apparent discrepancy may be resolved by noticing that due to the small diameter of the after-pulse discharge filament, it may be not very reproducible pulse-to-pulse, and may well miss the laser beams for some laser shots during CARS signal accumulation, thus resulting in a more gradual signal rise. This possible artifact is discussed in greater detail at the end of Section IV.3.

As shown in Fig. IV.8, temperature rise in the plasma on sub-microsecond time scale results in a noticeable pressure overshoot on the filament centerline, predicted by the model, by approximately 30%. Since the pressure rise occurs on sub-acoustic time scale, it generates a radial compression wave, which has been detected in nitrogen in our previous work [145].

In air, kinetics of energy thermalization and temperature rise during and after the discharge pulse becomes somewhat more complicated, as shown in Fig. IV.9. In this case, temperature in the plasma exhibits a well-pronounced two-stage rise, “rapid” (sub-acoustic) heating on sub- μs time scale, and “slow” heating on $\sim 50-500 \mu\text{s}$ time scale. Kinetics of these two heating stages is discussed in detail in our previous work [138]. Basically, rapid heating occurs mainly in collisions of electronically excited nitrogen molecules with O_2 , resulting in oxygen dissociation,



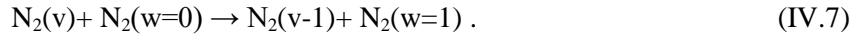
Figure IV.9 shows that rapid temperature rise during and after the discharge pulse occurs on the same time scale as quenching of excited electronic states of nitrogen molecules by O_2 , a few hundred nanoseconds. Gasdynamic expansion of the plasma filament, caused by its heating on sub-acoustic time scale, results in transient temperature reduction and O atom number density decrease, predicted by the model (see Fig. IV.9). Slow heating occurs during vibration-translation (V-T) relaxation of vibrationally excited N_2 by O atoms,



The time scale for the slow heating can be estimated from the net rate of V-T relaxation of nitrogen by O atoms, as was done in our previous work [138]. After peaking at $T \approx 850 \text{ K}$, on the time scale of approximately $500 \mu\text{s}$, the temperature decreases to near room temperature over about 10 ms due to radial

diffusion, consistent with the model predictions (see Fig. IV.9).

Comparing the behavior of gas temperature with “first level” N_2 vibrational temperature, $T_{0,1}$, plotted in Fig. IV.10, it can be seen that the “slow” temperature rise begins at the same time when the vibrational temperature starts to decrease. N_2 vibrational temperature, which increases considerably during the main discharge pulse due to vibrational excitation by electron impact, continues to rise during the afterglow, on the time scale of a few tens of microseconds after the pulse, peaking at $T_{0,1} \approx 2900$ K, in good agreement with the model predictions (see Fig. IV.10). This effect, as discussed in greater detail in our previous work [138], is due to “downward” V-V transfer in nitrogen with vibrational levels $v \geq 2$, strongly overpopulated by electron impact during the discharge,



This process is illustrated further in Fig. IV.11, which compares experimental and predicted $N_2(v=0-8)$ vibrational level populations at different time delays after the discharge pulse. It can be seen that a “kink” in the vibrational distribution function at $v=1$, generated during the discharge, gradually disappears at longer delay times, before V-T relaxation by O atoms reduces high vibrational level populations. Comparing Fig. IV.5 and Fig. IV.11, it is apparent that the “straightening” of the vibrational distribution caused by the downward V-V energy transfer of Eq. (IV.7) occurs in a similar way both in N_2 and air, as expected. On the other hand, V-T relaxation in air occurs much faster compared to nitrogen, due to rapid relaxation by O atoms. Figure IV.12, which plots N_2 vibrational level populations vs. time, also illustrates transient rise of $N_2(v=0-4)$ populations after the discharge pulse due to this effect, in good agreement with the modeling predictions. Incorporating energy addition by a weak after-pulse shown in Fig. IV.3 results in additional vibrational excitation of the plasma, although this effect is not as pronounced as in nitrogen (see Fig. IV.7). The difference between air and nitrogen is mainly due to a somewhat higher reduced electric field in the after-pulse plasma filament in air, compared to nitrogen, which reduces energy fraction into vibrational excitation of N_2 in the after-pulse.

Returning to discussion of temperature rise kinetics in air plasma, Fig. IV.13 shows that, as expected, “rapid” near constant volume heating on sub-acoustic time scale, $t < \tau_{\text{acoustic}} \sim 3 \mu\text{s}$, results in a significant pressure overshoot in the discharge filament, by about 60%. The pressure rise is considerably more pronounced than in nitrogen (see Fig. IV.8), due to higher rate of temperature rise in air, by approximately a factor of 2 ($\Delta T \approx 200$ K over 1 μs). After the overshoot, the discharge filament begins to expand and a compression wave propagates in the radial direction (see Fig. IV.14), causing rapid pressure fall on the centerline and slight transient rarefaction to $P \approx 90$ Torr, before returning to baseline pressure.

Figure IV.15 compares time-resolved locations of the radial compression wave, obtained from phase-locked schlieren images in our previous work [145], with the wave front location predicted by the present model (defined as the location of density gradient maximum). In the experiment, wave locations were determined from schlieren frames taken after the discharge pulse 1 μs apart ($t=0$ corresponds to the beginning of the main discharge pulse). It can be seen that the compression wave speed measured in the experiment is significantly higher compared to the model predictions. Average wave speed, determined as a slope to the trajectory at $r=4-10$ mm, is 500 m/s in the experiment vs. 360 m/s in the calculations. This discrepancy cannot be explained by preheating of the gas by previous discharge pulses (e.g. see Fig. IV.13, which shows that the temperature on the filament centerline in the beginning of the discharge pulse only slightly exceeds the room temperature, by ~20-30 K). Variation of the discharge filament diameter by $\pm 20\%$, which may be caused by the filament “jitter” (transverse movement pulse-to-pulse) affected the wave speed only insignificantly, approximately by 5%. It is possible that the wave speed may be affected by interaction of the cylindrical compression wave generated by the discharge filament and the spherical compression wave originated in the cathode layer of the discharge [145], but verifying this conjecture requires exercising a two-dimensional axisymmetric discharge / afterglow model.

The present kinetic model has also been used to analyze one of the puzzling results of experiments [143], which suggested that the total number of vibrational quanta per N_2 molecule continues

increasing after the discharge pulse (on the time scale of \sim 1-100 μ s), both in nitrogen and in air. In nitrogen, this effect, also detected in previous CARS measurements in a pulsed DC discharge in N₂ [162], may be interpreted as energy addition to the ground state vibrational model during collisional quenching of excited electronic states [162,143]. However, in air this explanation becomes far less likely since electronically excited levels of nitrogen in air are quenched on a much shorter time scale, \sim 1 μ s (see Fig. IV.9). The results of the present work suggest that this effect may be caused by a combination of discharge filament jitter and gasdynamic expansion caused by rapid heating. This effect is illustrated qualitatively in Fig. IV.16. Basically, transverse motion of the filament (in the direction perpendicular to the laser beams) results in a reduction of the CARS signal generated when the filament is displaced laterally, such that the laser beams probe its less excited, peripheral region (see Fig. IV.16(a)). This effect is more pronounced at short delays after the discharge pulse, when gasdynamic expansion has not yet occurred, and the filament diameter is relatively small. However, as the filament expands and its diameter increases, the effect of its lateral movement on the CARS signal intensity would be less pronounced, since now the laser beams are predominantly probing a stronger excited near-axial region of the filament (see Fig. IV.16(b)). This effect would be interpreted as a rise of high vibrational level populations at long time delays after the discharge pulse, i.e. an apparent increase of the number of vibrational quanta per N₂ molecule. Lateral jitter of the main discharge filament may also cause the partially constricted after-pulse filament to miss the laser beams, as discussed above.

To estimate the significance of this effect on the number of quanta per molecule at the present conditions, the filament jitter was modeled as random transverse motion of the region “probed” by the laser (with the amplitude of 0.2 mm), sampling N₂ vibrational level populations at different radial locations of the filament, and averaging the results for different delay times after the discharge pulse. The results of this semi-qualitative estimate are shown in Fig. IV.17. It can be seen that random radial jitter of the expanding filament results in an apparent rise of vibrational quanta per N₂ molecule by \sim 20% on the time scale of \sim 5 μ s, close to the experimental result of \sim 30% increase on the same time scale [143]. This result suggests that the effect of apparent rise of vibrational quanta per molecule is caused by the jitter and gasdynamic expansion of the filament, rather than by collisional energy transfer among different molecular energy modes.

At the present conditions, discharge energy fraction coupled to the positive column of the discharge filament in air is approximately 50%, with the rest coupled to the cathode layer. Significant energy coupling to the cathode layer of the discharge is apparent from schlieren images taken in the afterglow, which indicate an additional compression wave originating from the surface of the cathode [145]. This demonstrates the importance of self-consistent modeling of the cathode layer of the discharge, in 2-D geometry, for realistic prediction of the amplitude and shape of pressure perturbations produced by the discharge pulse. By the end of the discharge pulse in air, at t=100 ns, approximately 50% of the energy coupled to the positive column is stored in the vibrational mode of ground electronic state N₂, 25% remains in electronically excited N₂^{*}, 15% goes to O₂ dissociation (both by electron impact and by quenching of N₂^{*}), and 10% is thermalized during N₂^{*} quenching by O₂. These energy fractions represent 25%, 12.5%, 7.5%, and 5% of the total discharge pulse energy, respectively. By the end of the pressure overshoot (i.e. before gasdynamic expansion), at t=1 μ s, positive column energy fractions stored in N₂ vibrational and electronic energy modes are 50% and 2-3% (i.e. 25% and 1-2% of the total pulse energy), respectively, energy fraction stored in O atoms remains about 15% (7.5% of the total pulse energy), and thermalized energy increases to 20% (10% of the total pulse energy). Finally, energy stored in N₂ vibrational mode and O atoms is thermalized on the long time scale, t \sim 50-500 μ s, without producing finite amplitude compression waves, and diffuses out of the filament. Thus, it can be seen that at the present conditions, about 7.5% of the total discharge pulse energy is spent on O atom generation, and only about 10% is thermalized on sub-acoustic time scale.

IV.5. Summary

In the present work, kinetic modeling is used to analyze energy partition and energy transfer in nanosecond pulse discharges in air and nitrogen. The modeling predictions are compared with time-resolved temperature and $N_2(v=0-9)$ vibrational population measurements by picosecond broadband Coherent Anti-Stokes Raman Spectroscopy (CARS) [143] and phase-locked schlieren images of a compression wave generated due to heating of the discharge filament on sub-acoustic time scale [145]. The present kinetic model has been previously validated using time-resolved measurements of $N_2(v=0-4)$ vibrational level populations, [N], [O], and [NO] in nanosecond pulse discharge in air at a lower specific energy loading [139], as well as time- and spatially resolved temperature measurements in nanosecond pulse discharges in air and H_2 -air at a lower pressure [138].

In the experiments [143,145] modeled in the present work, the diffuse filament, nanosecond pulse discharge (pulse duration ~ 100 ns) was sustained between two spherical electrodes at $P=100$ torr and operated at a low pulse repetition rate, 50 Hz, to enable rotational-translational temperature and N_2 vibrational level population measurements over a wide range of time scales after the discharge pulse, from tens of ns to tens of ms. The present analysis is based on a one-dimensional axial model for the discharge pulse, and a one-dimensional radial axisymmetric model for the afterglow. The model shows good agreement with the experimental data, reproducing experimental discharge current pulse waveforms, as well as dominant processes of energy partition and energy transfer in the discharge and the afterglow. Specifically, the results demonstrate that energy thermalization and temperature rise occurs in two stages, (i) “rapid” heating, occurring on the time scale $\tau_{\text{rapid}} \sim 0.1\text{-}3 \mu\text{s}$ (in nitrogen) and $\tau_{\text{rapid}} \sim 0.1\text{-}1 \mu\text{s}$ (in air), dominated by $N_2(A^3\Sigma_u^+)$ energy pooling processes, $N_2(B^3\Pi_g)$ and $N(^2P, ^2D)$ quenching (in nitrogen), and by quenching of multiple excited electronic states of N_2 molecules by O_2 (in air), and (ii) “slow” heating, on the time scale $\tau_{\text{slow}} \sim 50\text{-}500 \mu\text{s}$, caused primarily by N_2 vibrational relaxation by O atoms (in air), and nearly completely missing in nitrogen due to the much slower vibrational relaxation rate. The results in air are consistent with our previous work [138].

Comparison of the model predictions with high spatial resolution measurements of $N_2(v=0-9)$ vibrational level populations confirms the conclusions of our previous work [157,138], which suggested that N_2 “first level” vibrational temperature rise after the discharge pulse is caused by the “downward” vibrational-vibrational exchange depopulating higher vibrational levels and populating vibrational level $v=1$. The model accurately reproduces temporal dynamics of vibrational level populations and temperature in the discharge and the afterglow. Thus, the present work provides experimental validation of the modeling predictions, based on accurate time-resolved temperature and $N_2(v=0-9)$ population measurements. Rapid heating of the filament on sub-acoustic time scale produces a strong compression wave propagating in the radial direction, predicted by the present kinetic model and detected in previous experiments in nanosecond pulse filament discharges [144,145]. The experimental wave speed is considerably higher compared to the model predictions, by approximately 30%. The reason for this discrepancy is not fully understood, and may be due to interaction between the cylindrical and spherical compression waves generated by the discharge filament and the cathode layer, respectively.

Since current in the cathode layer is dominated by the ion current, nearly all energy coupled to the cathode layer is thermalized extremely rapidly in ion-neutral collisions, both elastic and charge transfer. This occurs on the time scale of discharge pulse duration, ~ 100 ns, resulting in rapid temperature and pressure increase in the cathode layer. However, since the present one-dimensional model does not account for a significantly larger surface area occupied by the cathode layer on the electrode, compared to the discharge filament cross sectional area (see Fig. IV.3), peak temperature and pressure values in the cathode layer predicted by the model may well be overpredicted. Predictive analysis of cathode layer kinetics requires the use of a full two-dimensional model of the discharge.

Parametric modeling calculations for different voltage pulse waveforms demonstrated that, as expected, discharge energy fraction going into electronic excitation of nitrogen molecules increases with

pulse peak voltage and decreases with voltage rise time. Basically, this suggests that increasing the discharge energy fraction thermalized during “rapid heating” requires the use of short rise time, high peak voltage pulses. Similarly, since the dominant “rapid heating” process of Eq. (IV.5) in air results in effective generation of O atoms, similar pulse waveforms (i.e. short rise time, high peak voltage) are likely to be more effective for plasma assisted combustion applications. Finally, the effect of “slow heating” driven by vibrational relaxation on flow perturbations is not fully understood, and further experiments in near-surface nanosecond pulse discharges are necessary to provide quantitative insight into this issue.

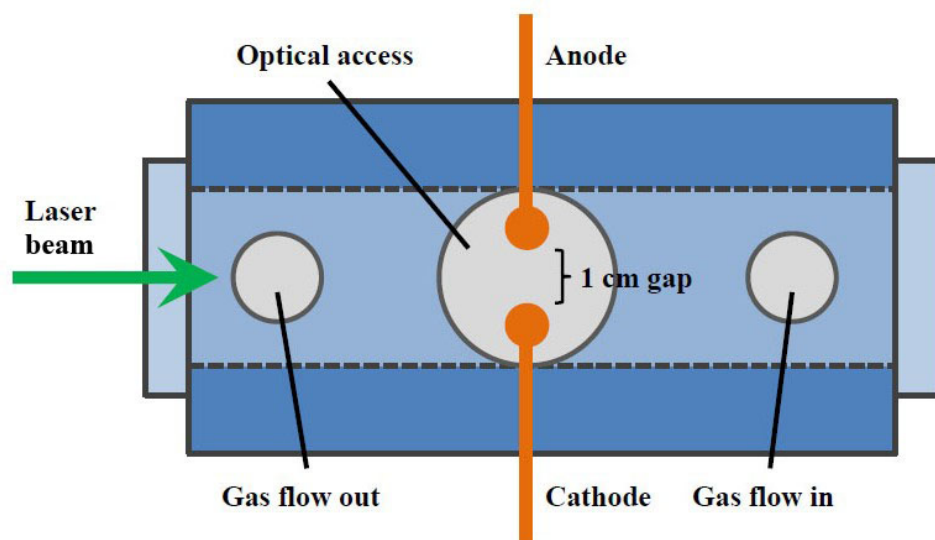


Figure IV.1. Photograph and schematic of the discharge cell.

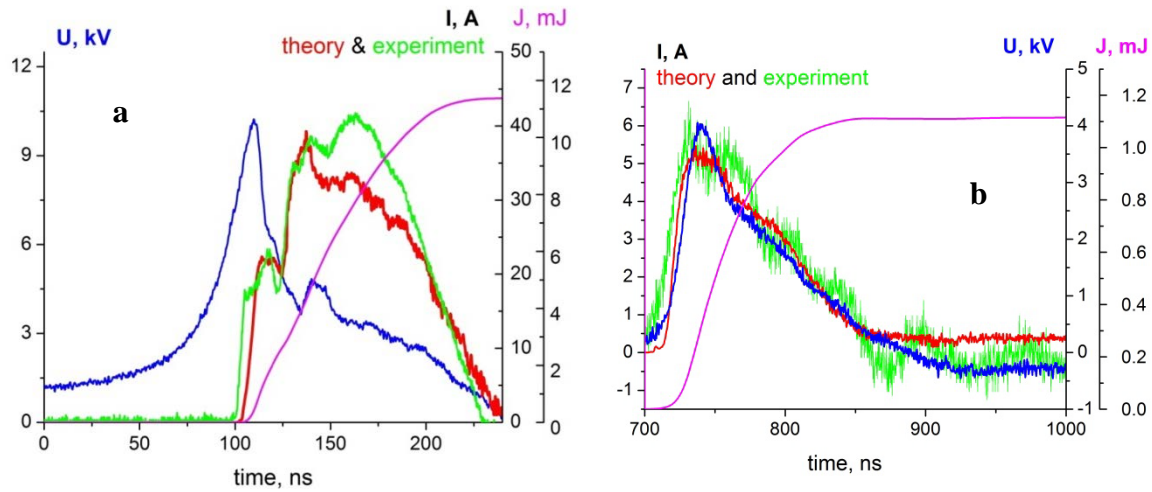


Figure IV.2. Voltage (experimental), current (experimental and predicted), and coupled energy (predicted) waveforms during the main pulse (a) and during the “after-pulse” (b) in air at $P=100$ Torr.

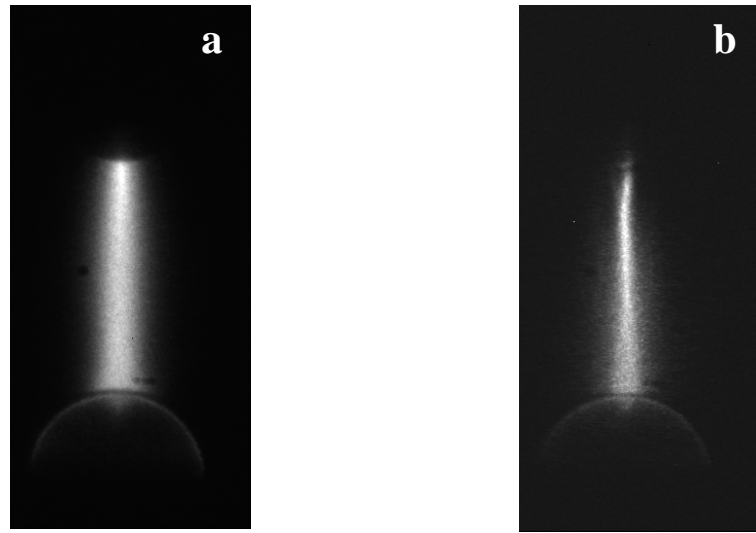


Figure IV.3. ICCD images of plasmas generated in air during the main pulse (a) and during the “after-pulse” 500 ns later (b). $P=100$ Torr, camera gate 100 ns, bottom electrode is grounded.

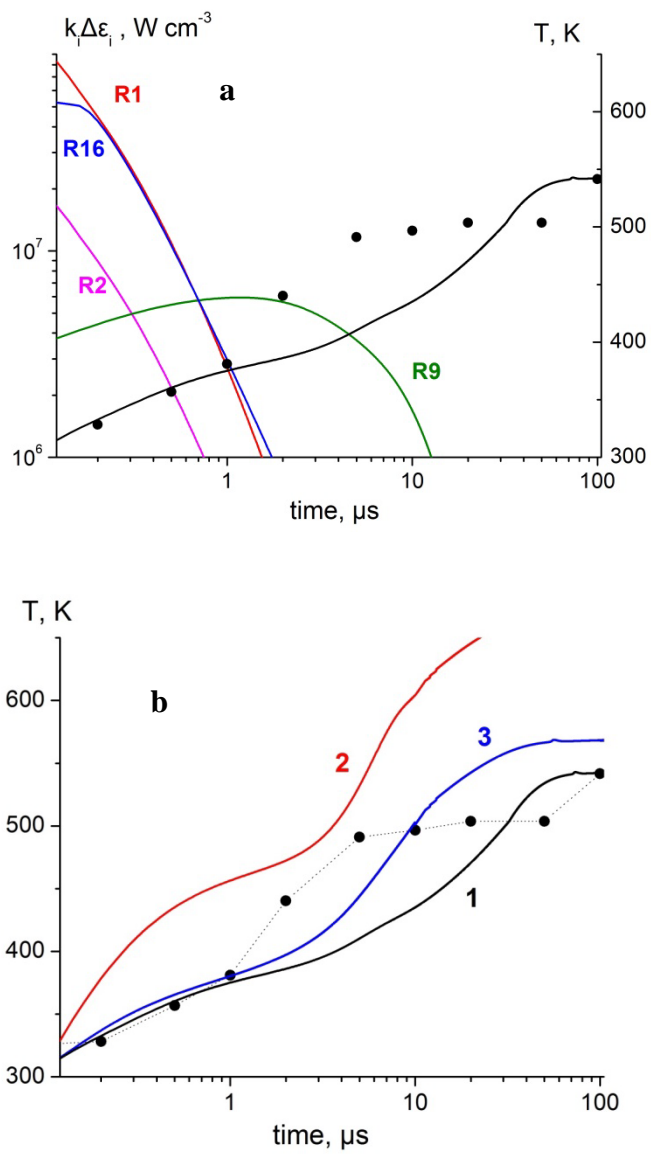


Figure IV.4. (a) Time-resolved gas temperature during and after the discharge pulse in nitrogen predicted by the model, plotted together with predicted rates of energy dissipation in dominant energy transfer processes; (b) Comparison of model predictions with experimental data using three different assumptions (see details in the text). Symbols: experimental data, lines: model predictions.

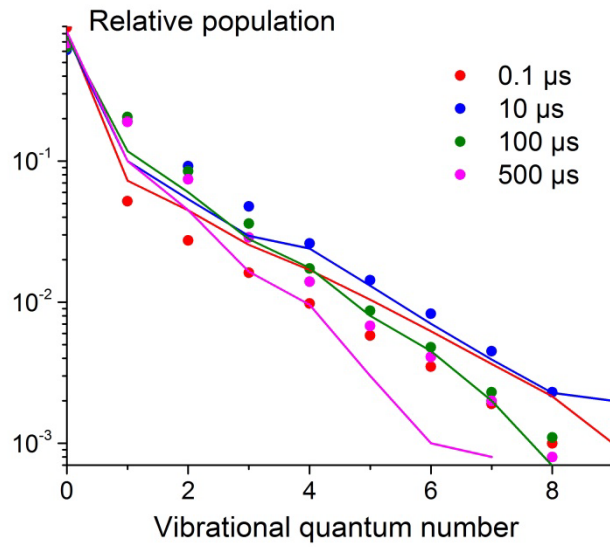


Figure IV.5. Experimental and predicted N_2 vibrational distribution functions after the discharge pulse in nitrogen, at different delay times after beginning of the main pulse. Symbols: experimental data, lines: model predictions.

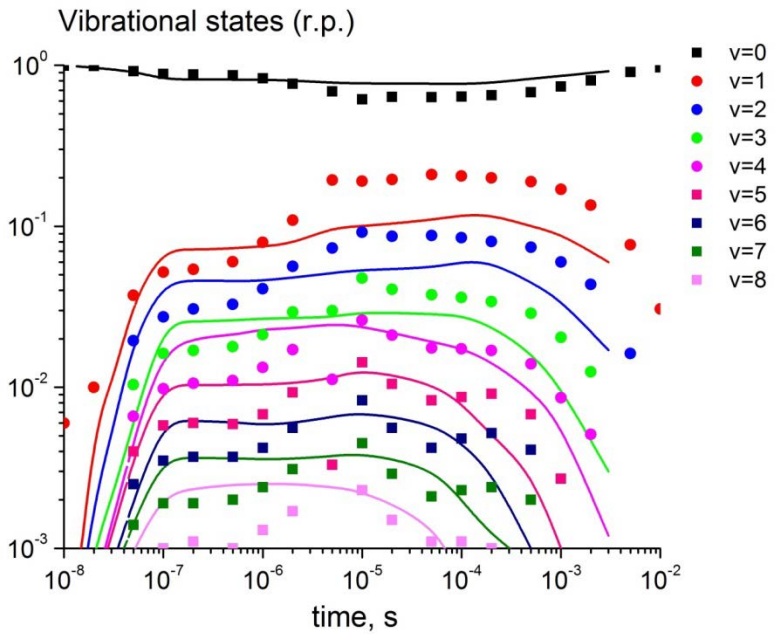


Figure IV.6. Experimental and predicted $\text{N}_2(v=0-9)$ vibrational level populations, plotted vs. time after beginning of the main discharge pulse in nitrogen. Symbols: experimental data, lines: model predictions.

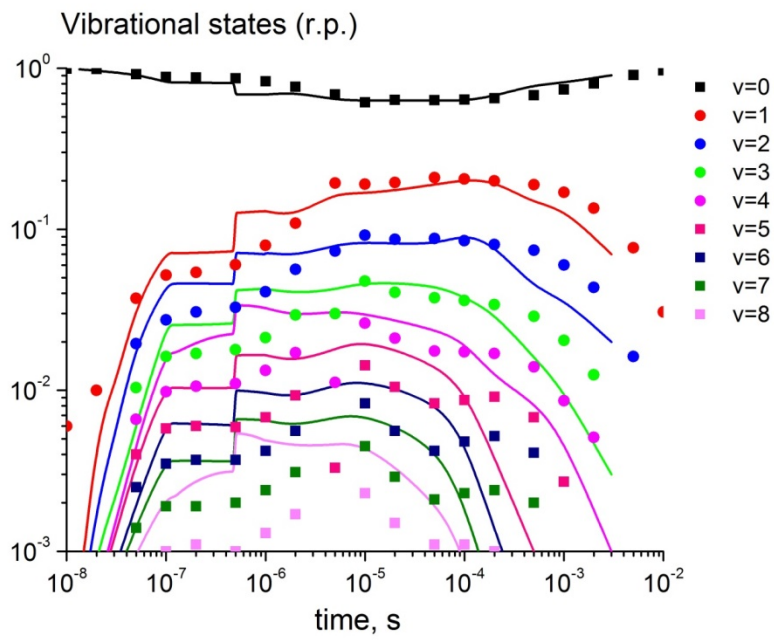


Figure IV.7. Experimental and predicted $\text{N}_2(v=0-9)$ vibrational level populations, plotted vs. time after beginning of the main discharge pulse in nitrogen, with additional energy loading by the after-pulse at $t=500$ ns taken into account. Symbols: experimental data, lines: model predictions.

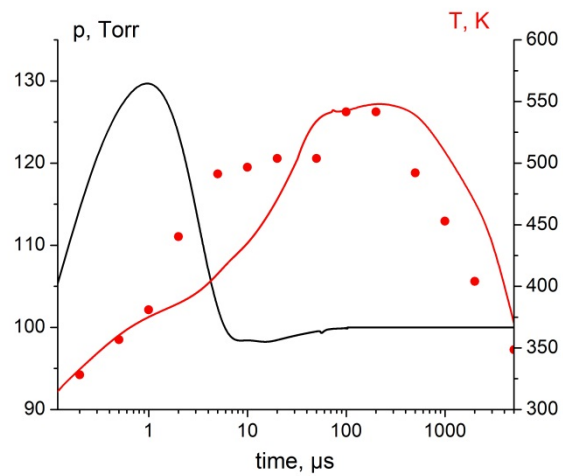


Figure IV.8. Time-resolved gas temperature (experimental and predicted) and pressure predicted on filament centerline during and after the discharge pulse in nitrogen. Symbols: experimental data, lines: model predictions.

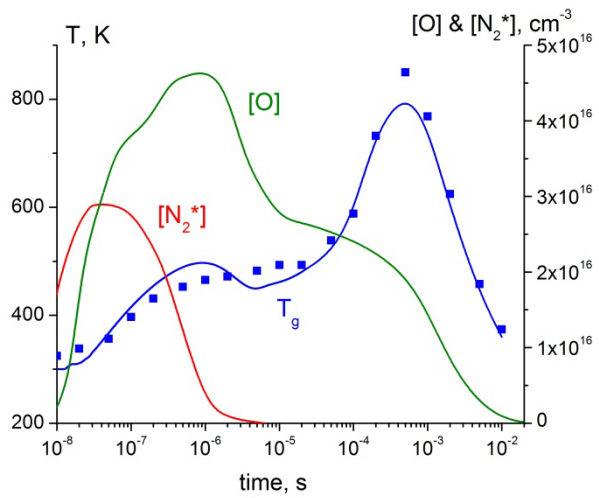


Figure IV.9. Time-resolved gas temperature (experimental and predicted), predicted number density of O atoms, and total number density of electronically excited states of N_2 and during and after the discharge pulse in air. Symbols: experimental data, lines: model predictions.

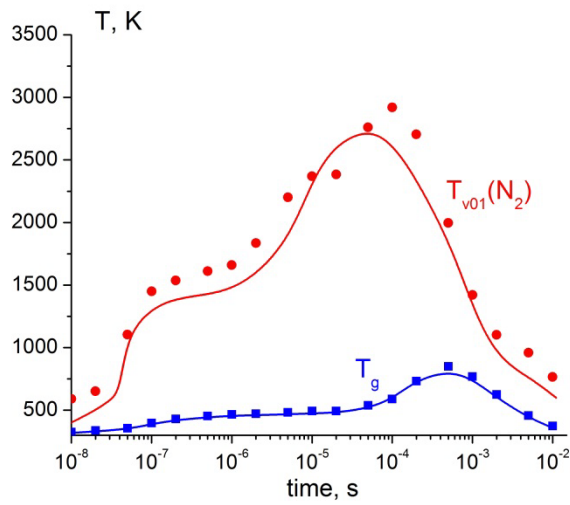


Figure IV.10. Experimental and predicted time-resolved gas temperature and “first level” N_2 vibrational temperature during and after the discharge pulse in air. Symbols: experimental data, lines: model predictions.

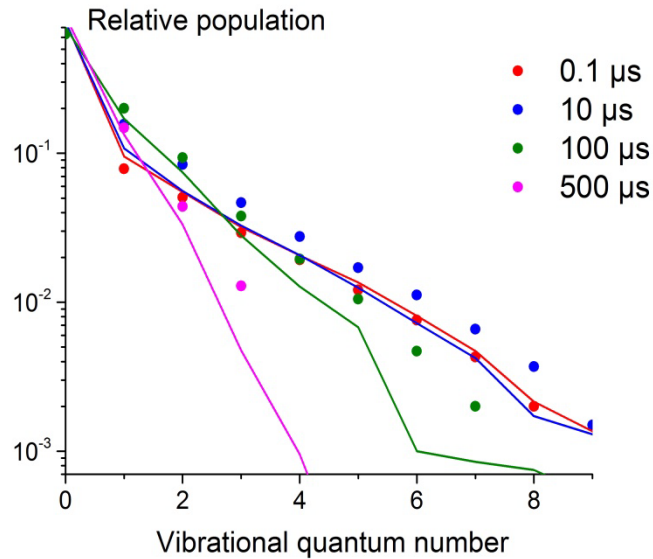


Figure IV.11. Experimental and predicted N_2 vibrational distribution functions after the discharge pulse in air, at different delay times after beginning of the main pulse. Symbols: experimental data, lines: model predictions.

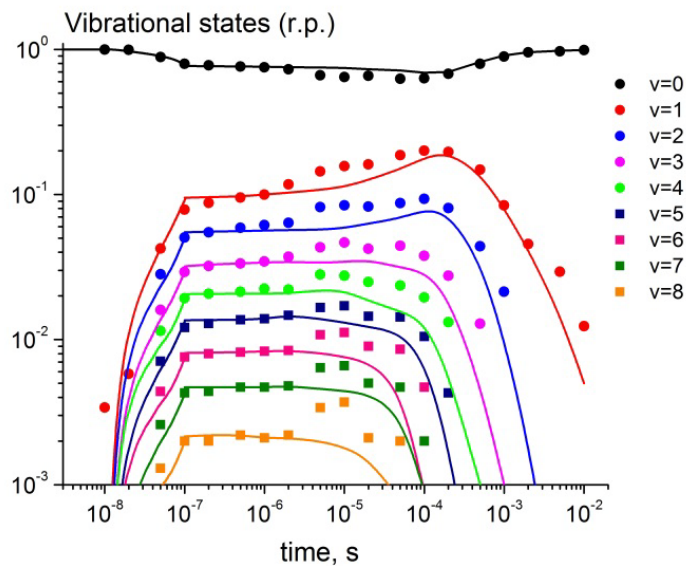


Figure IV.12. Experimental and predicted $\text{N}_2(v=0-9)$ vibrational level populations, plotted vs. time after beginning of the main discharge pulse in air. Symbols: experimental data, lines: model predictions.

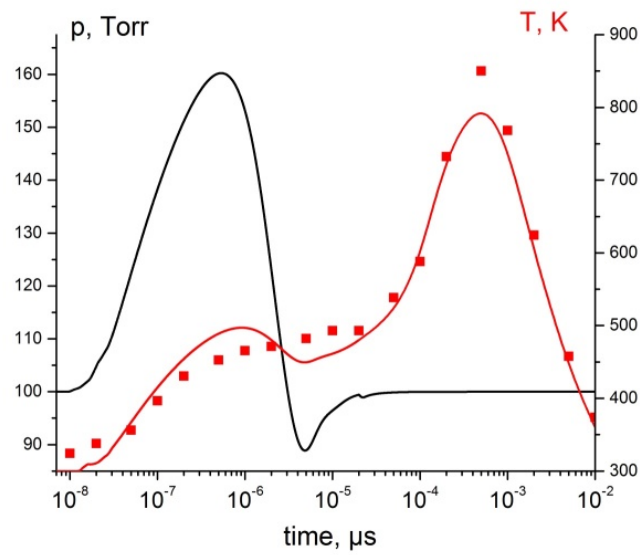


Figure IV.13. Time-resolved gas temperature (experimental and predicted) and pressure predicted on filament centerline during and after the discharge pulse in air. Symbols: experimental data, lines: model predictions.

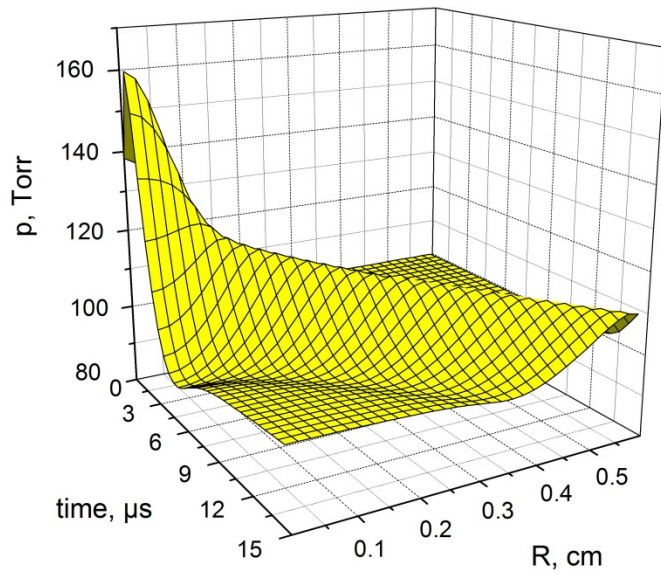


Figure IV.14. 3-D contour plot of pressure distribution after the discharge pulse in air, plotted vs. time delay after the pulse and radial distance.

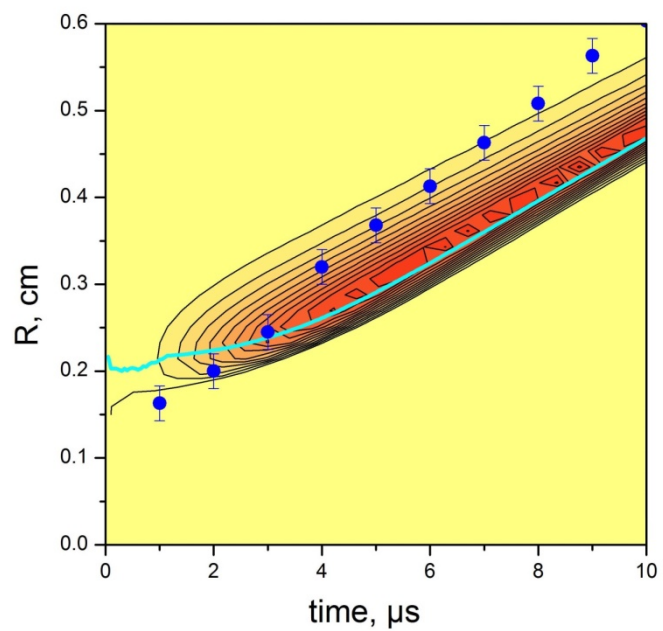


Figure IV.15. Contour plot of pressure gradient distribution after the discharge pulse in air, showing predicted compression wave trajectory (blue line), compared with experimental wave trajectory (symbols).

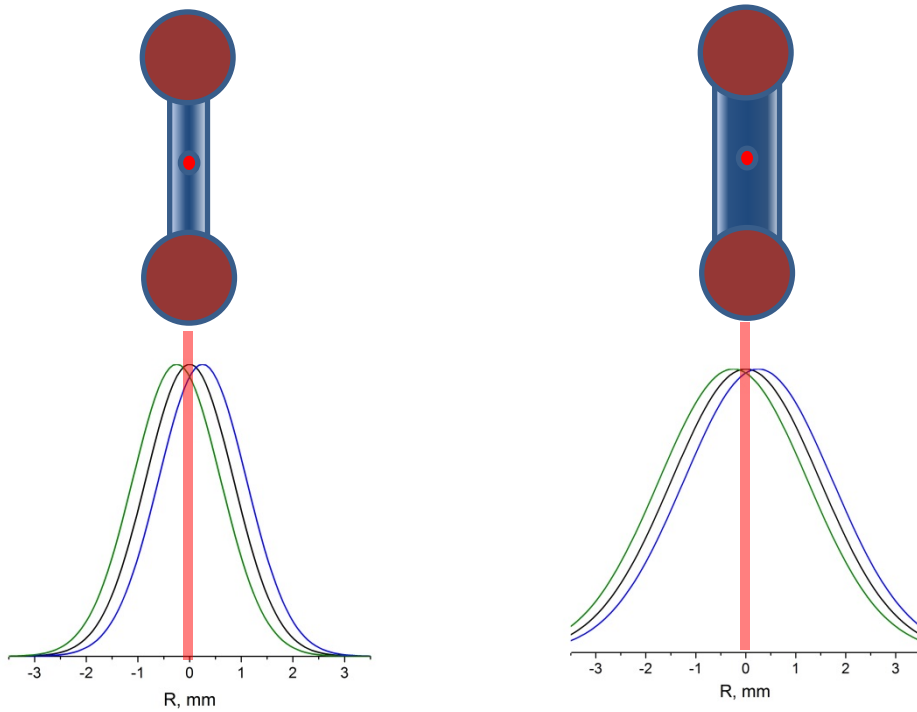


Figure IV.16. Cartoon schematic illustrating the effect of discharge filament “jitter” on CARS signal collection: left, at short times delays (before gasdynamic expansion), and right, at long time delays (after the expansion) after the discharge pulse. The red dot and the red bar indicate the location of the overlapped laser beams, estimated to be $\sim 100 \mu\text{m}$ in diameter. The curves illustrate Gaussian radial distributions of N_2 vibrational temperature, with FWHM of 2.0 mm (left) and 4.0 mm (right), displaced over $\pm 200 \mu\text{m}$ in the transverse direction.

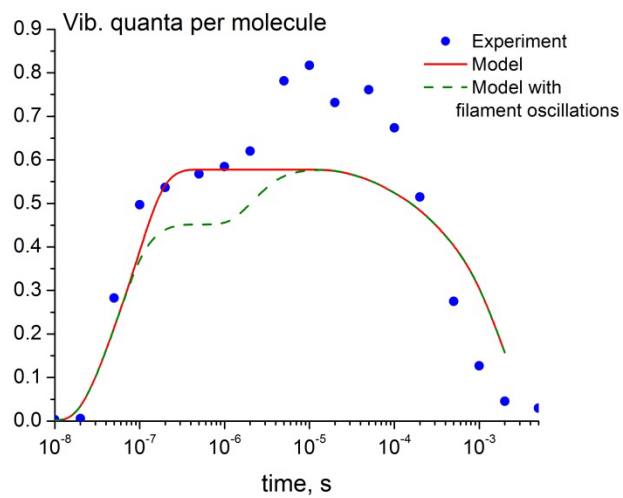


Figure IV.17. Comparison of experimental (symbols) and predicted (lines) time-resolved vibrational quanta per N_2 molecule in air, calculated with and without taking into account discharge filament “jitter”.

References

1. Gordiets, B.F., Osipov, V.A., and Shelepin, L.A., Kinetic Processes in Gases and Molecular Lasers, Gordon and Breach, London, 1988, Chaps. 3,4
2. Caciato, M., Capitelli, M., DeBenedictis, S., Dilonardo, M., and Gorse, C., "Vibrational Kinetics, Dissociation and Ionization of Diatomic Molecules under Nonequilibrium Conditions", Nonequilibrium Vibrational Kinetics, Springer-Verlag, Berlin, 1986, Chap. 2, pp. 5-46
3. Park, C., Nonequilibrium Hypersonic Aerodynamics, Wiley, New York, 1990, Chap. 3
4. M. Capitelli, I. Armenise, E. Bisceglie, D. Bruno, R. Celiberto, G. Colonna, G. D'Ammando, O. De Pascale, F. Esposito, C. Gorse, V. Laporta, A. Laricchiuta, "Thermodynamics, Transport and Kinetics of Equilibrium and Non-Equilibrium Plasmas: A State-to-State Approach", *Plasma Chem. Plasma Process.*, vol. 32, 2012, pp. 427-450
5. M. Caciato and G.D. Billing, "State-to-State Vibration-Translation and Vibration-Vibration Rate Constants in H₂-H₂ and HD-HD Collisions", *J. Phys. Chem.*, vol. 96, 1992, pp. 217-223
6. G.D. Billing and R.E. Kolesnick, "Semi-classical calculations of rate constants for vibrational transitions in hydrogen", *Chem. Phys. Lett.*, vol. 215, 1993, pp. 571-575
7. R.E. Kolesnick and Billing, G.D., "Rate Constants for Vibrational Transitions in Hydrogen and Isotopes", *Chemical Physics*, vol. 170, No. 1, 1993, pp. 201-207
8. V.A. Zenevich and G.D. Billing, "Vibrational-rotational energy transfer in H₂-H₂ collisions. I. Semiclassical decoupling approximation", *J. Chem. Phys.*, vol. 111, 1999, pp. 2401-2406
9. V.A. Zenevich, G.D. Billing, G. Jolicard, "Vibrational-rotational energy transfer in H₂-H₂ collisions. II. The relative roles of the initial rotational excitation of both diatoms", *Chem. Phys. Lett.*, vol. 312, 1999, pp. 530-535
10. Billing, G.D., and Fisher, E.R., "VV and VT Rate Coefficients in N₂ by a Quantum-Classical Model", *Chemical Physics*, Vol. 43, No.3, 1979, pp. 395-401
11. Caciato, M., Kurnosov, A., and Napartovich, A., "Vibrational Energy Transfer in N₂-N₂ Collisions: A New Semiclassical Study", *J. Chem. Phys.*, vol. 123, 2005, p. 174315
12. Billing, G.D., and Kolesnick, R.E., "Vibrational Relaxation of Oxygen. State to State Rate Constants", *Chemical Physics Letters*, Vol. 200, No. 4, 1992, pp. 382-386
13. Coletti, C., and Billing, G.D., "Vibrational energy transfer in molecular oxygen collisions", *Chem. Phys. Lett.*, vol. 356, 2002, pp. 14-22
14. Billing, G.D., "VV and VT Rates in N₂-O₂ Collisions", *Chemical Physics*, Vol. 179, No. 3, 1994, pp. 463-467
15. Lagana, A., Garcia, E., and Ciccarelli, L., "Deactivation of vibrationally excited Nitrogen Molecules by Collision with Nitrogen Atoms", *Journal of Physical Chemistry*, Vol. 91, 1987, pp. 312-314
16. Lagana, A., and Garcia, E., "Temperature Dependence of N+N₂ Rate Coefficients", *Journal of Physical Chemistry*, vol. 98, 1994, pp. 502-507
17. I. Armenise, M. Capitelli, E. Garcia, C. Gorse, A. Lagana, and S. Longo, "Deactivation dynamics of vibrationally excited nitrogen molecules by nitrogen atoms. Effects on non-equilibrium vibrational distribution and dissociation rates of nitrogen under electrical discharges", *Chem. Phys. Lett.*, vol. 200, 1992, pp. 597-604
18. G. Chaban, R. Jaffe, D. Schwenke, and W. Huo, "Dissociation cross-sections and rate coefficients for nitrogen from accurate theoretical calculations, AIAA Paper 2008-1209, 46th AIAA Aerospace Sciences Meeting and Exhibit, Reno, NV, 2008

19. R. Jaffe, D. Schwenke, G. Chaban, and W. Huo, "Vibrational and rotational excitation and relaxation of nitrogen from accurate theoretical calculations, AIAA Paper 2008-1208, 46th AIAA Aerospace Sciences Meeting and Exhibit, Reno, NV, 2008
20. R. Jaffe, D. Schwenke, and G. Chaban, "Theoretical analysis of N₂ collisional dissociation and rotation–vibration energy transfer, AIAA 2009-1569, 47th AIAA Aerospace Sciences Meeting and Exhibit, Orlando, FL, 2009
21. R. Jaffe, D. Schwenke, and G. Chaban, "Vibration–rotation excitation and dissociation in N₂- N₂ collisions from accurate theoretical calculations, AIAA Paper 2010-4517, 10th AIAA/ASME Joint Thermophysics and Heat Transfer Conference, Chicago, IL, 2010
22. F. Esposito and M. Capitelli, "Quasiclassical molecular dynamic calculations of vibrationally and rotationally state selected dissociation cross-sections: N+N₂(v,j)→3N", Chem. Phys. Lett., vol. 302, 1999, pp. 49-54
23. F. Esposito and M. Capitelli, "Quasi-classical dynamics and vibrational kinetics of N+N₂(v) system", Chem. Phys. 257, 2000, pp. 193-202
24. F. Esposito and M. Capitelli, "QCT calculations for the process N₂(v) + N → N₂(v') + N in the whole vibrational range", Chem. Physics Lett., vol. 418, 2006, pp. 581–585
25. T.E. Magin, M. Panesi, A. Bourdon, R.L. Jaffe, and D.W. Schwenke, "Coarse-grain model for internal energy excitation and dissociation of molecular nitrogen", Chem. Phys., vol. 398, 2012, pp. 90–95
26. A. Munafò, M. Panesi, R.L. Jaffe, G. Colonna, A. Bourdon, and T.E. Magin, "QCT-based vibrational collisional models applied to nonequilibrium nozzle flows", Eur. Phys. J. D, vol. 66, 2012, p. 188
27. M. Panesi, R.L. Jaffe, D.W. Schwenke, and T.E. Magin, "Rovibrational internal energy transfer and dissociation of N₂(¹Σ_g⁺) – N(⁴S_u) system in hypersonic flows", J. Chem. Phys., vol. 138, 2013, p. 044312
28. J.G. Kim and I.D. Boyd, "Monte Carlo Simulation of Nitrogen Dissociation Based on State-Resolved Cross Sections", Phys. Fluids, vol. 26, 2014, 012006
29. I.V. Adamovich and J.W. Rich, "Three-Dimensional Nonperturbative Analytic Model of Vibrational Energy Transfer in Atom-Molecule Collisions", J. Chem. Phys., vol. 109, No. 18, 1998, pp. 7711-7724
30. I.V. Adamovich, "Three-Dimensional Model of Vibrational Energy Transfer in Molecule-Molecule Collisions", AIAA J., vol. 39, No. 10, 2001, pp. 1916-1925
31. S.O. Macheret and I.V. Adamovich, "Semiclassical Modeling of State-Specific Dissociation Rates in Diatomic Gases", Journal of Chemical Physics, vol. 113, 2000, pp. 7351-7361
32. I.D. Boyd and E. Josyula "State Resolved Vibrational Relaxation Modeling for Strongly Nonequilibrium Flows", Physics of Fluids, vol. 23, 2011, p. 057101
33. C. Zhang and T.E. Schwartzentruber, "Consistent Implementation of State-to-State Collision Models for Direct Simulation Monte Carlo", AIAA Paper 2014-0866, 52nd AIAA Aerospace Sciences Meeting, 13-17 January 2014, National Harbor, Maryland
34. C. Nyeland and G.D. Billing, "Approximate Treatments of Rotational Relaxation", Chem. Phys., vol. 40, 1979, pp. 103-110
35. C. Nyeland, L.L. Poulsen, and G.D. Billing, "Rotational Relaxation and Transport Coefficients for Diatomic Gases: Computations on Nitrogen", J. Phys. Chem., 1984, vol. 88, pp. 1216-1221
36. Billing, G.D., "Rate Constants and Cross Sections for Vibrational Transitions in Atom-Diatom and Diatom-Diatom Collisions", Computer Physics Communications, Vol. 32, No. 1, 1984, pp. 45-62

37. Billing, G.D., "Rate Constants for Vibrational Transitions in Diatom-Diatom Collisions", *Computer Physics Communications*, Vol. 44, 1987, pp. 121-136
38. C. Zhang and T.E. Schwartzentruber, "Inelastic Collision Selection procedures for Direct Simulation Monte Carlo Calculations of Gas Mixtures", *Physics of Fluids*, vol. 25, 2013, p. 106105
39. C. Zhang and T.E. Schwartzentruber, "Molecular Dynamics Simulation of Rotational Relaxation in Nitrogen: Implications for Rotational Collision Number Models", *Physics of Fluids*, vol. 24, 2012, p. 106101
40. S.M. Starikovskaya, "Plasma assisted ignition and combustion", *Journal of Physics D: Applied Physics*, 39 (2006) R265
41. I.V. Adamovich, I. Choi, N. Jiang, J.-H Kim, S. Keshav, W.R. Lempert, E. Mintusov, M. Nishihara, M. Samimy, and M. Uddi, "Plasma Assisted Ignition and High-Speed Flow Control: Non-Thermal and Thermal Effects", *Plasma Sources Science and Technology*, 18 (2009) 034018
42. A. Starikovskiy and N. Aleksandrov, "Plasma-assisted ignition and combustion", *Progress in Energy and Combustion Science*, 39 (2013) 61
43. D.V. Roupasov, A.A. Nikipelov, M.M. Nudnova, A.Yu. Starikovskii, "Flow separation control by plasma actuator with nanosecond pulsed-periodic discharge", *AIAA Journal*, 47 (2009) 168
44. M. Nishihara, K. Takashima, J.W. Rich, I.V. Adamovich, "Mach 5 bow shock control by a nanosecond pulse surface dielectric barrier discharge", *Physics of Fluids*, 23 (2011) 066101
45. J. Little, K. Takashima, M. Nishihara, I. Adamovich, and M. Samimy, "Separation Control with Nanosecond Pulse Driven Dielectric Barrier Discharge Plasma Actuators", *AIAA Journal*, 50 (2012) 350
46. D.B. Graves, "The emerging role of reactive oxygen and nitrogen species in redox biology and some implications for plasma applications to medicine and biology", *Journal of Physics D: Applied Physics*, 45 (2012) 263001
47. Yu.P. Raizer, *Gas Discharge Physics*, Berlin, Springer (1991)
48. T. Unfer and J.P. Boeuf, "Modelling of a nanosecond surface discharge actuator", *Journal of Physics D: Applied Physics*, 42 (2009) 194017
49. V.R. Soloviev and V.M. Krivtsov, "Surface barrier discharge modelling for aerodynamic applications", *Journal of Physics D: Applied Physics*, 42 (2009) 125208
50. E. Marode, D. Djermoune, P. Dessante, C. Deniset, P. Segur, F. Bastien, A. Bourdon, and C. Laux, "Physics and applications of atmospheric non-thermal air plasma with reference to environment", *Plasma Physics and Controlled Fusion*, 51 (2009) 124002
51. I.V. Adamovich, M. Nishihara, I. Choi, M. Uddi, and W.R. Lempert, "Energy coupling to the plasma in repetitive pulse discharges" *Physics of Plasmas*, 16 (2009) 113505
52. N.A. Popov, "Fast gas heating in a nitrogen-oxygen discharge plasma: I. Kinetic mechanism" *Journal of Physics D: Applied Physics*, 44 (2011) 285201
53. S.M. Starikovskaia, N.B. Anikin, S.V. Pancheshnyi, D.V. Zatsepин, and A.Yu. Starikovskii, "Pulsed breakdown at high overvoltage: development, propagation and energy branching" *Plasma Sources Science and Technology*, 10 (2001) 344
54. N. B. Anikin, S. M. Starikovskaia, and A. Yu. Starikovskii, "Study of the Oxidation of Alkanes in Their Mixtures with Oxygen and Air under the Action of a Pulsed Volume Nanosecond Discharge", *Plasma Physics Reports*, 30 (2004) 1028
55. N.B. Anikin, N.A. Zavialova, S.M. Starikovskaia, and A.Yu. Starikovskii, "Nanosecond-discharge development in long tubes", *IEEE Transactions on Plasma Science*, 36 (2008) 902

56. I.A. Znamenskaya, D.F. Latfullin, A.E. Lutsky, and I.V. Mursenkova, "Energy deposition in boundary gas layer during initiation of nanosecond sliding surface discharge", *Technical Physics Letters*, **36** (2010) 795
57. K. Takashima, I.V. Adamovich, Z.M. Xiong, M.J. Kushner, S.M. Starikovskaia, U. Czarnetzki, and D. Luggenholscher, "Experimental and modeling analysis of fast ionization wave discharge propagation in a rectangular geometry", *Physics of Plasmas*, **18** (2011) 083505
58. A. D. Montello, Z. Yin, D. D. Burnette, I. V. Adamovich and W. R. Lempert, "Picosecond CARS Measurements of Nitrogen Vibrational Loading and Rotational/Translational Temperature in Nonequilibrium Discharges," *Journal of Physics D: Applied Physics*, **46** (2013) 464002
59. D. Burnette, A. Montello, S. Bowman, I.V. Adamovich, and W.R. Lempert, "Nitric Oxide Kinetics in the Afterglow of a Diffuse Plasma Filament", submitted for publication to *Plasma Sources Science and Technology*
60. T. Ahn, I.V. Adamovich, and W.R. Lempert, "Determination of nitrogen V-V transfer rates by stimulating Raman pumping", *Chemical Physics*, **298** (2004) 233
61. A.V. Phelps and L.C. Pitchford, "Anisotropic scattering of electrons by N₂ and its effect on electron transport", *Physical Review A*, **31** (1985) 2932
62. W.M. Hou, T.L. Gibson, M.A.P. Lima, and V. McKoy, "Schwinger multichannel study of the ² Π_g shape resonance in N₂", *Physical Review A*, **36** (1987) 1632
63. G.D. Billing, E.R. Fisher, "VV and VT rate coefficients in N₂ by a quantum-classical model" *Chemical Physics* **43** (1979) 395-401
64. G. V. Candler, J. D. Kelley, S.O. Macheret, M.N. Shneider, I.V. Adamovich, "Vibrational Excitation, Thermal Nonuniformities, and Unsteady Effects on Supersonic Blunt Bodies" *AIAA Journal* **40** (2002) 1803-1810
65. O.V. Braginskiy, A.N. Vasilieva, K.S. Klopovskiy, A.S. Kovalev, D.V. Lopaev, O.V. Proshina, T.V. Rakhimova, and A.T. Rakimov, "Singlet oxygen generation in O₂ flow excited by RF discharge: I. Homogeneous discharge mode: α -mode", *Journal of Physics D: Applied Physics*, **38** (2005) 3609
66. I.A. Shkurenkov, Yu.A. Mankelevich, and T.V. Rakimova, "Simulation of diffuse, constricted-stratified, and constricted modes of a dc discharge in argon: Hysteresis transition between diffuse and constricted-stratified modes", *Physical Review E*, **79** (2009) 046406
67. I.A. Kossyi, A.Yu. Kostinsky, A.A. Matveyev, and V.P. Silakov, "Kinetic scheme of the non-equilibrium discharge in nitrogen-oxygen mixtures", *Plasma Sources Science and Technology*, **1** (1992) 207
68. V. Guerra, P.A. Sa, and J. Loureiro, "Kinetic modeling of low-pressure nitrogen discharges and post-discharges", *European Physical Journal - Applied Physics*, **28** (2004) 125
69. I.A. Shkurenkov, Yu.A. Mankelevich, and T.V. Rakimova, "Diffuse and constricted modes of a dc discharge in neon: Simulation of the hysteresis transition", *Plasma Physics Reports*, **34** (2008) 780-793
70. I.P. Shkarovsky, T.W. Johnston, and M.P. Bachynskii, *The Particle Kinetics of Plasmas*, Addison-Wesley, Reading, 1966
71. D.Z. Pai, G.D. Stancu, D.A. Lacoste, C.O.Laux, "Nanosecond repetitively pulsed discharges in air at atmospheric pressure – the glow regime" *Plasma Sources Science and Technology*, **18** (2009) 045030
72. V. Lj. Marković, S. R. Gocić, S. N. Stamenković, and Z. Lj. Petrović, "Metastable and charged particle decay in neon afterglow studied by the breakdown time delay measurements", *Physics of Plasmas*, **14** (2007) 103504

73. G. Dilecce and S. De Benedictis, "Experimental studies on elementary kinetics in N₂-O₂ pulsed discharges", *Plasma Sources Science and Technology*, **8** (1999) 266
74. V. Guerra, P.A. Sa, and J. Loureiro, "Role played by the N₂(A³ Σ_u^+) metastable in stationary N₂ and N₂-O₂ discharges", *Journal of Physics D: Applied Physics*, **4** (2001) 1745
75. J.T. Herron and D.S. Green, "Chemical kinetics database and predictive schemes for nonthermal humid air plasma chemistry. Part II. Neutral Species reactions", *Plasma Chemistry and Plasma Processing*, **21** (2001) 459
76. J.T. Herron, "Modeling studies of the formation and destruction of NO in pulsed barrier discharges in nitrogen and air", *Plasma Chemistry and Plasma Processing*, **21** (2001) 581
77. C.D. Pintassilgo, J. Loureiro, V. Guerra, "Modeling of a N₂-O₂ flowing afterglow for plasma sterilization", *Journal of Physics D: Applied Physics*, **38** (2005) 417
78. A.A. Levitskii, S.O. Macheret, and A.A. Fridman, "Simulation of nonequilibrium chemical processes stimulated by vibrational-excitation of the reactants in plasma", *High Energy Chemistry*, **19** (1985) 364-370
79. I.K. Dmitrieva and V.A. Zenevich, "Nitrogen vibrational-excitation effect on N₂(v)+O→NO+N reaction-rate constant – information-theory approximation", *Khimicheskaya Fizika*, **3** (1984) 1075-1080
80. L.G. Piper, "The excitation of O(¹S) in the reaction between N₂(A³ Σ_u^+) and O(³P)", *Journal of Chemical Physics*, **77** (1982) 2373
81. S.M. Starikovskaya, "Plasma Assisted Ignition and Combustion", *Journal of Physics D: Applied Physics* **39** (2006) R265
82. I.V. Adamovich, I. Choi, N. Jiang, J.-H Kim, S. Keshav, W.R. Lempert, E. Mintusov, M. Nishihara, M. Samimy, and M. Uddi, "Plasma Assisted Ignition and High-Speed Flow Control: Non-Thermal and Thermal Effects", *Plasma Sources Science and Technology* **18** (2009) 034018
83. A. Starikovskiy and N. Aleksandrov, "Plasma-Assisted Ignition and Combustion", *Progress in Energy and Combustion Science* **39** (2013) 61
84. I.V. Adamovich and W.R. Lempert, "Challenges in Understanding and Development of Predictive Models of Plasma Assisted Combustion", accepted for publication in *Plasma Physics and Controlled Fusion*, 2014
85. M. Samimy, J.-H. Kim, J. Kastner, I. Adamovich, and Y. Utkin, "Active Control of High-speed and High Reynolds Number Jets Using Plasma Actuators", *Journal of Fluid Mechanics* **578** (2007) 305
86. D.V. Roupasov, A.A. Nikipelov, M.M. Nudnova, A.Yu. Starikovskii, "Flow separation control by plasma actuator with nanosecond pulsed-periodic discharge", *AIAA Journal* **47** (2009) 168
87. K. Takashima (Udagawa), Y. Zuzeek, W.R. Lempert, and I.V. Adamovich, "Characterization of Surface Dielectric Barrier Discharge Plasma Sustained by Repetitive Nanosecond Pulses", *Plasma Sources Science and Technology* **20** (2011) 055009
88. J. Little, K. Takashima, M. Nishihara, I. Adamovich, and M. Samimy, "Separation Control with Nanosecond Pulse Driven Dielectric Barrier Discharge Plasma Actuators", *AIAA Journal* **50** (2012) 350
89. M. Nishihara, K. Takashima, J.W. Rich, I.V. Adamovich, "Mach 5 bow shock control by a nanosecond pulse surface dielectric barrier discharge", *Physics of Fluids* **23** (2011) 066101
90. A. Fridman, *Plasma Chemistry*, Cambridge University Press, New York, 2012
91. A. Montello, M. Nishihara, J.W. Rich, I.V. Adamovich, and W.R. Lempert, "Picosecond CARS Measurements of Vibrational Distribution Functions in a High Pressure Plenum of a Nonequilibrium Hypersonic Wind Tunnel", *AIAA Journal* **50** (2012) 1367

92. Y. Zuzeek, I. Choi, M. Uddi, I.V. Adamovich, and W.R. Lempert, "Pure Rotational CARS Thermometry Studies of Low Temperature Oxidation Kinetics in Air and Ethene-Air Nanosecond Pulse Discharge Plasmas", *Journal of Physics D: Applied Physics* 43 (2010) 12400
93. Y. Zuzeek, S. Bowman, I. Choi, I.V. Adamovich, and W.R. Lempert, "Pure Rotational CARS Studies of Thermal Energy Release and Ignition in Nanosecond Repetitively Pulsed Hydrogen-Air Plasmas", *Proceedings of the Combustion Institute* 33 (2011) 3225
94. N.A. Popov, "Investigation of the mechanism for rapid heating of nitrogen and air in gas discharges", *Plasma Physics Reports* 27 (2001) 886
95. G.D. Stancu, F. Kaddouri, D.A. Lacoste, and C.O. Laux, "Atmospheric pressure plasma diagnostics by OES, CRDS and TALIF", *Journal of Physics D: Applied Physics* 43 (2010) 124002
96. N.L. Aleksandrov, S.V. Kindysheva, M.M. Nudnova, A.Yu. Starikovskiy, "Mechanism of ultra-fast heating in a non-equilibrium weakly ionized air discharge plasma in high electric fields", *Journal of Physics D: Applied Physics* 43 (2010) 255201
97. E.I. Mintoussov, S.J. Pendleton, F.G. Gerbault, N.A. Popov, and S.M. Starikovskaia, "Fast gas heating in nitrogen–oxygen discharge plasma: II. Energy exchange in the afterglow of a volume nanosecond discharge at moderate pressures", *Journal of Physics D: Applied Physics* 44 (2011) 285202
98. D.L. Rusterholtz, D.A. Lacoste, G.D. Stancu, D.Z. Pai, and C.O. Laux, "Ultrafast heating and oxygen dissociation in atmospheric pressure air by nanosecond repetitively pulsed discharges", *Journal of Physics D: Applied Physics* 46 (2013) 464010
99. D. Messina, B. Attal-Tretout, and F. Grisch, "Study of a Non-equilibrium Pulsed Nanosecond Discharge at Atmospheric Pressure Using Coherent Anti-Stokes Raman Scattering," *Proceedings of the Combustion Institute*, 31 (2007) 825-832
100. A. Montello, Z. Yin, D. Burnette, I.V. Adamovich, and W.R. Lempert, "Picosecond CARS measurements of nitrogen vibrational loading and rotational/translational temperature in nonequilibrium discharges," *Journal of Physics D: Applied Physics* 46, 464002 (2013)
101. A. Lo, A. Cessou, P. Boubert and P. Vervisch, "Space and time analysis of the nanosecond scale discharges in atmospheric pressure air: I. Gas temperature and vibrational distribution function of N₂ and O₂", *Journal of Physics D: Applied Physics* 47 (2014) 115201
102. A. Lo, A. Cessou and P. Vervisch, "Space and time analysis of the nanosecond scale discharges in atmospheric pressure air: II. Energy transfers during the post-discharge", *Journal of Physics D: Applied Physics* 47 (2014) 115202
103. N.A. Popov, "Fast gas heating in a nitrogen-oxygen discharge plasma: I. Kinetic mechanism", *Journal of Physics D: Applied Physics* 44 (2011) 285201
104. C.D. Pintassilgo, V. Guerra, O. Guaitella, and A. Rousseau, "Study of gas heating mechanisms in millisecond pulsed discharges and afterglows in air at low pressures", *Plasma Sources Science and Technology* 23 (2014) 025006
105. M. Hübner, D. Marinov, O. Guaitella, A. Rousseau, and J. Röpcke, "On time resolved gas temperature measurements in a pulsed dc plasma using quantum cascade laser absorption spectroscopy", *Measurement Science and Technology*, 23 (2012) 115602
106. A. Montello, D. Burnette, M. Nishihara, W.R. Lempert, and I.V. Adamovich, "Dynamics of Rapid Localized Heating in Nanosecond Pulse Discharges for High Speed Flow Control", *Journal of Fluid Science and Technology*, 8 (2013) 147-159
107. K. Takashima, I.V. Adamovich, Z. Xiong, M.J. Kushner, S. Starikovskaia, U. Czarnetzki, and D. Luggenhölscher, "Experimental and Modeling Analysis of Fast Ionization Wave Discharge Propagation in a Rectangular Geometry", *Physics of Plasmas*, 18 (2011) 083505

108. S.S. Bowman, I.V. Adamovich, W.R. Lempert, "Experimental and Modeling Analysis of Singlet Delta Oxygen Kinetics in a Repetitively Pulsed Nanosecond Discharge", *Plasma Sources Science and Technology*, 23 (2014) 035009
109. S.M. Roy, R. Terrence, "Broadband Coherent Anti-Stokes Raman Scattering of Nitrogen Using a Picosecond Modeless Dye Laser", *Optics Letters* 30 (2005) 3
110. A.C. Eckbreth, "BOXCARS: Crossed-Beam Phase-Matched CARS Generation in Gases", *Applied Physics Letters* 32 (1978) 421-423
111. F. Vestin, M. Afzelius, and P.-E. Bengtsson, "Development of Rotational CARS for Combustion Diagnostics using a Polarization Approach", *Proceedings of the Combustion Institute* 31 (2007) 833-840
112. R.E. Palmer, "The Carsfit Computer Code for Calculating Coherent Anti-Stokes Raman Spectra: User and Programmer Information", 1989, Sandia National Laboratories Livermore, CA
113. I. Shkurenkov, D. Burnette, W.R. Lempert, and I.V. Adamovich, "Kinetics of Excited States and Radicals in a Nanosecond Pulse Discharge and Afterglow in Nitrogen and Air", *Plasma Sources Science and Technology* 23 (2014) 065003
114. D. Burnette, A. Montello, I.V. Adamovich, and W.R. Lempert, "Nitric Oxide Kinetics in the Afterglow of a Diffuse Plasma Filament", *Plasma Sources Science and Technology* 23 (2014) 045007
115. A.V. Phelps and L.C. Pitchford, "Anisotropic scattering of electrons by N₂ and its effect on electron transport", *Physical Review A*, 31 (1985) 2932
116. W.M. Hou, T.L. Gibson, M.A.P. Lima, and V. McKoy, "Schwinger multichannel study of the ² Π_g shape resonance in N₂", *Physical Review A*, 36 (1987) 1632
117. B.F. Gordietz, A.I. Osipov, and L.A. Shelepin, *Kinetic Processes in Gases and Molecular Lasers*, Gordon and Breach, London, 1988, Ch. 3,4
118. G.V. Candler, J.D. Kelley, S.O. Macheret, M.N. Shneider, and I.V. Adamovich, "Vibrational Excitation, Thermal Nonuniformities, and Unsteady Effects on Supersonic Blunt Bodies" *AIAA Journal* 40 (2002) 1803-1810
119. R.-J. McNeal, M.E. Whitson, and G.R. Cook, "Quenching of vibrationally excited N₂ by atomic oxygen", *Chemical Physics Letters* 16 (1972) 507-510
120. F. Esposito, I. Armenise, M. Capitelli, "N-N₂ state to state vibrational-relaxation and dissociation rates based quasiclassical calculations", *Chemical Physics*, 331 (2006) 1-8
121. D.C. Allen, E.T. Chandler, E.A. Gregory, R.M. Siddles, CJS Simpson, "Vibrational deactivation of N₂ (v = 1) by n-H₂ and by p-H₂", *Chemical Physics Letters* 76 (1980) 347-353
122. M. Capitelli, C.M. Ferreira, B.F. Gordietz, A.I. Osipov, *Plasma Kinetics in Atmospheric Gases*, Springer-Verlag, Berlin, 2001, Chap.7
123. T. Ahn, I.V. Adamovich, and W.R. Lempert, "Determination of nitrogen V-V transfer rates by stimulating Raman pumping", *Chemical Physics*, 298 (2004) 233
124. I.V. Adamovich, "Three-Dimensional Model of Vibrational Energy Transfer in Molecule-Molecule Collisions", *AIAA Journal*, 39 (2001) 1916-1925
125. G.D. Billing, E.R. Fisher, "VV and VT rate coefficients in N₂ by a quantum-classical model", *Chemical Physics* 43 (1979) 395-401
126. G.D. Billing, "VV and VT Rates in N₂-O₂ Collisions", *Chemical Physics*, 179 (1994) No. 3, 463-467
127. F. Esposito, I. Armenise, G. Capitta, M. Capitelli, "O-O₂ state-to-state vibrational relaxation and dissociation rates based quasiclassical calculations", *Chemical Physics*, 351 (2008) 91-98

128. A. Lo, G. Cléon, P. Vervisch, and A. Cessou, "Spontaneous Raman scattering: a useful tool for investigating the afterglow of nanosecond scale discharges in air," *Applied Physics B: Laser and Optics*, 107 (2012) 229
129. O.V. Braginskiy, A.N. Vasilieva, K.S. Klopovskiy, A.S. Kovalev, D.V. Lopaev, O.V. Proshina, T.V. Rakhimova and A.T. Rakhimov, "Singlet Oxygen Generation in O₂ Flow Excited by RF discharge: I. Homogeneous Discharge Mode: α -mode", *Journal of Physics D: Applied Physics* 38 (2005) 3609-3625
130. A.G. Engelhardt and A.V. Phelps, "Elastic and Inelastic Collision Cross Sections in Hydrogen and Deuterium from Transport Coefficients", *Physical Review* 131 (1963) 2115
131. I.A. Shkurenkov, Yu.A. Mankelevich, and T.V. Rakhimova, "Two-dimensional simulation of an atmospheric-pressure RF DBD in a H₂ : O₂ mixture: discharge structures and plasma chemistry", *Plasma Sources Science and Technology*, 22 (2013) 015021
132. D. J. Eckstrom, "Vibrational relaxation of shock-heated N₂ by atomic oxygen using the IR tracer method", *Journal of Chemical Physics*, 59 (1973) 2787
133. M. Cacciatore, A. Kurnosov, A., and A. Napartovich, "Vibrational Energy Transfer in N₂-N₂ Collisions: A New Semiclassical Study", *Journal of Chemical Physics*, 123 (2005) 174315
134. D. Messina, B. Attal-Tretout, and F. Grisch, "Study of a Non-equilibrium Pulsed Nanosecond Discharge at Atmospheric Pressure Using Coherent Anti-Stokes Raman Scattering," *Proceedings of the Combustion Institute* 31 (2007) 825-832
135. G.D. Stancu, F. Kaddouri, D.A. Lacoste, and C.O. Laux, "Atmospheric Pressure Plasma Diagnostics by OES, CRDS and TALIF", *Journal of Physics D: Applied Physics* 43 (2010) 124002
136. D.L. Rusterholtz, D.A. Lacoste, G.D. Stancu, D.Z. Pai, and C.O. Laux, "Ultrafast heating and oxygen dissociation in atmospheric pressure air by nanosecond repetitively pulsed discharges", *Journal of Physics D: Applied Physics* 46 (2013) 464010
137. E.I. Mintoussov, S.J. Pendleton, F.G. Gerbault, N.A. Popov, and S.M. Starikovskaia, "Fast gas heating in nitrogen–oxygen discharge plasma: II. Energy exchange in the afterglow of a volume nanosecond discharge at moderate pressures", *Journal of Physics D: Applied Physics* 44 (2011) 285202
138. S. Lanier, I. Shkurenkov, I.V. Adamovich, and W.R. Lempert, "Two-Stage Energy Thermalization Mechanism in Nanosecond Pulse Discharges in Air and Hydrogen-Air Mixtures", *Plasma Sources Science and Technology* 24 (2015) 025005
139. D. Burnette, A. Montello, I.V. Adamovich, and W.R. Lempert, "Nitric Oxide Kinetics in the Afterglow of a Diffuse Plasma Filament", *Plasma Sources Science and Technology* 23 (2014) 045007
140. A. Lo, G. Cléon, P. Vervisch, and A. Cessou, "Spontaneous Raman scattering: a useful tool for investigating the afterglow of nanosecond scale discharges in air," *Applied Physics B: Laser and Optics* 107 (2012) 229
141. A. Lo, A. Cessou, P. Boubert and P. Vervisch, "Space and time analysis of the nanosecond scale discharges in atmospheric pressure air: I. Gas temperature and vibrational distribution function of N₂ and O₂", *Journal of Physics D: Applied Physics* 47 (2014) 115201
142. A. Lo, A. Cessou and P. Vervisch, "Space and time analysis of the nanosecond scale discharges in atmospheric pressure air: II. Energy transfers during the post-discharge", *Journal of Physics D: Applied Physics* 47 (2014) 115202
143. A. Montello, Z. Yin, D. Burnette, I.V. Adamovich, and W.R Lempert, "Picosecond CARS measurements of nitrogen vibrational loading and rotational/translational temperature in nonequilibrium discharges," *Journal of Physics D: Applied Physics* 46 (2013) 464002

144. D.A. Xu, D.A. Lacoste, D.L. Rusterholtz, P.-Q. Elias, G.D. Stancu, and C.O. Laux, "Experimental study of the hydrodynamic expansion following a nanosecond repetitively pulsed discharge in air", *Applied Physics Letters* 99 (2011) 121502
145. A. Montello, D. Burnette, M. Nishihara, W.R. Lempert, and I.V. Adamovich, "Dynamics of Rapid Localized Heating in Nanosecond Pulse Discharges for High Speed Flow Control", *Journal of Fluid Science and Technology* 8 (2013) 147-159
146. D.V. Roupasov, A.A. Nikipelov, M.M. Nudnova, and A.Yu. Starikovskii, "Flow separation control by plasma actuator with nanosecond pulsed-periodic discharge", *AIAA Journal* 47 (2009) 168
147. J. Little, K. Takashima, M. Nishihara, I. Adamovich, and M. Samimy, "Separation Control with Nanosecond Pulse Driven Dielectric Barrier Discharge Plasma Actuators", *AIAA Journal* 50 (2012) 350-365
148. Y. Ju and W. Sun, "Plasma assisted combustion: Dynamics and chemistry", *Progress in Energy and Combustion Science* 48 (2015) 21-83
149. D.B. Graves, "The emerging role of reactive oxygen and nitrogen species in redox biology and some implications for plasma applications to medicine and biology", *Journal of Physics D: Applied Physics* 45 (2012) 263001
150. N.A. Popov, "Investigation of the mechanism for rapid heating of nitrogen and air in gas discharges", *Plasma Physics Reports* 27 (2001) 886
151. N.A. Popov, "Fast gas heating in a nitrogen-oxygen discharge plasma: I. Kinetic mechanism", *Journal of Physics D: Applied Physics* 44 (2011) 285201
152. E. Marode, D. Djermoune, P. Dessante, C. Deniset, P. Segur, F. Bastien, A. Bourdon, and C. Laux, "Physics and applications of atmospheric non-thermal air plasma with reference to environment", *Plasma Physics and Controlled Fusion* 51 (2009) 124002
153. F. Tholin and A. Bourdon, "Influence of temperature on the glow regime of a discharge in air at atmospheric pressure between two point electrodes", *Journal of Physics D: Applied Physics* 44 (2011) 385203
154. F. Tholin and A. Bourdon, "Simulation of the hydrodynamic expansion following a nanosecond pulsed spark discharge in air at atmospheric pressure", *Journal of Physics D: Applied Physics* 46 (2013) 365205
155. S. Nagaraja, V. Yang, and I. Adamovich, "Multi-Scale Modeling of Pulsed Nanosecond Dielectric Barrier Plasma Discharges in Plane-to-Plane Geometry", *Journal of Physics D: Applied Physics* 46 (2013) 155205
156. H. Takana and H. Nishiyama, "Numerical simulation of nanosecond pulsed DBD in lean methane-air mixture for typical conditions in internal engines", *Plasma Sources Science and Technology* 23 (2014) 034001
157. I. Shkurenkov, D. Burnette, W.R. Lempert, and I.V. Adamovich, "Kinetics of Excited States and Radicals in a Nanosecond Pulse Discharge and Afterglow in Nitrogen and Air", *Plasma Sources Science and Technology* 23 (2014) 065003
158. V. Guerra, P.A. Sá, and J. Loureiro, "Kinetic modeling of low-pressure nitrogen discharges and post-discharges", *European Physical Journal Applied Physics* 28 (2004) 125-152
159. N.A. Popov, "Vibrational Kinetics of Electronically-excited $N_2(A^3\Sigma_u^+, v)$ Molecules in Nitrogen Discharge Plasma", *Journal of Physics D: Applied Physics* 46 (2013) 355204
160. J. T. Herron, "Evaluated Chemical Kinetics Data for Reactions of $N(^2D)$, $N(^2P)$, and $N_2(A^3\Sigma_u^+)$ in the Gas Phase", *Journal of Physical and Chemical Reference Data* 28 (1999) 1453-1483

161. B.R.L. Galvao, J.P. Braga, J.C. Belchior, and A.J.C. Varandas, “Electronic Quenching in N(²D) + N₂ Collisions: A State-Specific Analysis via Surface Hopping Dynamics”, Journal of Chemical Theory and Computation 10 (2014) 1872-1877
162. A.A. Devyatov, S.A. Dolenko, A.T. Rakhimov, T.V. Rakhimova, N.N. Roi, and N.V. Suetin, “Investigation of kinetic processes in molecular nitrogen by the CARS method”, Soviet Physics JETP 63 (1986) 246-250
163. K. A. Vereshchagin, V. V. Smirnov, and V. A. Shakhmatov, “CARS study of the vibrational kinetics of nitrogen molecules in the burning and afterglow stages of a pulsed discharge”, Technical Physics 42 (1997) 487-494

AFOSR Deliverables Submission Survey

Response ID:6626 Data

1.

1. Report Type

Final Report

Primary Contact E-mail

Contact email if there is a problem with the report.

adamovich.1@osu.edu

Primary Contact Phone Number

Contact phone number if there is a problem with the report

614-292-8453

Organization / Institution name

Ohio State University

Grant/Contract Title

The full title of the funded effort.

Nonequilibrium Molecular Energy Coupling and Conversion Mechanisms for Efficient Control of High-Speed Flow Field

Grant/Contract Number

AFOSR assigned control number. It must begin with "FA9550" or "F49620" or "FA2386".

FA9550-12-1-0439

Principal Investigator Name

The full name of the principal investigator on the grant or contract.

Igor V. Adamovich

Program Manager

The AFOSR Program Manager currently assigned to the award

Michael R. Berman

Reporting Period Start Date

09/01/2012

Reporting Period End Date

05/14/2016

Abstract

The report presents results of development of an accurate, physics-based model of vibrational and rotational energy transfer in three-dimensional collisions of rotating diatomic molecules, applicable over a wide range of collision energies and vibrational / rotational quantum numbers, and results of detailed kinetic modeling studies of state-to-state molecular energy transfer processes, including excitation of vibrational and electronic states by electron impact, collisional quenching of excited electronic states, vibration-vibration (V-V) energy transfer, vibration-rotation-translation (V-R-T) relaxation, internal mode energy thermalization, molecular dissociation (both by electron impact and during quenching of excited electronic state), and plasma chemical reactions. The kinetic modeling prediction are compared with recent time-resolved, spatially resolved measurements of vibrational level populations, gas temperature, and atomic species and radical number densities in the afterglow of a ns pulse discharge generating strong internal energy mode disequilibrium in air and fuel-air mixtures. The present results provide new quantitative insight into kinetics of molecular energy transfer and plasma chemical reactions in air and fuel-air mixtures, at the conditions of strong internal energy mode disequilibrium. Closed-form, physics-based,

DISTRIBUTION A: Distribution approved for public release.

analytic expressions for state-to-state rotational and vibrational energy transfer transition probabilities lend themselves to straightforward incorporation into state-of-the-art DSMC nonequilibrium flow codes. Understanding kinetics of energy thermalization and chemical reactions in ns pulse discharges considerably improves predictive capability of kinetic models, which has major implications for plasma assisted combustion and high-speed plasma flow control, where these discharges are used increasingly widely.

Distribution Statement

This is block 12 on the SF298 form.

Distribution A - Approved for Public Release

Explanation for Distribution Statement

If this is not approved for public release, please provide a short explanation. E.g., contains proprietary information.

SF298 Form

Please attach your [SF298](#) form. A blank SF298 can be found [here](#). Please do not password protect or secure the PDF. The maximum file size for an SF298 is 50MB.

[SF 298 AFOSR BRI final report2016.pdf](#)

Upload the Report Document. File must be a PDF. Please do not password protect or secure the PDF . The maximum file size for the Report Document is 50MB.

[AFOSR BRI final report 2016.pdf](#)

Upload a Report Document, if any. The maximum file size for the Report Document is 50MB.

Archival Publications (published) during reporting period:

1. I.V. Adamovich, "Three-Dimensional Analytic Probabilities of Coupled Vibrational-Rotational-Translational Energy Transfer for DSMC Modeling of Nonequilibrium Flows", Physics of Fluids 26 (2014) 046102
2. I. Shkurenkov, D. Burnette, W.R. Lempert, and I.V. Adamovich, " Kinetics of Excited States and Radicals in a Nanosecond Pulse Discharge and Afterglow in Nitrogen and Air", Plasma Sources Science and Technology 23 (2014) 065003
3. S. Lanier, I. Shkurenkov, I.V. Adamovich, and W.R. Lempert, "Two-Stage Energy Thermalization Mechanism in Nanosecond Pulse Discharges in Air and Hydrogen-Air Mixtures", Plasma Sources Science and Technology 24 (2015) 025005
4. I. Shkurenkov and I.V. Adamovich, "Energy Balance in Nanosecond Pulse Discharges in Nitrogen and Air", Plasma Sources Science and Technology 25 (2016) 015021

2. New discoveries, inventions, or patent disclosures:

Do you have any discoveries, inventions, or patent disclosures to report for this period?

No

Please describe and include any notable dates

Do you plan to pursue a claim for personal or organizational intellectual property?

Changes in research objectives (if any):

Change in AFOSR Program Manager, if any:

Extensions granted or milestones slipped, if any:

No-cost extension from 11/14/2015 until 5/14/2016

AFOSR LRIR Number

LRIR Title

Reporting Period

Laboratory Task Manager

DISTRIBUTION A: Distribution approved for public release.

Program Officer

Research Objectives

Technical Summary

Funding Summary by Cost Category (by FY, \$K)

	Starting FY	FY+1	FY+2
Salary			
Equipment/Facilities			
Supplies			
Total			

Report Document

Report Document - Text Analysis

Report Document - Text Analysis

Appendix Documents

2. Thank You

E-mail user

Aug 01, 2016 14:03:20 Success: Email Sent to: adamovich.1@osu.edu